Quantum Effects in 2D Dirac Materials with Strong Spin-Orbit Coupling: From Spin-Orbit Torques to Quantum Interference Phenomena

Frederico João Ferreira de Sousa

DOCTOR OF PHILOSOPHY

UNIVERSITY OF YORK

PHYSICS

May 26, 2021

Abstract

In the last decade, spintronics has emerged as a major field in condensed matter physics. It aims to use the spin degree of freedom of charge carriers to store, process and transmit information. Offering low power consumption and high efficiency devices, it represents a path towards the next step up for modern electronics. Spin-orbit torque (SOT) is a spintronics-based phenomenom. It makes use of the coupling between the electronic spin and momentum present in some systems to electrically control the magnetisation of magnetic materials.

Two dimensional (2D) materials offer an ideal venue for spintronics applications due to their low dimensionality, versatility and tunability. Vertical stacking of different layers allows for a remarkable control of the resulting properties. This includes the engineering of the much sought after spin-orbit coupling (SOC) via proximity interaction. The effects of strong SOC in these heterostructures, however, remains fairly unexplored.

The aim of this thesis is twofold: to understand how SOC changes the quantum interference effects, and to develop a microscopic theory for SOT in disordered 2D Dirac heterostructures.

In Dirac materials the interplay between spin, pseudospin and isospin vastly enriches the picture of quantum interference corrections. We find that an unconventional SOC-driven weak localisation phase arises due to spin-pseudospin coupling. Intervalley scattering recovers the standard weak anti-localisation making detecting it very challenging.

Interesting results arise in ferromagnetic Dirac heterostructures. We find new skew-scattering-induced spin responses: a collinear Edelstein effect and out-of-plane spin response. Both constitute robust sources of damping-like SOT and are highly sensitive to disorder strength. We show how all the responses can be interpreted in terms Fermi surface spin textures. In gapped systems the SOT becomes highly anisotropic and a non-perturbative approach is necessary. These findings provide new insight into the nature of SOT in ultra-thin structures.

Contents

5

List of Tables

List of Figures

Acknowledgements

Sir Isaac Newton was undoubtedly a physics behemoth but not even him had shoulders as stable as I had to stand on. As obvious as it might sound, it still needs to be said that this work and these last couple of years would not have been possible without the help and presence of a lot of important people in my life, to whom I will forever be grateful.

Firstly, Aires, whose ability to easily solve what seems insurmountable. I owe you these last 4 great years in York filled with uncountable opportunities that have enriched my life academically but also personally. I will always treasure the discussions we had at the white boards and at the pubs. None of this would have been possible without you. Thank you.

To all my friends that have shared this journey with me, thank you. You have time and time again given more reasons to keep going and make you proud. Patrick, Bilou, Brejo, Alho, Chico, Serrano, I look forward to seeing you again. Thank you Diogo for all the support and keeping me motivated with climbing, work and life. Thank you João for all the great chats and advice. Thank you for the nights watching shows, playing games and chatting Luís. And thank you Afonso for all the terribly great chess games.

It would be remiss of me not to mention my great office companions. My mentor Manuel who not only taught me the ropes in the research group but also the way around the many pubs of York. Neville, who let me geek out to my heart's content. My very good friend Alessandro for allowing me to share what I know, hyping me up to work out, practicing pistol squats and just generally vastly improving any sort of activity with your enthusiasm. And lastly but not least, Francisco the alternative guy, that always reminds me of the important things.

A massive thank you to my family, that have always been a safe haven for me. My parents truly are giants that have propped me up since I was a kid reading Carl Sagan. It is no secret that without your unconditional support I would not be where I am today and I would not be who I am. Cristina, Catarina and João Maria have always kept me grounded and I always strived to make you proud.

And finally, Amyzinha, for taking care of my heart when my brain was busy with the PhD, for being there for me every single day and keeping me sane (a remarkably daunting task!). I cannot thank you enough.

Declaration

I declare that this thesis is a presentation of original work and I am the sole author. This work has not previously been presented for an award at this, or any other, university. All sources are acknowledged as References. Some parts of this work are adaptations of articles published in peer-reviewed scientific journals or are in the process of being submitted for publication. In particular, work from Chapter 4 is currently in preparation for later publication and Chapter 5 expands on work published in:

- "Skew-scattering-induced giant antidamping spin-orbit torques: Collinear and out-of-plane Edelstein effects at two-dimensional material/ferromagnet interfaces", Frederico Sousa, Gen Tatara and Aires Ferreira, Physical Review Research **2**, 043401 (2020).

I declare that I was a main participant in producing the research mentioned above and described throughout this thesis. From outlining projects, calculations and result interpretation, to drafting the papers mentioned above.

Signed,

Frederico Sousa

Chapter 1

Introduction

Two Dimensional Materials: Ever more relevant

Science is a paradoxical field that lives by the very thing it tries to eradicate: the unknown. For this goal, it does not shy away from the inconceivably large nor from the unthinkably small. Ideas and concepts need to go through the ultimate filter that is nature. Once in a while, unusual and non-intuitive concepts manage to pass this sifting process and that is when the scientific community goes into a frenzy and breakthroughs are made.

It has been more than 15 years since the first isolation of a truly two dimensional (2D) material [1]. The successful isolation of atomically thin carbon layers, known as graphene, marked the beginning of a scientific "gold rush". The study of low dimensional materials became much more than an abstract endeavour as exciting new application possibilities sprouted across a wide range of areas. Energy storage, water filtration systems, solar cells and biological tissue fabrication [2–4] are but a few examples of graphene's versatility. Its low dimensionality plays a crucial role in the unique electronic, thermal and optical properties that allow for such applications [5]. Concurrently, it provided a perfect playground to tackle fundamental questions regarding the behaviour of fermions in the 2D limit with respect with Klein tunneling [6, 7], Fermi liquid theory [8] and quantum Hall effect [9, 10], to name a few.

Perhaps most importantly, graphene was proof that 2D materials were not only a real possibility, but also hosts to interesting physical properties and phenomena. It was not long until new atomically thin compounds were

isolated [11]. Monolayer hexagonal boron nitride (hBN) is an isomorph of graphene, but displays a large direct band gap [12], and 2D crystals obtained from transition metal dichalcogenide (TMD) compounds can be metallic (e.g. NbS_2 [13]) or semiconductors (e.g. MoS_2 [14] and WS_2 [15]). It is this vast variety, mixed with the high degree of tunability that is inherent to 2D materials, that makes them prime candidates for cutting-edge technological applications [16]. These monolayers can be obtained from their respective bulk compounds via mechanical or chemical exfoliation techniques [11, 17, 18]. Alternatively, large scale high quality samples can be fabricated employing bottom-up approaches such as chemical vapour deposition [19–21]. The advancement of our understanding, together with the improvement of fabrication techniques have led to new methods of enhancing their qualities (and lessening their drawbacks), as well as to the discovery of new monolayer crystals. With proposals of 2D topological insulators (TI) [22] and, more recently, their experimental realisation [23, 24] and the first isolations of magnetic 2D materials [25, 26], new paths for research are still being paved. The field of 2D physics is still flourishing as atomically thin materials continue to provide a fertile ground for physics discoveries.

Exploring internal degrees of freedom: Spintronics, Valleytronics

The field of electronics has completely reshaped the technological paradigm of the 20th century. The invention of the transistor in 1948 triggered a self-sustained boom of technological development that quickly permeated through much of our daily lives. The order of the day is speed and efficiency, and the need for better electronic devices is nothing but increasing. The exponential growth of the density of transistors in integrated circuits observed in the last 50 years – known as Moore's Law [27] – is slowing down. Technology giants like Samsung Electronics were pushing for mass scale production in 2020 of "5mm node" transistors but the development is becoming slower and more expensive. At this scale, quantum tunneling and quantum confinement effects become more pronounced (the atomic radius of silicon is ~ 0.1 nm), leading to higher power consumption due to leakage currents [28]. In light of these difficulties, there has been big a focus on finding alternative technologies able to keep up with the demands set by precedent developments. A complete overhaul of the technology industry is a daunting and

incredibly expensive task, especially after decades of investment and development, so it comes as no surprise that efforts are concentrated into complementary technologies. Among those, spintronics shows a lot of promise, making use of extra information encoded in the electrons: the spin.

The goal of spintronics is to use, in addition to the charge, the spin degree of freedom (DOF) of charge carriers to store, transfer and process data in solid state devices. Some of its main selling points include dissipationless pure spin currents and high stability spin-based non volatile memories, which are attractive from the point of view of energy consumption of devices and data storage applications. The field of spintronics can be said to have started in the 1970s with the detection of spin polarised electron tunneling [29], and later the first injection of spin-polarised currents into non-magnetic metals in 1985 [30], but it truly came to life with the discovery of the giant magnetoresistance (GMR) effect by Albert Fert and Peter Grünberg in 1988 [31, 32], which earned them the Physics Nobel Prize in 2007, cementing the importance of spintronics as an emergent research field. The GMR is a phenomenom wherein the resistance of a magnetic multilayer system greatly depends on the relative magnetic orientation of the layers and paved the way for magnetoresistive random access memories (MRAMs).

Electrical control of the electron's spin

To develop robust spintronics devices it is necessary to have control over the eletronic spin DOF and ways of generating spin currents. For earlier devices, this was accomplished via magnetic materials: the exchange interaction between the local magnetic moments and the itinerant electrons leads to a transfer of angular momentum so that driving a charge current through a ferromagnet (FM) generates a polarised charge current. Recently there has been a great interest in all-electrical control and generation of spin currents in non-magnetic media, bypassing the magnetic parts which make it harder to integrate into existing electronic systems. The quintessential example of such charge-to-spin current coupling is the spin Hall effect (SHE)[33]. First predicted in 1971 by Mikhail Dyakonov and Vladimir Perel [34], it consists in a generation of a pure spin current perpendicular to the applied charge current, as depicted in Fig. 1.1a. This spin current usually manifests itself as spin accumulation of opposite signs at the edges of the conductor (Fig. 1.1b). The resulting polarisation is always perpendicular to both the initial charge current and ensuing spin current [35]. In thin films the spin current is po-
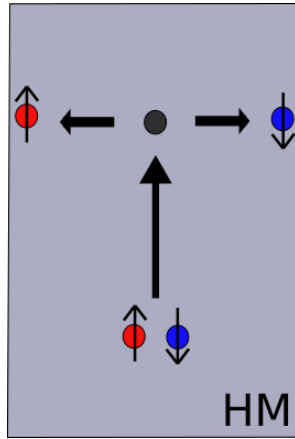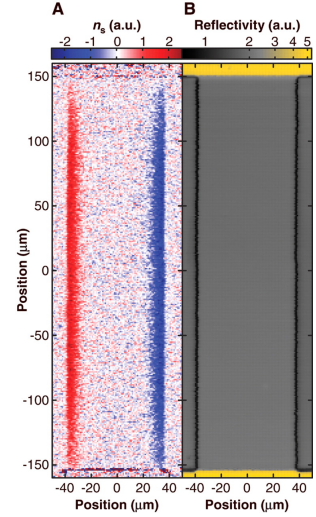
Figure 1.1: (a) The spin-Hall effect is the spin analogy to the conventional Hall effect. In spin-orbit-active materials, electrons experience a spin-dependent scattering which leads to a pure spin current transverse to the applied current. (b) Optical measurement of the edge spin accumulation generated by SHE in the semiconductor GaAs [37].

larised in the out-of-plane direction since there is much more phase space for scattering in the plane defined by the film. The separation of spin projections is enabled by spin-orbit coupling (SOC) present in the material (either intrinsically or in impurities), similarly to a Mott scattering event [36]. It was first experimentally detected in semiconductors by measuring the spin accumulation at the edges [37, 38] using Kerr rotation. This is a technique that makes use of the magneto-optic Kerr effect, which is the change of the polarisation of a reflected light beam due to the magnetisation/spin-polarisation of the medium. The reciprocal effect to SHE, wherein a spin current generates a transverse charge current, known as the inverse spin Hall effect (ISHE), was first seen in metals, and later semiconductors [39–41] and can be used as a spin current detection tool that does not require magnetic components.

Spin orbit interaction enables more charge-to-spin conversion mechanisms other than the SHE. The inverse spin galvanic effect (ISGE), or Rashba-Edelstein effect (REE), is the generation of an in-plane spin polarisation in systems with broken inversion symmetry, upon application of a charge current. The theory behind this phenomenom was developed with the model for a 2D electron gas (2DEG) in the presence of a SOC of the Bychkov-Rashba[1] type [42] in mind [43–46]:

---

[1]For brevity we refer to it as simply Rashba SOC from now on.

$$\mathcal{H}^{\text{2DEG}} = \frac{\mathbf{p}^2}{2m_e} + \lambda_R \left(\mathrm{p}_x s_y - \mathrm{p}_y s_x \right), \qquad (1.1)$$

where $\mathbf{p} = \left(\mathrm{p}_x, \mathrm{p}_y \right)$ is the electron momentum, m_e is the electron effective mass, λ_R is the Rashba parameter and $\boldsymbol{s} = (s_x, s_y, s_z)$ is the vector of Pauli matrices acting on the spin space, defined as:

$$s_x = \begin{pmatrix} 0 & 1 \\ 1 & 0 \end{pmatrix}, \quad s_y = \begin{pmatrix} 0 & -i \\ i & 0 \end{pmatrix}, \quad s_z = \begin{pmatrix} 1 & 0 \\ 0 & -1 \end{pmatrix}. \qquad (1.2)$$

The Rashba SOC is allowed by the breaking of the $z \to -z$ inversion symmetry and it should be clear that without any inversion asymmetry there could be no connection between a charge current and a non-equilibrium spin polarisation since these two quantities transform differently under such transformation. The ISGE has a simple semiclassical explanation based on Fermi surface effects. The Rashba SOC locks the electron spin in plane, winding around the Fermi rings (with opposite chirality in each ring) such that a population imbalance brought about by an electric field invariably leads to a non-cancellation of the spin in the direction perpendicular to the electric field. It was actually the reciprocal of the ISGE, the spin galvanic effect (SGE), that was measured first in GaAs quantum wells [47]. Subsequently, experiments in InGaAs and AlGaAs/GaAs heterostructures [38, 48] showed evidence of the ISGE in conjuction with SHE. In general, separating the two contributions is no easy task and requires either multiple experiments with different devices or a careful symmetry analysis of the results with respect to an external magnetic field. Sánchez *et al.* have measured a charge current generated after the injection of a spin current in Bi/Ag system that is much larger than the one measured in the Ag/Ag or Bi/Bi structures, indicating that the spin to charge conversion mechanism is dominated by the SGE [49] (Figs. 1.2a-1.2b).

Other types of SOC can arise upon breaking of other inversion symmetries. The Dresselhaus SOC, for instance, is present in systems that lack an inversion center. Originally studied in Zinc Blende structures [50], it has the following form in 2D:

$$\mathcal{H}_D = \lambda_D \left(s_x \mathrm{p}_x - s_y \mathrm{p}_y \right), \qquad (1.3)$$

to linear order in the momentum, with coupling strength λ_D. Depending on the particular asymetry there can be other types of spin-orbit interactions,

17

such as the spin-valley coupling (see Chapter 3).

In graphene-based heterostructures the ISGE was recently measured in a spin-valve geometry [30, 51], illustrated in Fig. 1.2c. In this set up one first generates a spin density (in this case via either the SHE or ISGE) at the injection point. The spins then diffuse through a channel where a magnetic field is applied, inducing Larmor precession. The spin signal is then detected at the end of the spin channel via a ferromagnet, as shown in Fig. 1.2c. Sweeping the magnetic field modulates the signal yielding Hanle precession curves (Fig. 1.2d). The SHE and ISGE have different symmetries regarding the orientation of the magnetic field so they can be discriminated using oblique fields [52–55].

The spin orbit interaction plays a key role in the electrical control of spins and was expertly exploited in the 1990 proposal of a spin field-effect transistor by Datta and Das [58]. They envisioned a device composed of a spin source and drain (ferromagnets) and a channel through which the spins would propagate. Similarly to the aforementioned spin valve set up, the relative orientation between the drain magnetisation and the spins determines the strength of the signal, however, in this case there is no applied magnetic field. The spin precession is activated by the SOC that is assumed to exist in the channel, and acts as a pseudo-magnetic field. The final piece is the SOC tuning via a gate voltage, allowing for the control of the spins precession rate and thus the signal at the drain. The Datta-Das transistor is an important concept in spintronics and functioning versions of it have already been manufactured [59]. With this device in mind we shall see in the next Sections why 2D materials are so promising for spintronics applications.

Spin Orbit Torque

Spin-charge conversion mechanisms such as the SHE, ISGE and their inverse are now playing major roles in the development of MRAM. Non-volatile memory cells have seen remarkable advances. Originally based on the GMR effect, developments on magnetic tunnel junctions (MTJ) [60–62] and spin transfer torque (STT) [63–65] have opened paths towards new paradigms of MRAM. The STT is the transfer of angular momentum from itinerant electrons to the local magnetic moments of a magnet. Typically, the electrons are polarised by interacting with local magnetic moments in a localised region of the system (e.g. a FM layer of a multilayer system or a domain of a FM) and then flow into another region with a different magnetisation orientation

(a)

(b)

(c)

(d)
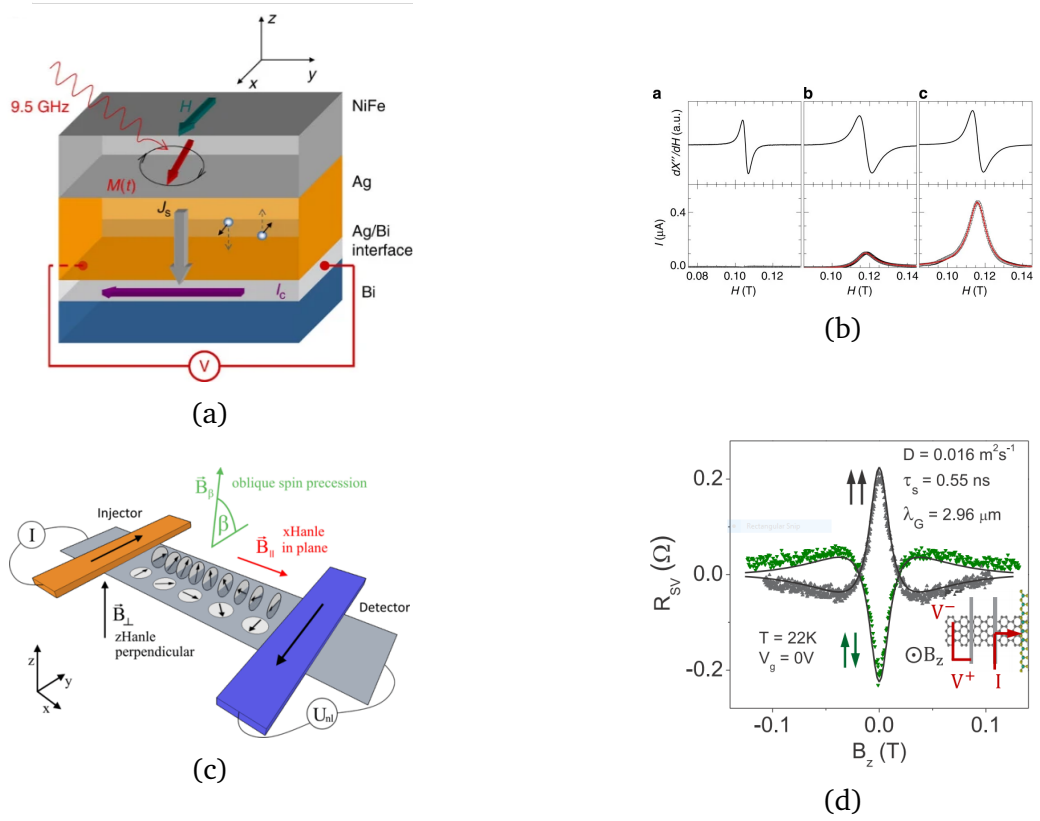
Figure 1.2: In (a) and (b) (taken from Ref. [49]) a spin current is excited in a ferromagnet via magnetic resonance. This spin current is then converted into a charge current at the Ag/Bi interface, seen in the bottom right panel of (b). If interface asymmetry is removed, by making it Ag/Ag or Bi/Bi (bottom left and center panels respectively), there is a significant reduction of the detected signal, indicating that the conversion must be done mainly via the SGE. The spin valve set up shown in (c) from Ref. [51] is be used to detect spin signals (often to extract spin diffusion lengths [56, 57]). At the injector, a spin polarisation is generated (for example via the ISGE) which diffuses through the channel where a magnetic field is applied. By changing the intensity and orientation of the magnetic field, one can modulate the signal measured at the detector, generally a ferromagnet. Such a modulation can be seen in (d), from Ref. [54], as a magnetoresistivity curve that captures the dependence of the resistivity on the relative orientation between the electrons spins and the mangnetisation of the ferromagnet.

exerting a torque and reorienting the magnetisation, as depicted in panel (a) of Fig. 1.3. Spin pumping is the reciprocal effect of STT [66]– i.e. the emission of spin currents by magnetisation dynamics – and is a valuable tool in probing spin-dependent phenomena [67, 68]. There are some issues with the STT approach for large density memories where large spin currents must be driven through MTJ without damaging the barriers and maintaining reliable switching [69]. Furthermore, ultrafast switching requires large currents

that are damaging to the magnetic junction. An alternative method known as spin-orbit torque (SOT) is a variation of STT where the spin polarisation is generated via charge-to-spin conversion phenomena such as the SHE or ISGE [70–72]. Placing a heavy metal (HM) in contact with the FM and driving a charge current through it leads to the polarisation of electrons at the interface (panels (b) and (c) of Fig. 1.3). This way, the switching of the FM can be achieved without relying on extra magnetic parts. Reversing the current changes the sign of spin polarisation, so SOT allows for a reversible control of the magnetisation. These electrically driven torques have already been observed in a wide variety of structures such as HM/FM bilayers [69, 73, 74], TI [75, 76] and, more recently, 2D materials [77–81].

The standard measurement of SOT is based on ferromagnetic resonance (FMR) experiments [82]. In FMR, an alternating current is applied in plane, generating a torque field which in turn excites magnetisation dynamics in the FM. Due to the anisotropy magnetoresistance of the FM, the measured resistance will oscillate in time with a frequency set by an external magnetic field that is non collinear with the applied current. This leads to frequency mixing and a dc voltage V_{mix} that is measured. When the resonance frequency of the FM matches the ac frequency, V_{mix} displays a peak whose shape characterises the existing torques in the sample.

Another technique for measuring SOT is known as the second harmonic Hall measurement [83, 84]. This makes use of the fact that the tilting of magnetisation in a FM induces a change in the Hall resistance ρ_{H} [85]. Hence, driving an ac current $I(\omega)$ through a FM will modulate the Hall resistance due the oscillation of the current-generated SOT. The Hall voltage includes then second harmonic terms $V_{\mathrm{H}} = \rho_{\mathrm{H}} I(\omega)$, with respect to the relative angles between the applied magnetic field and the current. From the harmonic expansion one can extract the effective fields associated with the SOT. This technique has been used to detect SOTs in various systems such as oxide trilayers [83, 84, 86], normal metal/FM bilayers [87, 88] and TMD/FM bilayers [77].

There are already significant advancements when it comes to the theory behind the microscopic origin of SOT in 2DEG [89, 90] and topological insulators [91]. 2D materials on the other hand are lagging behind in this aspect as the nature of SOT in this ultrathin limit is still unclear [92]. With proposals for SOT devices based entirely on 2D materials [93, 94], a general microscopic theory for SOT in these systems is sorely needed.
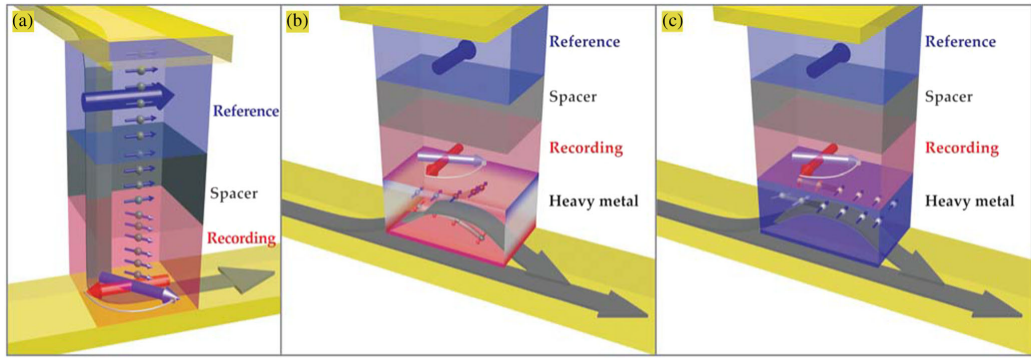
Figure 1.3: The various methods for electrical switching in a MTJ. (a) Using STT, electrons are first polarised via interaction with the reference FM layer (blue). A spin current then flows into the recording layer (red), where, via exchange interaction transfers its angular momentum to the local magnetisation, exerting a torque. After some time (switching time of the device) the recording and reference layer magnetisations are aligned. The SOT achieves the switching of the recording layer without using the reference layer. Instead, the polarisation happens by driving a charge current through a SOC-active layer which generates a non-equilibrium spin polarisation via the SHE (b) or the ISGE (c). Diagram from Ref.[95].

2D Materials in Spintronics

As the field of 2D materials established itself within the scientific community, their potential for spintronics applications became clear. Their low dimensionality is extremely useful for compact device fabrication but they hold much more potential than simply being used for their extreme thinness. Graphene is an excellent spin channel, being able to hold spin currents across lengths of micrometre scale [96, 97]. This long spin diffusion length is a result of both a high mobility of the charge carriers and a very weak intrinsic SOC (recent microwave measurements put it at 42 μeV [98]). On the other hand, this lack of a meaningful SOC does not allow for an easy control of the spin precession. For this reason, the enhancement of SOC in graphene without jeopardising its transport properties became a prominent topic of research [99].

Enhancing SOC in Graphene: van der Waals Heterostructures

The carbon atoms in a graphene layer are sp^2 hybridised, with these bonds providing the structural integrity of the system. Its electronic properties are vastly dominated by the electrons from the p_z orbitals. Initial attempts to increase the SOC in graphene drew some inspiration from another carbon compound: diamond, in which the carbon atoms are sp^3 hybridised and dis-

plays a much larger SOC (around 10 meV [100]). Doping the graphene layer with adatoms (e.g. hydrogen) would induce a distortion in the carbon lattice with local sp^3 hybridisation, increasing the SOC in the system [101]. Several more studies followed, concerning adatom decoration with heavier species ($3d$ and $5d$ transition metals) predicting further increase of the SOC together with a quantum anomalous Hall effect [102, 103]. However, experiments with heavy elements such as In [104, 105] and Ir [106] showed no evidence of a sizeable SOC-induced gap, likely due to the low diffusion barrier of adatoms that leads to their clustering [107] or intervalley scattering [108].

An alternative to adatom decoration is to make use of other 2D materials properties and layer-stacking them in what are known as van der Waals (vdW) heterstructures (Fig. 1.4) [109, 110]. Their name derives from the namesake forces that hold the different layers together (much like in the case of graphene/graphite). These structures have already been realised successfully. Graphene/hBN and graphene/WS$_2$ can be used as a field-effect tunnelling transistor [111, 112], and graphene/MoS$_2$ is a candidate for non volatile memory cells [113]. The fractional quantum Hall effect and the Hofstadter butterfly observed in graphene/hBN [114] are examples of the interesting phenomena these systems hold. The underlying principle behind this band structure engineering are proximity effects: the hybridisation of bands from different layers as electrons tunnel between them.

After the success of the first vdW heterostructures, it is vital to identify what are the ideal layer combinations. Monolayer TMDs seem to be great "partners" for graphene. These 2D materials are made up of three atomic layers: two chalcogen layers interposed by a transition metal layer. Each layer forms a triangular lattice, such that the crystal displays a honeycomb lattice akin to graphene's. However, the breaking of sublattice opens a gap in the band structure that can be bigger than 1 eV [115]. Furthermore, the presence of heavy metallic atoms leads to large SOC, with splitting of the valence bands on the order of hundreds of meV [116]. They are also hosts of a characteristic spin-orbit interaction known as the spin-valley coupling. This interaction is activated by the in-plane inversion asymmetry that is inherent in these materials with two different atomic species. The spin-valley interaction makes different extrema points in the momentum space (known as valleys, or K points) exhibit different spin-splitting [117]. Charge carriers can then be selectively excited from each valley by using circularly polarised light [118, 119] by making use of optical selection rules. As such, TMDs are considered prime candidates for applications in valleytronics and optoelec-
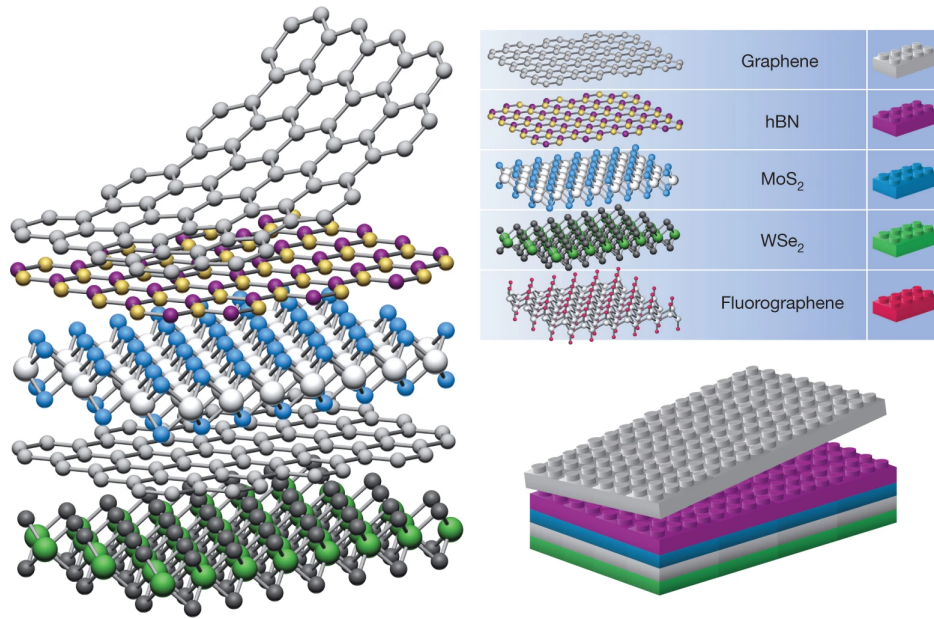
Figure 1.4: The simple yet powerful idea of stacking different 2D materials with the intent of combining different characteristics into one system. By carefully selecting which layers to use we can engineer many different band structure effects that allow for an array of different applications [109].

tronics.

Early first principles calculations predicted a SOC in graphene/TMD heterostructures up to 100 times bigger than in simple graphene. Not only that, but as the graphene states lie within the TMD gap, the Dirac nature of the charge carriers remains intact [98, 120, 121]. Experiments suggest an even bigger enhancement with reports of a decrease of spin relaxation time [122] and a giant spin lifetime anisotropy (SLTA) [51, 56, 57] indicating SOC of ~ 10 meV. The interface-induced spin-valley coupling is also present in these heterostructures, where optical spin injection has been already achieved [123], a testament to the success of proximity effect-based approaches.

Quantum Interference Effects: Weak Localisation

Coherent Backscattering

The concept of wave-particle duality of particles had a profound impact in physics since de Broglie associated a momentum-dependent wavelength to all particles. For electrons in particular, this duality is beautifully captured by electron diffraction [124, 125] first observed in 1927 and now widely

used as an experimental technique for structure analysis. Its classical counterpart has been known since the 17th century and is an example of wave interference.

Another manifestation of wave interference is coherent backscattering. When light travels through a medium with a large number of scatterers with size comparable to its wavelength, it will scatter off in every direction (the same effect that causes the glare when shining light into fog). As it does so, it interferes with itself generating a pattern around the cluster of scatterers that depends on the positions of each centre. Coherent backscattering is a general phenomenom wherein, regardless of the layout of the scatterers, there is constructive interference at a scattering angle $\theta = \pi$ relative to the incident source. This phenomenom also occurs with electrons scattering off impurities in disordered conductors, in what is known as weak localisation (WL)[2].

Coherent Interference of Electron Waves

Weak localisation is a negative correction to the conductivity of disordered systems when taking into account quantum interference effects. It stems from the interference between the different possible paths an electron can take through the scattering centers. It is evident that the conductivity of a material is related to the probability W of electrons to move from an initial point A to another point B. To do that the electrons can take several different paths. The total probability is then obtained by summing all the different paths contributions and then taking the modulus square:

$$W = \left| \sum_i w_i \right|^2 = \sum_{i,j} w_i w_j^* = \sum_{i=j} |w_i|^2 + \sum_{i \neq j} w_i w_j^*. \qquad (1.4)$$

The first term in Eq.(1.4) is the probability for the electron to take any path. This is the classical contribution, in which the paths are uncorrelated, and is the origin for the Drude contribution [129]. The second term takes into account the interference between all the different amplitudes and is inherently a quantum effect. Each path is associated with a phase so that vast majority of path pairs $i \neq j$ will have a large phase difference, and therefore, will average out when summing over all the paths. The exception

---

[2]Actually, the classical case with waves was observed after its quantum counterpart [126–128], since the $\theta = \pi$ peak can be very sharp making managing a source/detector system at such angles very challenging.

are path pairs that cancel each other's phase exactly, i.e. paths that are time reversal pairs, as depicted in Fig. 1.5. In this case the particle retraces the trajectory in reverse, which is only possible if the initial and final points A and B are the same. Considering two of these paths we have:

$$W_{CC} = |w_1|^2 + |w_2|^2 + w_1 w_2^* + w_2 w_1^* = 4|w_1|^2, \tag{1.5}$$

since the two amplitudes only differ by a phase: $\phi_1 = -\phi_2$. Equation (1.5) tells us that the probability of finding the particle in the same place after the scattering events is twice the value that one would get in the classical picture. There is a constructive interference increasing the likelihood of electrons remaining stuck in these loops, thus not contributing towards transport. Note that this is not a many body effect, but rather a phenomenom of self interference.

The theory of WL started in the end of the 1970s with Abrahams, Anderson, Licciardello and Ramakrishnan [130]. Using renormalisation theory they realised that the 2D case of electrons diffusing through random media is special: instead of a transition from a conducting to a localised regime at some critical disorder strength as in 3D, it has a crossover from a logarithmic localisation to the conventional exponential localisation. This peculiarity was already noted by Langer and Neal back in 1966 as a breakdown of perturbation theory for the resistivity [131]. Diagrammatic calculations soon followed [132, 133] that computed the full set of maximally crossed diagrams (for details see Chapter 2) confirming this result. The inclusion of SOC changes the problem interestingly. Hikami, Larkin and Nagaoka [134] showed that, if the spin and orbital degrees of freedom are strongly coupled, the interference becomes destructive instead. This is because spin states of the interfering waves are off-phase by 2π, as the spin rotates with the momentum. This phase difference, for fermions, leads to a minus sign and the quantum correction to the conductivity becomes positive in what is known as weak anti-localisation (WAL) [135]. These quantum coherence effects are only observable in 2D materials since in 3D there are more "escape routes" available out of the loops. Furthermore, they are low temperature effects as they hinge on electrons being able to maintain quantum coherence. The latter can only be maintained at lengths up to the coherence length L which decreases sharply with temperature. For systems much larger than the coherence length, the WL/WAL effects are the leading contributions towards the quantum corrections to electronic transport. The case where the coher-

ence length is larger than the system size falls outside of the scope of this work. It is the realm of mesoscopic physics where other quantum interference effects become relevant as well. Systems at this scale require a quantum treatment of their transport properties, yet statistical treatment is still adequate. Random matrix theory is a formalism to study such systems which exhibit features of quantum chaos [136–139].
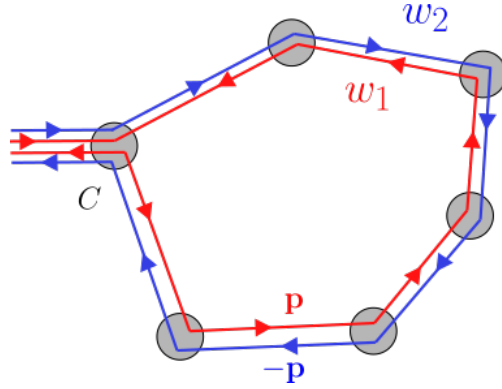
Figure 1.5: The localisation corrections arise when considering impurity loops that can be traversed anti-clockwise (w_1) or clockwise (w_2). If the system is time reversal invariant, the two paths have the same phase and interfere constructively, yielding an increased probability for electrons to remain in these loops. This manifests as a negative contribution to the conductivity of the system, known as weak localisation. Image adapted from Ref. [140].

Magnetic fingerprint of quantum interference

For most systems the WL corrections are, as the name indicates, a small change to the dominant (classical) conductivity. Nevertheless, it is possible to measure them by analysing the magnetoresistivity of the system at low temperatures. The perfect constructive/destructive interference is ensured by time reversal symmetry that connects the two ways of circling around a loop. Applying a magnetic field breaks this equivalence and introduces a phase:

$$W_{CC} = 2 \left| w \right|^2 \left[1 + \cos \left(2\varphi_B \right) \right], \tag{1.6}$$

which is given by the magnetic flux, Φ, enclosed in the loop: $\varphi_B = -e\,\Phi/\hbar$. When accounting for all the possible impurity loops this phase becomes effectively a random variable and the interference effects are suppressed, which translates to a peak in the magnetoresistivity curve for low temperature. A negative (positive) magnetoresistivity for low values of the magnetic

field is a sign of weak (anti)localisation. As such, WL corrections can be used to probe the strength of SOC in a material. The shape of the peak also holds valuable information about the system's coherence length, mean free path and spin diffusion length [141].

Quantum Interference Corrections in Dirac Materials

The interplay between different internal degrees of freedom is vital for quantum interference effects. Honeycomb lattices are made up of two triangular sublattices (A and B) from which emerges a spin-like DOF known as pseudospin, which characterises the electronic distribution over the two sublattices (e.g. the A sublattice is associated to the "up" pseudospin state). Furthermore, the already mentioned valley DOF (also known as isospin) is also present. In graphene, the presence of these DOFs dramatically changes the picture, as first pointed out by Ando and Suzuura [142]. If the valley DOF is ignored, graphene displays a WAL phase (without SOC), and only when opening the intervalley channel (e.g. with short range impurities) does it recover the traditional WL phase. Later, a theory of the quantum corrections to the magnetoresistivity was developed for graphene with pseudospin and isospin active impurities [143]. Such theories are vital for the accurate interpretation of magnetoresistivity experiments, widely used for the characterization of 2D materials and vdW heterostructures [141, 144–150]. Many more works followed, first extending the theory to include SOC in the band structure and impurities [151], and eventually moving to TMDs [152], vdW heterostructures [153] and even TI [154, 155]. However, the theories concerning graphene and vdW heterostructures are focused on the case of either weak SOC or disorder-induced SOC. Nonetheless, some experiments indicate that the SOC operative in these structures can be as large as 10 meV [150]. As such, a theory fully non-perturbative in the SOC is amiss and is one of the focus points of this thesis.

Goals and Outline

This thesis is centered around the effect of strong SOC in 2D Dirac systems, namely graphene-based vdW heterostructures with proximity-induced SOC and graphene/TMD/FM heterostructures. We will be focused on two different aspects: quantum interference effects in the former and SOT for the latter.

This work is organized as follows. We start by laying down the formalism used for the theoretical study of the above mentioned matters in Chapter 2. We will introduce a diagrammatic technique that allows us to treat, in a fully quantum mechanical manner, SOC and disorder non-perturbatively in the limit of dilute impurities. This is an extension to the standard diagrammatic formalism that is limited to weak disorder strength (Gaussian approximation) [156, 157]. In Chapter 3 we present the models used to study the different systems. We start with the simplest case of graphene and slowly build upon it until we reach the model for general honeycomb lattices of graphene/TMDs heterostructures coupled to FM. This is where band structure, spin texture, and other quantities will be discussed. Additionally, the effects of disorder in terms of self energy and propagators for the chosen approximations will also be analysed. Chapter 4 is dedicated to the study of quantum corrections to the conductivity in graphene with strong SOC. In order to build familiarity with the formalism we will start with conventional graphene in the presence of different types of disorder before we delve into the strong SOC case with the inclusion of valley-mixing scatterers. Spin orbit torque in graphene and vdW heterostructures coupled to FM is the subject of Chapter 5. To conclude, we summarise the main points achieved in this work and discuss possible extensions to this project in Chapter 6.

Chapter 2

Theory

2.1 Linear Response Theory: The Kubo Formula

Linear response theory is a widely used tool to compute how a system responds to a weak external perturbation $V(\mathbf{r}, t)$ that drives it out of equilibrium. It hinges in the simple idea that, if the perturbation is indeed small, the response should be linear in the applied field. The derivation of the Kubo formula assumes that there is only one frequency perturbing the system, however, this should not be seen as a limitation since, within linear response, different frequencies act independently of each other so that we need only sum the individual contributions of each frequency.

Let $\mathcal{H}_0$ be the Hamiltonian that is being probed by the external force and is time independent, and, from now on, we set $\hbar = 1$. Suppose now that the system is in some eigenstate $|\psi(t')\rangle$ of the unperturbed Hamiltonian when the external perturbation is switched on. Physically, this perturbation can be brought about by a field $\boldsymbol{h}(\boldsymbol{r}, t)$ that couples to some operator, $\mathcal{B}_\mu(\mathbf{r})$, as:

$$V(t) = \int \mathrm{d}^3\mathbf{r}\, \mathcal{B}_\mu(\mathbf{r})\, h_\mu(\boldsymbol{r}, t). \tag{2.1}$$

The dynamics of the system are now controlled by the full Hamiltonian $\mathcal{H} = \mathcal{H}_0 + V$. The expectation value of the observable $\mathcal{O}_\alpha$ at a time $t > t'$ is:

$$\langle \mathcal{O}_\alpha(\mathbf{r}, t)\rangle = \langle\psi(t)|\mathcal{O}_\alpha(\mathbf{r})|\psi(t)\rangle, \tag{2.2}$$

Since the perturbation is small, we can separate the time dependence of the state vectors into a fast, trivial, oscillatory component driven by $\mathcal{H}_0$ and a

slower one controlled by V. This owes itself to be treated using the interaction picture: $|\psi_I(t)\rangle = e^{i\mathcal{H}_0 t/\hbar}|\psi(t)\rangle$ (the state/operator on the rhs are in the Schrödinger picture). The time evolution of the states $|\psi_I(t)\rangle$ is controlled by the time evolution operator $\mathcal{U}(t, t')$:

$$|\psi_I(t)\rangle = \mathcal{U}(t, t')|\psi_I(t')\rangle. \tag{2.3}$$

This operator can be expanded using the Dyson's Series:

$$\mathcal{U}(t, t') = \mathcal{T}\left[\exp\left(-i/\hbar \int_{t'}^{t} \mathrm{d}t_1 V(t_1)\right)\right] \approx 1 - i\int_{t'}^{t} \mathrm{d}t_1\, V(t_1), \tag{2.4}$$

where $\mathcal{T}$ stands for the time ordering operator and we have linearised the exponential in V. Using Eq.(2.4) and (2.1) into (2.3) yields [158, 159]:

$$\langle\mathcal{O}_\alpha(\mathbf{r}, t)\rangle = \langle\mathcal{O}_\alpha(\mathbf{r})\rangle_0 + \int \mathrm{d}^3\mathbf{r}' \int_{-\infty}^{+\infty} \mathrm{d}t' \sum_\beta \mathcal{X}_{\alpha\beta}^R(\mathbf{r}, \mathbf{r}', t, t')h_\beta(\mathbf{r}', t'), \tag{2.5}$$

with the response function defined as:

$$\mathcal{X}_{\alpha\beta}^R(\mathbf{r}, \mathbf{r}', t, t') = -i\theta(t - t')\langle[\mathcal{O}_\alpha(\mathbf{r}, t), \mathcal{B}_\beta(\mathbf{r}', t')]\rangle. \tag{2.6}$$

The step function ensures causality and is equivalent to introducing the above mentioned switching on process explicitly in the time dependence of the perturbation. This result is easily extended for finite temperature by considering a canonical ensemble and the only difference is that the symbol $\langle\cdot\rangle$ now denotes a thermal average [160]. Since $\mathcal{H}_0$ is time independent, the response function will only depend on the time difference $t - t'$. Using the eigenstates of $\mathcal{H}_0$, $\mathcal{H}_0|n\rangle = E_n|n\rangle$ and going to the frequency domain we can recast Eq.(2.6) into its Lehmann representation:

$$\mathcal{X}_{\alpha\beta}^L(\mathbf{r}, \mathbf{r}', \omega = 0) = i\sum_{nm} \frac{\langle n|\mathcal{O}_\alpha(\mathbf{r})|m\rangle\langle m|\mathcal{B}_\beta(\mathbf{r}')|n\rangle}{E_n - E_m}\frac{f(E_m) - f(E_n)}{E_n - E_m + i0^+}, \tag{2.7}$$

having introduced the Fermi distribution function $f(E) = \left(1 + e^{E/k_B T}\right)^{-1}$.

In this thesis we are interested in spin/charge current responses of 2D systems to a constant and homogeneous electric field $\mathcal{E}$, in which case $\mathcal{B}$ is the charge current $J_\beta = -ev_\beta$, v_β being the velocity operator ($\beta = x, y$). We now make use of the fact that, in Dirac materials, the physical observables we are interested can be written solely in terms of the elements of the algebra.

Let us denote the elements of this d-dimensional algebra by $\{\gamma_i\}$, with $i = 0, \ldots, d-1$. For example, for $1/2$ spin fermions, $d = 16$ or 64 depending whether isospin is disregarded or not. The γ_i are matrices spanned by the tensor product between the different Pauli matrices, including the identity, which is γ_0. As such, they have dimensions $D \times D$, with $D = 8$ in the full case where we consider spin, pseudospin and isospin. The generalised response function is, from Eq.(2.7):

$$\mathcal{X}_{\alpha\beta}(\omega = 0) = i \sum_{nm} \frac{\langle n|\gamma_\alpha|m\rangle\langle m|\gamma_\beta|n\rangle}{E_n - E_m} \frac{f(E_m) - f(E_n)}{E_n - E_m + i0^+}. \tag{2.8}$$

The positive infinitesimal imaginary part assures the causality of the $\theta(t)$ and it singles out the contribution from the Fermi surface to the response function. To further work Eq.(2.8) we introduce the one particle propagators, known as the retarded/advanced Green's functions (GFs). They are extremely useful when tackling the problem of randomly distributed impurities and are defined as follows:

$$G^{R/A}_{\mathbf{p}}(\epsilon) = \frac{1}{\epsilon - \mathcal{H}_0 \pm i0^+} = \sum_n \frac{|n\rangle\langle n|}{\epsilon - E_n \pm i0^+}, \tag{2.9}$$

in the spectral representation. After recasting Eq.(2.8) in terms of GFs we arrive at a more useful version of the equation, the Kubo-Bastin formula [161]:

$$\mathcal{X}_{\alpha\beta} = i \int_{-\infty}^{+\infty} d\epsilon\, f(\epsilon)\, \text{Tr}\left\{\gamma_\alpha \frac{dG^R(\epsilon)}{d\epsilon}\gamma_\beta \delta(\epsilon - \mathcal{H}_0) - \frac{dG^A(\epsilon)}{d\epsilon}\gamma_\alpha \delta(\epsilon - \mathcal{H}_0)\gamma_\beta\right\}. \tag{2.10}$$

The Kubo-Bastin formula is more suited to treat disordered systems due to the presence of the GFs. From this equation one can identify two different contributions, in the form of the Kubo-Streda formula [162, 163]. In this form, the response function is separated into two different parts: $\sigma^{\gamma,\text{I}}_{\alpha\beta}$ that pertains to the contribution of the electrons at the Fermi surface, and $\sigma^{\gamma,\text{II}}_{\alpha\beta}$, which encodes the contribution from the whole Fermi sea:

$$\mathcal{X}^{\text{I}}_{\alpha\beta} = \frac{1}{4\pi}\text{Tr}\left\{\gamma_\alpha\left[G^R - G^A\right]\gamma_\beta G^A - \gamma_\alpha G^R \gamma_\beta\left[G^R - G^A\right]\right\}, \tag{2.11}$$

$$\mathcal{X}^{\text{II}}_{\alpha\beta} = \frac{1}{4\pi}\int_{-\infty}^{+\infty} d\epsilon\, f(\epsilon)\, \text{Tr}\left\{\gamma_\alpha G^R(\epsilon)\gamma_\beta \frac{dG^R}{d\epsilon} - \gamma_\alpha \frac{dG^R}{d\epsilon}\gamma_\beta G^R(\epsilon) + h.c.\right\}. \tag{2.12}$$

Equation 2.11 in particular will be at the core of this work as we explore different response functions for Dirac systems in the dilute impurity regime. The contribution from the Fermi sea, or the Berry phase contribution encodes the intrinsic response (i.e. of the clean system) and is sub-leading for diffusive processes that are mediated by impurity scattering. As such, the next section is devoted to the diagrammatic expansion technique, which allows to compute $\mathcal{X}^{\mathrm{I}}_{\alpha\beta}$ in the presence of a disordered potential.

2.2 Diagrammatic Expansion of Response Functions

The Hamiltonian of the unperturbed system we are studying is generally a combination of a bare term $\mathcal{H}_b$, coming from the periodic nature of the lattice (the general form of which is determined by the lattice's symmetries), and a disorder term U, originating from randomly distributed impurities:

$$\mathcal{H}_0 = \mathcal{H}_b + U. \tag{2.13}$$

The presence of the U term hampers the straightforward approach of directly using Eq.(2.9). Rather, one must take Eqs.(2.11) and (2.12) to be *disorder averaged*. In the thermodynamic limit, the disorder average of an operator $\langle \mathcal{O} \rangle$ is defined as:

$$\langle \mathcal{O} \rangle_{dis} = \lim_{N,\Omega \to \infty} \prod_{i=1}^{N} \int \frac{\mathrm{d}\mathbf{r}_i}{\Omega} \, \mathcal{O}\left(\mathbf{r}_i, ..., \mathbf{r}_N\right), \tag{2.14}$$

where the limit is taken such that the ratio between the number of impurities N and the system volume Ω is constant so that we have a finite impurity concentration $n = N/\Omega$. In this work we shall assume that the impurity scatterers are short-ranged, and follow some statistical distribution:

$$U\left(\mathbf{r}\right) = U \sum_{i=1}^{N} \delta\left(\mathbf{r} - \mathbf{r}_i\right), \tag{2.15}$$

here U can have a matrix structure (to include magnetic or SOC-active impurities for instance).

To illustrate the effects of this disorder average procedure let us look at the one particle Green's Function. Before impurity average, the GF is related to the transition amplitude between an electron in state $\mathbf{p}$ to a state $\mathbf{p}'$ and

can be written as a infinite series containing any number of scatterings:

$$G_{\mathbf{p},\mathbf{p}'} = G_{\mathbf{p}}^0 \delta_{\mathbf{p}\mathbf{p}'} + G_{\mathbf{p}}^0 U_{\mathbf{p}-\mathbf{p}'} G_{\mathbf{p}'}^0 + \sum_{\mathbf{q}} G_{\mathbf{p}}^0 U_{\mathbf{q}} G_{\mathbf{p}-\mathbf{q}}^0 U_{\mathbf{p}-\mathbf{q}-\mathbf{p}'} G_{\mathbf{p}'}^0 + ... \quad (2.16)$$

with G^0 being the free propagator, pertaining to the bare (clean) system $\mathcal{H}_b$ and $U_{\mathbf{q}}$ is the Fourier transform of $U(\mathbf{r})$. The above expression is made more transparent when viewed in its diagrammatic form, shown in Fig. 2.1. Upon disorder averaging, translational invariance is recovered and the impurities lines are "connected". Diagrammatically this is achieved by joining the impurities lines of each term in $G_{\mathbf{p},\mathbf{p}'}$ in all possible manners, as shown in Fig. 2.2. Here we define reducibility: the maximum number of propagator lines we can cut in a diagram such that we still end up with valid diagrams. Irreducible diagrams are the one in which we cannot cut any $G_{\mathbf{p}}^0$ line. We now write the disorder averaged propagator $\mathcal{G}_{\mathbf{p}}$ in terms of a Dyson-like series:

$$\mathcal{G}_{\mathbf{p}} = G_{\mathbf{p}}^0 + G_{\mathbf{p}}^0 \Sigma(\mathbf{p}) \mathcal{G}_{\mathbf{p}}, \quad (2.17)$$

where we have introduced the *Self Energy* of the system Σ. This quantity contains every irreducible diagram (without the external propagator line) and, if we were able compute it exactly, it would allow us to treat to problem of random short range scatterers exactly. The fact that this is not the case, however, should not be seen as a major impediment. The diagrammatic method provides a way of tuning into a particular transport regime by choosing which subsets of the full series we sum. The simplest choice is the Gaussian approximation, in which we only keep the diagrams with two potential lines (second diagram in Fig. 2.3) and is the limit of weak potential disorder. This approximation is equivalent to assuming the disorder

Figure 2.1: The electron propagator in the presence of disorder can be depicted as an infinite series of diagrams of free propagators (solid lines) going through any number of scattering events. In these, the electrons interact via the impurity potential (dashed lines) with the impurities (stars), changing their momentum state.

potential follows "white noise" statistics:

$$\langle U\left(\mathbf{r}\right) U\left(\mathbf{r}'\right)\rangle_{dis} = nu_0^2\delta\left(\mathbf{r}-\mathbf{r}'\right); \qquad \langle U\left(\mathbf{r}\right)\rangle_{dis} = 0. \qquad (2.18)$$

A more refined approach is known as the T-matrix approximation in which we keep all the one impurity diagrams.

$$T^{R/A} = \frac{U}{1 - Ug^{R/A}}, \qquad (2.19)$$

where we have defined the momentum integrated GF:

$$g^{R/A} = \frac{1}{\Omega}\sum_{\mathbf{p}} G^{R/A} \qquad (2.20)$$

In this way the self energy becomes $\Sigma^{R/A} = nT^{R/A}$. This allows the treatment of very strong potentials and any non-coherent single impurity scattering events, enabling us to capture scattering events that distinguish between left and right (relative to the electric field), known as skewness. Capturing this asymmetry is essential when looking for phenomena such as the SHE, where it is the scattering cross section for each spin projection favouring a particular direction that leads to the generation of the transverse spin current.

The reason why we can indeed only select a subset of all the diagrams but still get accurate result is the perturbative nature of the diagrammatic expansion in the dilute regime. Not only are there diagrams that encode multiple impurity scatterings so they are next order in the impurity concentration, but for the same order in n there is a hierarchy in place. This is the case of crossing diagrams, where potential lines cross. These depict coherent scattering between different impurities and are smaller than their non crossing counterparts by a factor of $(k_F\ell)^{-1}$ which is a small number for metals (here k_F is the Fermi momentum and ℓ is the mean free path). When impurity lines cross, the phase space volume available for the internal propagator line is much smaller since it is constrained by conservation of momentum

$$\mathcal{G}_{\mathbf{p}} = \text{---} + \text{---} + \text{---} + \text{---} + \text{---} + \text{---} + \cdots$$
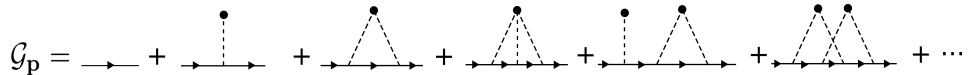
Figure 2.2: The disorder averaged GF contains every possible way of connecting impurity lines from $G_{\mathbf{p},\mathbf{p}'}$. This includes reducible diagrams (5th) and irreducible diagrams of one (2nd, 3rd and 4th) and multiple impurities (6th).

for two different scattering events at the same time. The crossing diagrams are related to quantum corrections that become increasingly important as $k_F\ell$ decreases. This quantity marks the transition between a system where the semi-classical picture adequately describes the electronic states and one where quantum effects need to be taken into account.

The computation of the self energy is the first step towards evaluating the response function. Once that is done the disorder averaged GF is simply:

$$\mathcal{G} = \frac{1}{(G^0)^{-1} - \Sigma}. \tag{2.21}$$

This expression can be used to recursively generate the rainbow diagrams of the self-consistent Born approximation, in which we first compute $\mathcal{G}$ in the Gaussian approximation and then re-insert it in Eq.(2.21) replacing G^0, and repeating the process. This however, amounts to a correction of order $(k_F\ell)^{-1}$ to the Gaussian self energy, so we shall ignore it.

2.2.1 Vertex Corrections and the Diffuson

We have seen how the disorder average procedure can be done by connecting impurity lines. We now apply the same procedure to the response function in Eq.(2.11). Now we can connect impurity lines coming from the same or different fermionic propagators, i.e. G^R and G^A. The first case is taken care of by using the disorder averaged GF as the propagator lines: $G^{R/A} \to \mathcal{G}^{R/A}$. The latter case, on the other hand, pertains to the connecting diagrams, and again we will work within a subset of diagrams that we can sum and that will encode the phenomena we are interested in. In the Gaussian approximation mentioned, for example, we keep only the "ladder diagrams", depicted in Fig. 2.4. Similarly to the self energy discussion, other diagrams contribute to next order in the diagrammatic expansion. We will discuss the connecting
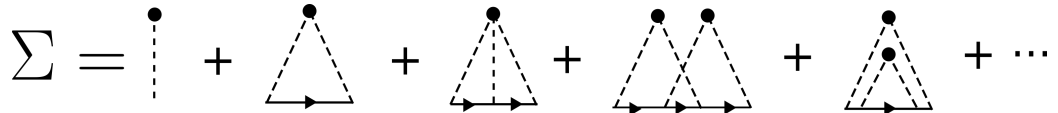
Figure 2.3: The skeleton expansion of the self energy. By recursively inserting it into the Dyson equation we generate the disorder averaged GF. The choice of what diagrams we keep in the self energy determines which regime/approximation we go into. The Gaussian approximation refers to keeping only the second diagram (second order in the impurity potential) whereas the T-Matrix is given by all the single impurity diagrams (e.g. 1st, 2nd, 3rd diagrams).

Figure 2.4: The response function is given by a product of GF connected via the two vertexes $\gamma_{\alpha,\beta}$ and via impurity lines. In the Gaussian approximation (depicted) we only keep the "ladder diagrams". Equivalently we can include all the ladders in a "bare bubble" with the renormalised vertex $\tilde{\gamma}_\beta$ which is defined recursively as shown in the bottom line.

crossing diagrams and their role in quantum corrections later on, in Section 2.3.3.

The connecting diagrams are typically taken into account by incorporating them into a renormalised vertex $\tilde{\gamma}_i$ which generates recursively the desired scattering processes (see bottom of Fig. 2.4). As such, the response can then be computed using the renormalised vertex as:

$$\mathcal{X}_{\alpha\beta} = \frac{1}{2\pi} \sum_{\mathbf{p}} \text{Tr} \left\{ \gamma_\alpha \mathcal{G}_{\mathbf{p}}^R \tilde{\gamma}_\beta \mathcal{G}_{\mathbf{p}}^A \right\}. \tag{2.22}$$

We have neglected the terms mixing GF from different sectors. The other terms $G^a G^a$ in Eq.(2.11) are subdominant since the two GF involved are analytical in the same half of the complex plane.

The renormalised vertex satisfies a Bethe-Salpeter equation. Within the T-Matrix approach it has the following form:

$$\tilde{\gamma}_i = \gamma_i + n \sum_{\mathbf{p}} \mathcal{G}_{\mathbf{p}}^R T^R \tilde{\gamma}_i T^A \mathcal{G}^{\mathcal{A}}{}_{\mathbf{p}}. \tag{2.23}$$

The renormalised vertex $\tilde{\gamma}_i$ includes an infinite series of non-coherent scatterings (and therefore is more general than the standard ladder approximation). This is formally achieved via substitution of the impurity lines in the ladder series by T-Matrix insertions [164].

An alternative method that bypasses the sum in Eq.(2.22) is the *Diffuson* method, which was first developed in the context of 2DEG with Gaussian impurities (ladder approximation) [165]. The method can be generalised for

Dirac systems within the T-Matrix approximation [166]. This makes use of the fact that we can write the operators in terms of algebra elements, including the renormalised vertex, such that $\tilde{\gamma}_i = \sum_j c_{ij}\gamma_j$. Projecting Eq.(2.23) onto the basis set yields:

$$
\begin{aligned}
c_{\beta\rho} &= \delta_{\beta\rho} + \sum_{\delta} c_{\beta\delta} \sum_{\mathbf{p}} \frac{n}{D} \text{Tr}\left\{ T^R G^R \gamma_\delta G^A T^A \gamma_\rho \right\} \\
&= \delta_{\beta\rho} + \sum_{\delta} c_{\beta\delta} \mathcal{M}_{\delta\rho},
\end{aligned}
\tag{2.24}
$$

with

$$
\mathcal{M}_{\delta\rho} \equiv \frac{n}{4} \sum_{\mathbf{p}} \text{Tr}\left\{ T^R G^R \gamma_\delta G^A T^A \gamma_\rho \right\}.
\tag{2.25}
$$

Here c is a matrix whose lines are the coefficients for the different renormalised vertices, and the elements of the algebra are matrices with dimensions $D \times D$. We can rewrite $\mathcal{M}$ by introducing two new matrices:

$$
\mathcal{N}_{\alpha\beta} = \frac{1}{D} \text{Tr}\left\{ G^R \gamma_\alpha G^A \gamma_\beta \right\},
\tag{2.26a}
$$

$$
\Upsilon_{\alpha\beta} = \frac{n}{D} \text{Tr}\left\{ T^R \gamma_\alpha T^A \gamma_\beta \right\},
\tag{2.26b}
$$

which allow us to write $\mathcal{M} = \mathcal{N} \cdot \Upsilon$[1]. The response function can then be computed entirely from only $\mathcal{N}$ and Υ:

$$
\begin{aligned}
\mathcal{X}_{\alpha\beta} &= \frac{1}{2\pi} \sum_{\mathbf{p}} \text{Tr}\left\{ \gamma_\alpha \mathcal{G}^R_{\mathbf{p}} \tilde{\gamma}_\beta \mathcal{G}^A_{\mathbf{p}} \right\} \\
&= \frac{1}{2\pi} \sum_{\rho} c_{\beta\rho} \sum_{\mathbf{p}} \text{Tr}\left\{ \gamma_\alpha G^R \gamma_\rho G^A \right\} \\
&= \frac{D}{2\pi} \left[c \cdot \mathcal{N} \right]_{\beta\alpha} \\
&= \frac{D}{2\pi} \left[(c-1)\,\Upsilon^{-1} \right]_{\beta\alpha} \\
&= \frac{D}{2\pi} \left[\left((1 - \mathcal{N}\Upsilon)^{-1} - 1 \right) \Upsilon^{-1} \right]_{\beta\alpha}.
\end{aligned}
\tag{2.27}
$$

Finally we introduce the *Diffuson* matrix $\mathcal{D} = (1 - \mathcal{M})^{-1}$ to arrive finally at:

---

[1]It is easy to see that, for any matrices A, B, C and D:

$$
\begin{aligned}
\text{Tr}\left\{ A\sigma^\alpha B\sigma^\beta \right\} \text{Tr}\left\{ C\sigma^\beta D\sigma^\gamma \right\} &= A_{ab}\sigma^\alpha_{bc} B_{cd}\sigma^\beta_{da} C_{ef}\sigma^\beta_{fg} D_{gh}\sigma^\gamma_{he} \\
&= 2\,C_{ea}A_{ab}\sigma^\alpha_{bc}B_{cd}D_{dh}\sigma^\gamma_{he} \\
&= 2\,\text{Tr}\left\{ CA\sigma^\alpha BD\sigma^\gamma \right\},
\end{aligned}
$$

where we have used the property of Pauli Matrices $\sigma^\alpha_{ab}\sigma^\alpha_{cd} = 2\delta_{ad}\delta_{bc}$.

$$\mathcal{X}_{\alpha\beta} = \frac{D}{2\pi} \left[\left(\mathcal{D} - 1 \right) \Upsilon^{-1} \right]_{\beta\alpha}. \tag{2.28}$$

The Gaussian limit is easily obtainable by setting $\Upsilon = nu_0^2/4$. This T-Matrix approximation is a more general and powerful framework that allows access to the strong impurity potential regime, even capturing the unitary limit $u_0 \to \infty$ (the case of vacancies) [167–169].

Equation (2.28) provides a clear and straightforward way to access any response function at semi-classical level from the Diffuson matrix. The Diffuson encodes information about how the different physical quantities in the system (the ones described by the algebra elements γ_i) diffuse and how they are coupled. As such, it can be used to derive the continuity and diffusion equations of the system if we include the frequency and momentum response.

We shall make use of this formalism when we look into the non-equilibrium spin density response of different systems to an external electric field. The study of quantum effects, however, requires us to go beyond single impurity scattering events and take into account coherent scattering. This shall be the focus of the next section.

2.3   Quantum Effects in Disordered Conductors

Resistivity in metals is a simple result of the fact that electrons, when moving in the presence of some driving force, encounter obstacles within the medium they are trying to traverse. At room temperature the main contribution for resistivity comes from electron-phonon scattering, in other words, lattice vibrations. The dependence of the phonon density with temperature is then passed on to the resistivity. As temperature decreases electron-phonon interactions become less and less important. However, resistivity never reaches zero, instead, at near zero temperature, it remains finite. This residual resistivity comes from lattice imperfections and from the scattering between electrons and impurities. This is even more so in graphene, since the electron-phonon coupling is weak even at room temperature [170–173]. Another famous effect of impurities on the resistivity is known as the Kondo effect [174], wherein the scatering off magnetic impurities results in a resistivity minimum at finite temperatures. This is the reason why a meaningful description of electronic transport must take impurities into consideration. Besides, as was already mentioned, very frequently impurities are not an

unwanted factor but actually the main ingredient that enable some physical phenomena.

2.3.1 The Semi-Classical Picture

In the Drude-Sommerfeld picture, electrons in a metal form a gas of non-interacting particles that move freely between collisions with the impurities. The collisions are taken to be instantaneous and the effect of impurities is included in a momentum relaxation time τ_p, which is the average time between scattering events. The mean free path is then given by $\ell = v_F \tau_\mathrm{p}$, where v_F is the Fermi velocity. If we apply an electric field $\mathcal{E}$, these particles will move according to the following equation of motion:

$$m\frac{\mathrm{d}\boldsymbol{v}}{\mathrm{d}t} = -e\boldsymbol{\mathcal{E}} - \frac{m}{\tau_\mathrm{p}}\boldsymbol{v}, \tag{2.29}$$

with $-e < 0$ the electron charge and $\boldsymbol{v}$ the velocity of the electron. Restricting ourselves to the steady state, $\frac{\mathrm{d}v}{\mathrm{d}t} = 0$, one immediately gets:

$$\boldsymbol{v} = -\frac{e\tau_\mathrm{p}}{m}\boldsymbol{\mathcal{E}}. \tag{2.30}$$

From the expression for the charge current $\mathbf{J} = -N_e e \boldsymbol{v} = \sigma \boldsymbol{\mathcal{E}}$, we can read the Drude conductivity:

$$\sigma = \frac{N_e e^2 \tau_\mathrm{p}}{m}, \tag{2.31}$$

where N_e is the electron density of the metal. It is worth to stress that this expression tells us that the conductivity is linear in τ_p. Generally, in the absence of magnetic fields, we get that τ_p must be inversely proportional to the impurity density: $\tau_\mathrm{p} \sim \frac{1}{n}$, which implies that the Drude conductivity is of the order $1/n$, a signature feature of a semi-classical contribution. There were several assumptions made in order to arrive at Eq.(2.31): we assumed that, between collisions, electrons are described by non-interacting classical particles, and collisions occur instantaneously with a probability τ_p^{-1} per unit time and are independent of each other.

Neglecting the electron-electron interactions is justified within Landau's Fermi Liquid theory in which the interacting system is equivalent to quasi-particles whose ground state is the non-interacting system. In this picture, one is allowed to make the non-interacting approximation with a simple renormalisation of certain physical quantities such as electronic mass and magnetic moment of the electron gas. For Dirac fermions, the properties of

the Fermi liquid depends on the charge carrier density. At the Dirac point, where the spectral weight vanishes, the system is marginally Fermi liquid, while away from that point, system behaves as a conventional Fermi liquid [8]. The presence of disorder changes the renormalisation parameters but does not break the Fermi liquid phase [175, 176].

Treating electrons as classical particles can be justified as follows. Wave packets move classically if the uncertainty in momentum Δk is much smaller than the momentum itself, k_F. If we take the position uncertainty Δx to be given by the mean free path $\ell = v_F \tau_\mathrm{p}$, where v_F is the Fermi velocity, and we use the uncertainty relation $\Delta x \Delta k > 1/2$ we have: $\frac{1}{2l} < \Delta k \ll k_F$, and so we have our condition for classical electrons:

$$k_F \ell \gg 1. \tag{2.32}$$

Equivalently, the above condition implies that the semi-classical description is valid when the electron wavelength is much smaller than the mean free path $\lambda_F \ll \ell$. Therefore, we can treat electrons as classical particles in systems with dilute impurity densities. As disorder increases we expect quantum effects to become relevant. In fact, this semi-classical result is only the leading term in the expansion of the conductivity in terms of the small parameter $(k_F \ell)^{-1}$. As the impurity concentration increases some electrons states become localised, thus not contributing to conduction. Eventually this leads to an insulating phase in what is known as Anderson localisation [177]. In three dimensions this localisation occurs when the impurity concentration surpasses a given critical value, whereas in one and two dimensions any amount of disorder (in the absence of SOC and disorder correlations) will induce localised states in the thermodynamic limit at zero temperature [178, 179].

2.3.2 Semi-Classical Boltzmann Equation

The Boltzmann formalism allows us to study semi-classical electronic transport properties via a statistical description of the system in terms of a distribution function $f(\mathbf{r}, \mathbf{p}, t)$. This function encodes the probability density for finding a particle in a small region of the phase space centered around momentum $\mathbf{p}$ and position $\mathbf{r}$ at time t. We will use make use of the Boltzmann equation to gain some physical intuition about the mechanisms behind the SOT terms in Chapter 5. This formalism is capable of capturing semi classical responses which are determined primarily by the distortion of the Fermi

surface of the system as a response to an external driving force. In our case the driving force is provided by the external electric field $\mathcal{E}$ and, considering a stationary state for a homogeneous system, the linearised equation reads [180]:

$$- e\boldsymbol{v} \cdot \boldsymbol{\mathcal{E}} \delta \left(\epsilon - \epsilon_{\mathbf{p}} \right) = n \int \mathrm{d}\mathbf{p}' W_{\mathbf{p}\mathbf{p}'} \left(\delta f_{\mathbf{p}} - \delta f_{\mathbf{p}'} \right), \qquad (2.33)$$

with the short-hand notation $f_{\mathbf{p}} \equiv f \left(\mathbf{r}, \mathbf{p}, t \right)$ and having defined the transition amplitude

$$W_{\mathbf{p}\mathbf{p}'} = 2\pi \left| \langle \mathbf{p} | T | \mathbf{p}' \rangle \right|^2 \delta \left(\epsilon_{\mathbf{p}} - \epsilon_{\mathbf{p}'} \right), \qquad (2.34)$$

with T being the T-Matrix of the system and the change of the Fermi surface due to the external field is $\delta f_{\mathbf{k}}$. This distortion can be written in terms of a harmonic expansion in the momentum angle parameterised by relaxation times. In general, the crux of the problem lies in finding these relaxation times. As such, we can use the following expression for the Fermi surface distortion:

$$\delta f_{\mathbf{p}} = \delta \left(\epsilon - \epsilon_{\mathbf{p}} \right) v_{\mathbf{p}} \left(\tau_{\parallel} \hat{\mathbf{p}} \cdot \boldsymbol{\mathcal{E}} + \tau_{\perp} \hat{\mathbf{p}} \times \boldsymbol{\mathcal{E}} \right). \qquad (2.35)$$

The distortion of the Fermi surface along the direction of the electric field is controlled by the longitudinal transport time $\tau_{\parallel}$ whereas transverse distortion (skewness) is parameterised by the skewscattering time $\tau_{\perp}$ [168]. In an isotropic system there are only these first order harmonics. When the Fermi surface is anisotropic there can be any number of harmonics. With the distortion of the distribution function we can compute the non-equilibrium spin density that is generated by the electric field via:

$$\delta S_i = \sum_{\alpha} \int \frac{\mathrm{d}\mathbf{p}}{4\pi^2} \langle s_i \rangle_{\alpha\mathbf{p}} \delta f_{\alpha\mathbf{p}}, \qquad (2.36)$$

where we have introduced a band label α to account for multiband systems and denoted the expectation value of the spin operator s_i in band α as $\langle s_i \rangle_{\alpha\mathbf{p}}$. Through Eqs.(2.35) and (2.36) one can predict what kind of responses are active and which mechanisms activate them based on the harmonics present in the spin texture. As such we will not actually compute the relaxation times but rather see which responses each time can activate.

Figure 2.5: The series of maximally crossed diagrams, known as the Cooperon, that encodes the weak localization corrections, the dominant quantum interference processes.

2.3.3 Quantum Effects within Diagrammatic Theory: The Cooperon

To capture the quantum effects in the response function one needs to go beyond the ladder diagrams. The diagrams that need to be considered are the maximally crossed diagrams whose series is known as the Cooperon. These are multiple impurity scattering diagrams where each impurity line crosses every other once as shown in Fig. 2.5.

The reason these are the diagrams to consider can be traced back to its connection to the Diffuson. Time reversal symmetry ensures that the divergence at zero momentum of the Diffuson (the signature of charge conservation) is also present in the Cooperon [181]. In fact, this connection is made clear if we "twist" the lower fermionic line of the Cooperon diagrams, since the resulting diagrams form the ladder series of the Diffuson. For systems with a scalar GF, the Diffuson and the Cooperon are related via a simple change of variables. When the GF has a matrix structure this relation is more complex.

The Cooperon describes the scattering processes that contribute towards WL corrections. These are the dominant quantum interference phenomena in systems larger in size than the coherence length of electrons L. It is not possible to sum the maximally crossed diagrams within a vertex correction as we did for the ladder diagrams. Instead, we make use of the four point vertex function γ and we recast the Kubo-Streda formula as (summing over repeated indices):

$$\sigma = \frac{e^2}{2\pi\Omega} \sum_{\mathbf{p}\mathbf{p}'} \left[\mathcal{G}^A(\mathbf{p}) \, v_x(\mathbf{p}) \, \mathcal{G}^R(\mathbf{p})\right]_{\gamma\alpha} \Gamma^{\alpha\beta}_{\delta\gamma}(\mathbf{p}, \mathbf{p}') \left[\mathcal{G}^R(\mathbf{p}') \, v_x(\mathbf{p}') \, \mathcal{G}^A(\mathbf{p}')\right]_{\beta\delta}.$$

(2.37)

The four point vertex function is defined as

$$\Gamma^{\alpha\beta}_{\delta\gamma}(\mathbf{p}, \mathbf{p}') = \left\langle G^R_{\alpha\beta}(\mathbf{p}, \mathbf{p}') \, G^A_{\delta\gamma}(\mathbf{p}', \mathbf{p}) \right\rangle_{dis},$$

(2.38)

42

or, making use of the tensor product definition:

$$\Gamma\left(\mathbf{p}, \mathbf{p}'\right) = \left\langle G^R\left(\mathbf{p}, \mathbf{p}'\right) \otimes G^A\left(\mathbf{p}', \mathbf{p}\right)\right\rangle_{dis}. \tag{2.39}$$

The four point vertex function contains every diagram that connects the two fermionic lines. The way we perform the disorder average will determine which diagrams we capture. If we choose these to be the maximally crossed diagrams only, we single out the WL contribution to the conductivity. We denote the four point vertex function that only contains the Cooperon as $\mathcal{C}$. To sum the whole maximally crossed series we start by writing the first few diagrams[2]:

$$\begin{aligned}\mathcal{C}^{s_1 s_2}_{s_3 s_4}\left(\boldsymbol{Q}\right) = {} & n U_{s_1 s_2} U_{s_3 s_4} + n^2 \sum_{\mathbf{p}''} \left(U\mathcal{G}^R_{\mathbf{p}''}U\right)_{s_1 s_2} \left(U\mathcal{G}^A_{\boldsymbol{Q}-\mathbf{p}''}U\right)_{s_3 s_4} + \\ & n^3 \sum_{\mathbf{p}'', \mathbf{k}''} \left(U\mathcal{G}^R_{\mathbf{p}''}U\mathcal{G}^R_{\mathbf{k}''}U\right)_{s_1 s_2} \left(U\mathcal{G}^A_{\boldsymbol{Q}-\mathbf{p}''}U\mathcal{G}^A_{\boldsymbol{Q}-\mathbf{k}''}U\right)_{s_3 s_4} + ...\end{aligned} \tag{2.40}$$

The Cooperon depends only on a single momentum variable $\boldsymbol{Q} = \mathbf{p} + \mathbf{p}'$ which is the sum of initial and final momenta of the scattering process. Since we are looking at backscattering phenomena we expect the Cooperon momentum to be small: $Q \ll \mathrm{p}_F$. We are working within the possibility of the impurity potential U having a matrix structure defined on the space of the internal DOFs of the Dirac material. This will allow us to study what are the effects of intervalley scattering, for example, in Section 4.2.3. Going now to a two-particle space and using the property of tensor product $(a \cdot b) \otimes (c \cdot d) = (a \otimes c) \cdot (b \otimes d)$ we can write a recursive relation for the Cooperon:

$$\mathcal{C} = nU \otimes U + n \sum_{\mathbf{p}''} \left(U\mathcal{G}^R_{\mathbf{p}''}\right) \otimes \left(U\mathcal{G}^A_{\boldsymbol{Q}-\mathbf{p}''}\right)\mathcal{C}, \tag{2.41}$$

and thus the Cooperon admits the form:

$$\mathcal{C}\left(\boldsymbol{Q}\right) = \frac{\xi}{1 - \xi P\left(\boldsymbol{Q}\right)}, \tag{2.42}$$

where we have defined $\xi = nU \otimes U$. The recursive insertion for the Cooperon

---

[2]Since we are looking at homogeneous electric fields we do not include any momentum transfer between the upper and lower fermionic lines. Interestingly, one can show that the Cooperon is completely insensitive to such inhomogeneities as they can be absorbed in the summed momenta [160].

is:

$$P(\boldsymbol{Q}) = \sum_{\mathbf{p}''} \mathcal{G}^R_{\mathbf{p}''} \otimes \mathcal{G}^A_{\boldsymbol{Q}-\mathbf{p}''}. \tag{2.43}$$

In this way the computation of the Cooperon hinges primarily on finding $P(\boldsymbol{Q})$. What's more, this formalism allows us to easily study different impurity potentials once we have $P(\boldsymbol{Q})$, by using Eq.(2.42). Typically we take advantage of the fact that $\boldsymbol{Q}$ is small to expand $P(\boldsymbol{Q})$ in a power series:

$$P(\boldsymbol{Q}) \approx P^{(0)} + Q P^{(1)} + Q^2 P^{(2)}, \tag{2.44}$$

with $Q = |\boldsymbol{Q}|$. We shall use this expansion when we first apply this formalism to the simpler cases. However it is possible to compute $P(\boldsymbol{Q})$ without expanding in the Cooperon momentum, which is useful when dealing with systems with very strong spin-orbit coupling (see Section 4.3.3). For that we use the following identity:

$$P(\boldsymbol{Q}) = \int \frac{\mathrm{d}\theta_Q}{2\pi} \frac{i}{4} \tilde{\rho}(\epsilon) \left[\frac{1}{\mathcal{H}^2(\mathbf{p}_F) - \mathcal{H}^1(\boldsymbol{Q} - \mathbf{p}_F) + 2i\eta} - (1 \leftrightarrow 2)^\dagger \right]. \tag{2.45}$$

Here the superscripts represent the "two particle" subspaces that arise due to the tensor product present, for example, in Eq.(2.41), such that $\mathcal{H}^1 = \mathcal{H}_b \otimes 1_{D \times D}$ and $\mathcal{H}^2 = 1_{D \times D} \otimes \mathcal{H}_b$. The imaginary part of the self energy (which is assumed scalar for this expression) is given by η, the average density of states of the bands is $\tilde{\rho}$ and we are integrating over the angle of $\boldsymbol{Q}$. This identity holds within the limit of $Q \ll \mathrm{p}_F$ and the Fermi level ϵ much larger than the SOC. The proof of this expression is presented in Appendix E.

The Cooperon is a two particle object lending itself to be analysed in a two particle basis, i.e. as a singlet-triplet basis. We can look at the "dispersion" of Cooperon modes by studying the *Cooperon Hamiltonian* [182, 183]:

$$\mathcal{H}_C = 1 - \xi P. \tag{2.46}$$

The dispersion of the Cooperon modes can give us a lot of information regarding the mechanisms behind WL/WAL. Modes that vanish at zero momentum are called gapless and will tend to contribute the most to the conductivity correction since the Cooperon is peaked at $\boldsymbol{Q} \approx 0$. The way the gaps depend on the system parameters contains information about when WL/WAL transitions might occur, for example, how strong must the spin-

orbit coupling be for a system to display WAL (see Section 4.3).

2.3.4 The Kubo-Streda formula for Quantum Corrections

Having introduced and understood the structure of the Cooperon we can compute the quantum correction to the conductivity using:

$$\Delta\sigma = \frac{e^2}{2\pi\Omega}\mathrm{Tr}\left\{\sum_{\mathbf{p}}W\left(\mathbf{p},-\mathbf{p}\right)\cdot\sum_{\boldsymbol{Q}}\mathcal{C}\left(\boldsymbol{Q}\right)\right\}. \tag{2.47}$$

The remaining fermionic lines as well as the ladder-renormalised vertices comprise the weight matrix $\boldsymbol{W}$:

$$W_{\gamma\delta}^{\beta\alpha}\left(\mathbf{p},\mathbf{p}'\right) = \left[\mathcal{G}^A\left(\mathbf{p}\right)v_x\mathcal{G}^R\left(\mathbf{p}\right)\right]_{\gamma\alpha}\left[\mathcal{G}^R\left(\mathbf{p}'\right)v_x\mathcal{G}^A\left(\mathbf{p}'\right)\right]_{\beta\delta}. \tag{2.48}$$

The weight matrix has an important role in the quantum corrections: it determines the weight *and sign* of the Cooperon modes. We shall neglect the Cooperon momentum $\boldsymbol{Q}$ in W as it will only bring about higher order corrections since it is the Cooperon which carries the divergent contribution at small momentum. This divergence is a manifestation of charge conservation. Its presence should pose no practical problems for calculations as the Cooperon is an object bound by the two length scales: the mean free path and the coherence length; so that the $\boldsymbol{Q}$ sum in Eq.(2.47) is taken for $L^{-1} < Q < \ell^{-1}$. At low temperatures, the main contribution towards L are electron-electron interactions so we can indirectly include them via tuning the coherence length parameter.

Armed with this formalism we will analyse in Chapter 4 the quantum correction to the conductivity.

Chapter 3

Model Hamiltonians

3.1 Monolayer Graphene

We start with the highest symmetry level model of graphene to establish nomenclature and notation. This will also be the starting point for our study of weak localisation corrections in Dirac systems realised in vdW heterostrutures in Chapter 4.

Monolayer graphene is composed of carbon atoms arranged in a honeycomb lattice. This is not a Bravais lattice as it is composed of two interpenetrating triangular sub-lattices, shown in Fig. 3.1a. This feature is the root for the pseudospin/sublattice degree of freedom which distinguishes graphene from conventional metals/semi-conductors. The system belongs to the D_{6h} point symmetry group: is invariant under 6-fold rotations about the axis perpendicular to the plane plane ($\hat{z}$) and is inversion symmetric with respect to the transformation $\hat{z} \rightarrow -\hat{z}$. The reciprocal unit cell is a hexagon and the Fermi level of (undoped) graphene lies precisely at its vertices. These are known as Dirac points and there are only two non-equivalent ones ($\mathbf{K}$ and $\mathbf{K}'$), connected by time-reversal. This gives rise to yet another electronic degree of freedom in the continuum limit: the isospin/valley.

A low energy description of graphene focuses on momenta close to the $\mathbf{K}$ points. Let $\mathbf{p}$ be this momentum, as measured from the Dirac point. There are several possible representations for the graphene Hamiltonian depending on the basis of choice. The three most commonly used are presented in Table 3.1. The Hamiltonian for monolayer graphene around the Dirac points reads, in magic basis 2:
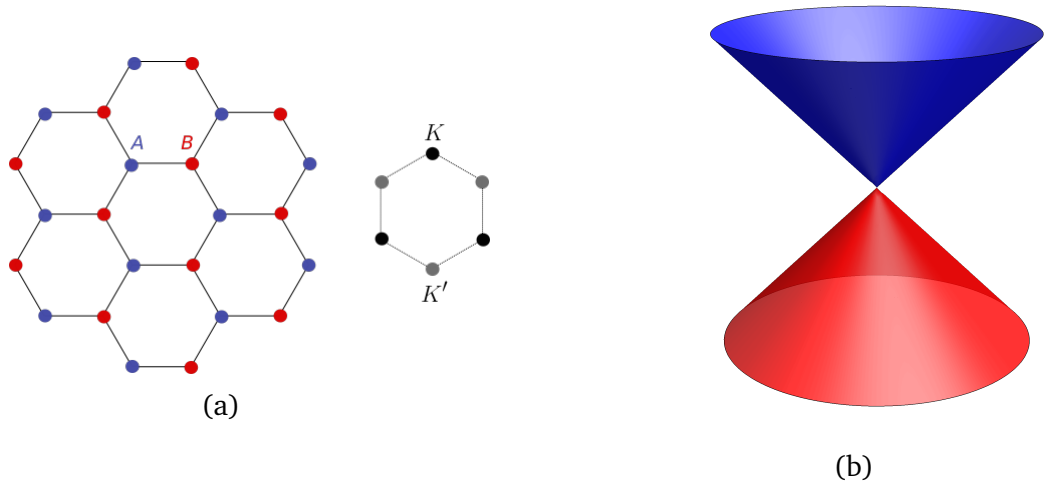
Figure 3.1: (a) The honeycomb lattice with its two triangular sublattices, A and B, highlighted in different colours. The hexagonal Brillouin zone is represented next to it, with two Dirac points, K and K', shown. The low energy theory of graphene is centered around these points. This is a continuum theory from which two extra SU(2) DOF are born: the pseudospin, related to the A/B sublattices and the isospin, dealing with the valleys K and K'. At the Dirac points the valence and conduction bands meet in a linear dispersion depicted in (b).

$$\mathcal{H}_{b,\mathbf{p}} = v\tau_0\boldsymbol{\sigma} \cdot \mathbf{p}, \tag{3.1}$$

where σ_i and τ_i, $i = 0, x, y, z$ are the Pauli matrices acting on, respectively, the pseudospin/sublattice and valley degrees of freedom introduced earlier, and $v \approx 10^6$m/s is the Fermi velocity of massless Dirac fermions. As per convention, we omit the tensor product symbol: $\tau_i\sigma_j \equiv \tau_i \otimes \sigma_j$. The energy bands take the characteristic linear shape $\epsilon_{\mathbf{p}} = \pm v\mathbf{p}$. In the absence of intervalley processes we can restrict ourselves to one valley, as we can just recover the effect of the other as a degeneracy factor at the end. It is worth pointing

Basis	Wallace	Magic 1	Magic 2
Ordering	$(A_{\mathbf{K}}, B_{\mathbf{K}}, A_{\mathbf{K}'}, B_{\mathbf{K}'})$	$(A_{\mathbf{K}}, B_{\mathbf{K}}, B_{\mathbf{K}'}, A_{\mathbf{K}'})$	$(A_{\mathbf{K}}, B_{\mathbf{K}}, -B_{\mathbf{K}'}, A_{\mathbf{K}'})$
$\mathcal{H}_{b,\mathbf{p}}$	$v\left(\tau_z\sigma_x\mathbf{p}_x + \sigma_y\mathbf{p}_y\right)$	$\tau_z v\boldsymbol{\sigma} \cdot \mathbf{p}$	$\tau_0 v\boldsymbol{\sigma} \cdot \mathbf{p}$

Table 3.1: The most common basis used to write the graphene Hamiltonian. The normal, or Wallace basis is the one originally used to study the band structure of graphene [184] but the Hamiltonian does not have a symmetrical form in the momentum directions. In the magic basis 1 and 2 the symmetry is present. Magic basis 2 shows that the valley is indeed a degenerate DOF. In this basis, the valley DOF is only explicitly present for the terms that truly depend on it.

out that intrinsic SOC is present in bare graphene, known as the Kane-Mele SOC [185]. This term however, is very small, leading to a spin-orbit gap of only 42μeV [98]. Proximity effects do enhance this term but it remains much weaker than other SOC [186, 187]. For this reason, we shall ignore it throughout this thesis.

3.1.1   Disorder effects

The D_{6h} graphene model will also be used as a practical introduction of the diagrammatic formalism of quantum corrections. These are brought about by impurities which we shall take to be δ-scatterers:

$$U\left(\mathbf{r}\right) = U\sum_i \delta\left(\mathbf{r} - \mathbf{R}_i\right). \tag{3.2}$$

We start by considering the simple case of scalar disorder such that $U = u_0\mathbf{1}$. As we have seen in Chapter 2, to treat disorder effects we need the disorder averaged Green's function which we can obtain from $G_{0\mathbf{p}}^{R(A)}$ system via:

$$\mathcal{G}_{\mathbf{p}}^a = \frac{1}{\left(G_{0\mathbf{p}}^a\right)^{-1} - \Sigma^a}, \tag{3.3}$$

where Σ^a is the self energy that must be computed within some approximation. Here, we will consider the Gaussian approximation which amounts to keeping only diagrams that are quadratic in the U: $\langle U\left(\mathbf{r}\right) U\left(\mathbf{r}'\right)\rangle_{dis} = nu_0^2\delta\left(\mathbf{r} - \mathbf{r}'\right)$. In this weak potential limit the self energy takes the simple form:

$$\Sigma_G^{R/A} = nu_0^2 g_0^{R/A}. \tag{3.4}$$

Here we have introduced the momentum integrated clean Green's function [164]:

$$
\begin{aligned}
g_0^{R/A} &= \int \frac{\mathbf{dp}}{4\pi^2}\, G_{0\mathbf{p}}^{R/A} \\
&= -\frac{\epsilon}{2\pi v^2}\ln\left|\frac{\Lambda}{\epsilon}\right| \mp i\frac{|\epsilon|}{4v^2},
\end{aligned} \tag{3.5}
$$

where Λ is an ultraviolet cutoff for the low energy theory [167]. In this case, the integrated GF is scalar and does not introduce any new matrix structures not present in $\mathcal{H}_b$, which will allow us to obtain the disorder averaged GF by

an analytical continuation of $G_{0\mathbf{p}}^a$. The momentum integrated GF defines the real and imaginary parts of the self energy:

$$\Sigma_G^{R/A} = \delta\epsilon \pm i\eta \tag{3.6}$$

the real part of the self energy, $\delta\epsilon$, is a small shift of the Fermi level which can be neglected [164, 166]. The imaginary part $\eta = nu_0^2\epsilon/4v^2$, on the other hand is the impurity broadening of the energy levels and is essential for the calculation. This broadening is related to the momentum scattering time $\tau_{\mathbf{p}} = \frac{1}{2\eta}$. Finally, the disorder averaged GF for graphene in the Gaussian approximation is [164]:

$$\mathcal{G}_{\mathbf{p}}^{R(A)} = \frac{1}{\epsilon - \mathcal{H}_{0,\mathbf{p}} - \Sigma_G^{R/A}} = \frac{\epsilon \pm i\eta + v\boldsymbol{\sigma} \cdot \mathbf{p}}{(\epsilon \pm i\eta)^2 - v^2\mathbf{p}^2}. \tag{3.7}$$

3.2 Graphene based Heterostructures: Proximity-Induced SOC

3.2.1 The C_{6v} Dirac-Rashba Model

The only spin-orbit interaction compatible with all symmetries of graphene, the famous Kane-Mele SOC [185], is too weak for practical purposes [98]. The Dirac-Rashba model, which arises when the inversion symmetry is broken along the direction normal to the plane, already allows for SOC in the bare system and is the main object of study in the topic of quantum corrections in Chapter 4. Such an asymmetry is achieved, for example, via placing the graphene layer on a suitable substrate. This breaks the mirror symmetry $\hat{z} \rightarrow -\hat{z}$ lowering the symmetry class from D_{6h} to C_{6v}. The graphene Hamiltonian is endowed with the Rashba SOC [42], turning it into what we call the Dirac-Rashba model. We will use this model to study the quantum corrections to the conductivity in graphene with strong SOC doped with scalar impurities in Section 4.3.

Model and Energy Bands

In the "magic basis 2" (see Table 3.1), the Hamiltonian for the clean system reads:

$$\mathcal{H}_{0\mathbf{p}} = \tau_0 v\boldsymbol{\sigma} \cdot \mathbf{p} + \alpha\tau_0 \left(\sigma_x s_y - \sigma_y s_x\right), \tag{3.8}$$
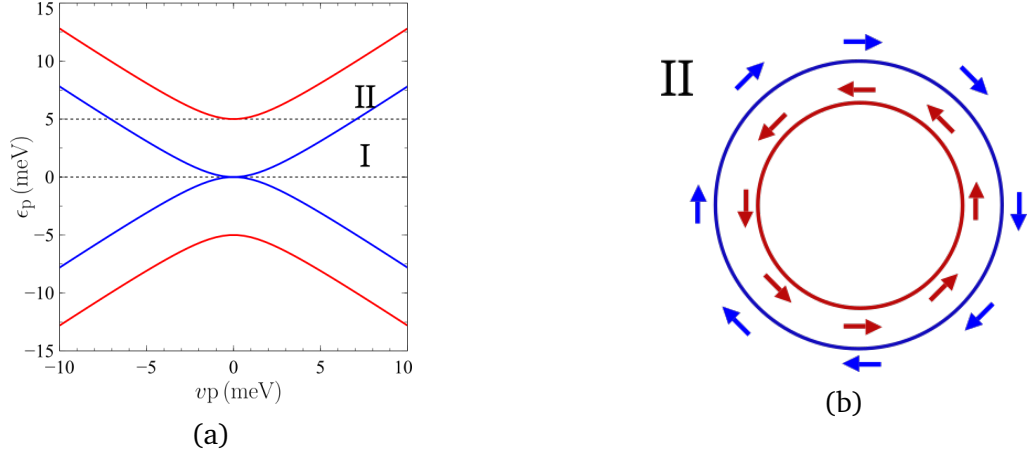
Figure 3.2: (a) The Dirac-Rashba model has spin degeneracy lifted by SOC with spin gap 2α. This introduces two energy regimes characterized by how many bands does the Fermi level cross, one in regime I and two in the case of regime II. In (b) it is shown a top view of the spin texture at the Fermi rings in regime II, with the characteristic in-plane winding of the spins around the Fermi surface.

where τ_0 is the 2×2 identity matrix acting on the valley DOF and σ_i, s_i are the Pauli matrices corresponding to the sublattice and spin degrees of freedom. The energy bands have the dispersion relation $\epsilon_\mathrm{p} = \lambda\left(\alpha + s\sqrt{v^2\mathrm{p}^2 + \alpha^2}\right)$, where $\lambda, s = \pm 1$ are the band labels. The Rashba SOC lifts the spin degeneracy creating a spin gap of 2α at the Dirac points. This introduces two different regimes, shown in Fig. 3.2a: Fermi energy ϵ inside (regime I) or outside this pseudo-gap (regime II). We will leave intervalley physics for later so we restrict the following discussion to a single valley $\tau_0 = 1$. To simplify the expressions and discussions we will also take the Fermi energy and the Hamiltonian couplings to be positive from now on.

The prominent feature of this model is the in-plane spin-momentum locking:

$$\langle \boldsymbol{s} \rangle_\mathbf{p} = \pm \frac{\sqrt{\epsilon\left(\epsilon \pm 2\alpha\right)}}{\epsilon \pm \alpha}\left(\hat{p} \times \hat{z}\right), \tag{3.9}$$

with $\pm$ standing for the spin majority (+) and minority (−) bands. The electrons spin is thus locked in plane, perpendicular to the direction of the momentum, winding around the Fermi surface with a well defined and opposite chirality for each band (Fig. 3.2b). For this reason, phenomena that hinge on this spin texture are typically stronger in regime I where all electrons have the same chirality [188].

Clean Green's Function

For ease of notation we define the 4×4 matrices $\gamma_{ij} = \sigma_i \otimes s_j$. These span an orthogonal basis for the matrix algebra and are at the same time the momentum independent operators for all the relevant observables, like charge/spin currents and spin densities. The presence of Rashba SOC generates new terms in the clean GF [166]:

$$\mathcal{G}_0^{R(A)} (\epsilon, \mathbf{p}) = \left. \frac{G_0^{\mathbf{p}} + G_0^{\theta}}{\left(\epsilon^2 - v^2 \mathbf{p}^2 \right)^2 + 4\epsilon^2 \alpha^2} \right|_{\epsilon \to \epsilon \pm i 0^+} . \tag{3.10}$$

We have separated the radial and angular components as:

$$G_0^{\mathbf{p}} = \epsilon \left(\epsilon^2 - v^2 \mathbf{p}^2 - 2\alpha^2 \right) \gamma_{00} + \alpha \epsilon^2 \gamma_R - 2\alpha^2 \epsilon \gamma_{33}, \tag{3.11a}$$

$$\begin{aligned} G_0^{\theta} =&\, 2\alpha \epsilon v \mathbf{p} \left(\gamma_{02} \cos \theta - \gamma_{01} \sin \theta \right) + v \mathbf{p} \left(\epsilon^2 - v^2 \mathbf{p}^2 \right) \left(\gamma_{10} \cos \theta + \gamma_{20} \sin \theta \right) + \\ &\, v^2 \mathbf{p}^2 \alpha \left[\sin \left(2\theta \right) \left(\gamma_{22} - \gamma_{11} \right) + \cos \left(2\theta \right) \left(\gamma_{12} + \gamma_{21} \right) \right], \end{aligned}$$
$$\tag{3.11b}$$

with $\gamma_R = \gamma_{12} - \gamma_{21}$. The momentum integrated GF is the foundation for the disorder averaging of the GF. It is comprised of 3 structures coming from the radial components as the angular terms vanish upon integration:

$$g^{R(A)} = g_0^{R(A)} \gamma_{00} + g_3^{R(A)} \gamma_{33} + g_R^{R(A)} \gamma_R, \tag{3.12}$$

with each term being given by:

$$\begin{aligned} g_0^{R(A)} =& -\frac{\epsilon}{8\pi v^2} \ln \left| \frac{\Lambda^4}{\epsilon^2 \left(\epsilon^2 - 4\alpha^2 \right)} \right| - \frac{\alpha}{8\pi v^2} \ln \left| \frac{\epsilon - 2\alpha}{\epsilon + 2\alpha} \right| \\ & \mp \frac{i}{4v^2} \left\{ \frac{\epsilon + \alpha}{2} \theta \left(2\alpha - \epsilon \right) + \epsilon \theta \left(\epsilon - 2\alpha \right) \right\}, \end{aligned} \tag{3.13a}$$

$$g_3^{R(A)} = -\frac{\alpha}{8\pi v^2} \ln \left| \frac{\epsilon - 2\alpha}{\epsilon + 2\alpha} \right| \mp i \frac{\alpha}{8v^2} \theta \left(2\alpha - \epsilon \right), \tag{3.13b}$$

$$g_R^{R(A)} = \frac{\epsilon}{16\pi v^2} \ln \left| \frac{\epsilon - 2\alpha}{\epsilon + 2\alpha} \right| \pm i \frac{\epsilon}{16v^2} \theta \left(2\alpha - \epsilon \right), \tag{3.13c}$$

where $\theta \left(x \right)$ is the Heaviside step function. The imaginary part is scalar in regime II which will lead to a scalar self-energy formally identical to the one in Eq.(3.4) in the Gaussian limit.

Disorder Averaged Green's Function

The T-Matrix formalism allows to capture the resonant-scattering limit. For this model, the T-Matrix $T^{R(A)} = \left[u_0^{-1} - g_0^{R(A)} \right]^{-1}$ acquires a matrix structure and the self energy becomes:

$$\Sigma^{R(A)} = (\delta\epsilon \mp i\eta_0)\,\gamma_{00} + (m_3 \mp i\eta_3)\,\gamma_{33} + (m_R \mp i\eta_R)\,\gamma_R, \tag{3.14}$$

with the components given by:

$$\delta\epsilon \approx nu_0^2 g_{0,r}^R, \quad \eta_0 \approx -nu_0^2 g_{0,i}^R, \tag{3.15a}$$

$$m_3 \approx nu_0^2 g_{3,r}^R, \quad \eta_3 \approx -nu_0^2 g_{3,i}^R, \tag{3.15b}$$

$$m_R \approx nu_0^2 g_{R,r}^R, \quad \eta_R \approx -nu_0^2 g_{R,i}^R, \tag{3.15c}$$

within the weak scattering regime ($u_0 \ll |g_0|^{-1}$). In regime II the self-energy is a scalar (neglecting the real part) just like in the bare graphene case, whereas in regime I there is a rich matrix structure that imprints a strong energy dependence on various response functions. The disorder averaged Green's Function is obtained via:

$$\mathcal{G}_{\mathbf{p}}^{R(A)} = \frac{1}{\epsilon - \mathcal{H}_0 - \Sigma^{R(A)}}. \tag{3.16}$$

The self energy in Eq.(3.14) has the same structure as $\mathcal{H}_0$ but with an extra term in γ_{33}. This means that we can obtain the disorder average GF for the original system if we instead compute the clean GF of a system with a mass term in γ_{33}:

$$\mathcal{H}_m = \mathcal{H}_0 + m\sigma_z s_z, \tag{3.17}$$

and then use the following substitution rules:

$$\epsilon \to \epsilon \pm i\eta_0, \quad \alpha \to \alpha + m_R \mp i\eta_R, \quad m \to m_3 \mp i\eta_3. \tag{3.18}$$

The clean GF for the massive system can be written as:

$$\mathcal{G}_m^{R(A)}(\epsilon, \mathbf{p}) = \left(G_m^{\mathrm{p}} + G_m^\theta\right)/\mathcal{L}^{R(A)}, \tag{3.19}$$

with the denominator being given by:

$$\mathcal{L}^{R(A)} = \left(v^2 p^2 - (\epsilon - m)(\epsilon - 2\alpha + m)\right)\left(v^2 p^2 - (\epsilon - m)(\epsilon + 2\alpha + m)\right), \tag{3.20}$$

52

and

$$G_m^{\text{p}} = \left[\epsilon \left(\epsilon^2 - m^2 - v^2\mathbf{p}^2 - 2\alpha^2 \right) + 2m\alpha^2 \right] \gamma_{00} + \alpha \left(\epsilon - m \right)^2 \gamma_R$$
$$- \left(2\alpha^2 \epsilon + m \left(m^2 + v^2\mathbf{p}^2 - \epsilon^2 - 2\alpha^2 \right) \right) \gamma_{33}, \tag{3.21a}$$

$$G_0^\theta = 2\alpha \left(\epsilon - m \right) v\mathbf{p} \left(\gamma_{02} \cos\theta - \gamma_{01} \sin\theta \right) +$$
$$+ v\mathbf{p} \left(\epsilon^2 - v^2\mathbf{p}^2 - m^2 \right) \left(\gamma_{10} \cos\theta + \gamma_{20} \sin\theta \right) +$$
$$+ v^2\mathbf{p}^2 \alpha \left[\sin\left(2\theta \right) \left(\gamma_{22} - \gamma_{11} \right) + \cos\left(2\theta \right) \left(\gamma_{12} + \gamma_{21} \right) \right], \tag{3.21b}$$

using the substitution (3.18).

3.2.2 The C_{3v} Generalised Dirac-Rashba Model

To describe more complex systems such as TMD monolayers and heterostructures like graphene/TMD, TMD/graphene/FM and TMD/FM, we lift some of the symmetry constraints which allow more terms in the Hamiltonian [187]. Systems with broken sublattice symmetry, such as TMDs, require a generalisation of the Dirac-Rashba model. The Hamiltonian is endowed with an orbital gap and a valley resolved SOC known as spin valley coupling. This general model, together with a proximity-induced exchange interaction, will be the starting point of our SOT analysis in Chapter 5.

Model and Energy Bands

Ferromagnetic Dirac vdW heterostructures can be described by the magnetised Dirac-Rashba Hamiltonian which reads as follows:

$$\mathcal{H}_b = v\boldsymbol{\sigma} \cdot \mathbf{p} + \alpha \left(\sigma_x s_y - \sigma_y s_x \right) + \Delta \tau_z \sigma_z - \Delta_{xc} \mathbf{m} \cdot \boldsymbol{s}, \tag{3.22}$$

in magic basis 2 from Table 3.1. Here, additionally to the Rashba SOC, brought about by the breaking of interfacial symmetry due to the FM film, there are several new energy scales. The breaking of sublattice symmetry that is present in TMDs is captured by the staggered on-site potential Δ which can open orbital gaps close to 2 eV in some samples [115]. Systems with broken inversion symmetry such as TMDs display spin-valley (SV) coupling $\lambda_{sv} \tau_z s_z$ which can be accounted for as a valley dependent Zeeman term. Note that, in order to allow a Dresselhaus-type term as discussed in Chapter 1 we would need further lower the symmetry level of the model.

The interaction between the spins of the 2D charge carriers and the local moments of the FM induces an exchange field that takes the form $-\Delta_{xc} \mathbf{m} \cdot \boldsymbol{s}$,

when assuming a mean field description of the FM magnetisation $\mathbf{m}$ [90, 92], where Δ_{xc} is the exchange coupling strength. The magnetisation direction can be set by a bias external field. The presence of this field complicates the calculations so we assume it is removed after setting $\mathbf{m}$. The presence of in-plane magnetisation $m_{x,y}$ breaks the rotational invariance of the system, inducing anisotropy and, as we will show in Chapter 5, will be crucial in activating a multitude of SOT terms. Without loss of generality we take the in-plane anisotropy to be along the $\hat{x}$-axis so that:

$$\mathbf{m} = m_x\,\hat{x} + m_z\,\hat{z} \equiv \sin\theta_{\mathbf{m}}\,\hat{x} + \cos\theta_{\mathbf{m}}\,\hat{z}. \tag{3.23}$$

The aforementioned spin-valley coupling can thus be included as $m_z \to m_z - \frac{\lambda_{sv}}{\Delta_{xc}}\tau_z$. In the absence of intervalley processes we can perform any calculations on the 4×4 space spanned by only the spin and pseudospin DOFs setting $\tau_z = \pm 1$ and then simply adding the outcomes. The interplay between all the energy scales gives rise to a variety of band structures with interesting features and different energy regimes. These can be accessed in gated devices which allow for an easy control of the carrier density via back-gate voltages [1, 189].

To simplify expressions we introduce $\tilde{\mathfrak{m}} = \mathfrak{m} + \tau_z \lambda_{sv}\hat{z}$ with $\mathfrak{m} = -\Delta_{xc}\mathbf{m}$. A typical band structure is shown in Fig. 3.3a and comprises four distinct spectral regions (for illustration purposes we take $\alpha > \tilde{\mathfrak{m}}_z \gg \mathfrak{m}_x$):

- Regime Ia: Only present in the anisotropic case. This is a low energy regime where the Fermi level crosses an electron/hole pocket that is situated away from the $\mathbf{K}$ point. It is contained within the energies:

$$\epsilon_{\text{Ia}} < |\epsilon| < \epsilon_{\text{Ib}}; \tag{3.24}$$

- Regime Ib: A distorted "Mexican Hat". Very narrow energy range where the Fermi level crosses two different Fermi rings both belonging to the spin majority band. This happens for:

$$\epsilon_{\text{Ib}} < |\epsilon| < \epsilon_{\text{Ic}}; \tag{3.25}$$

- Regime Ic: Intermediate regime where the Fermi level crosses only the spin majority band, hinting at stronger spin density responses for

$$\epsilon_{\text{Ic}} < |\epsilon| < \epsilon_{\text{II}}; \tag{3.26}$$

54
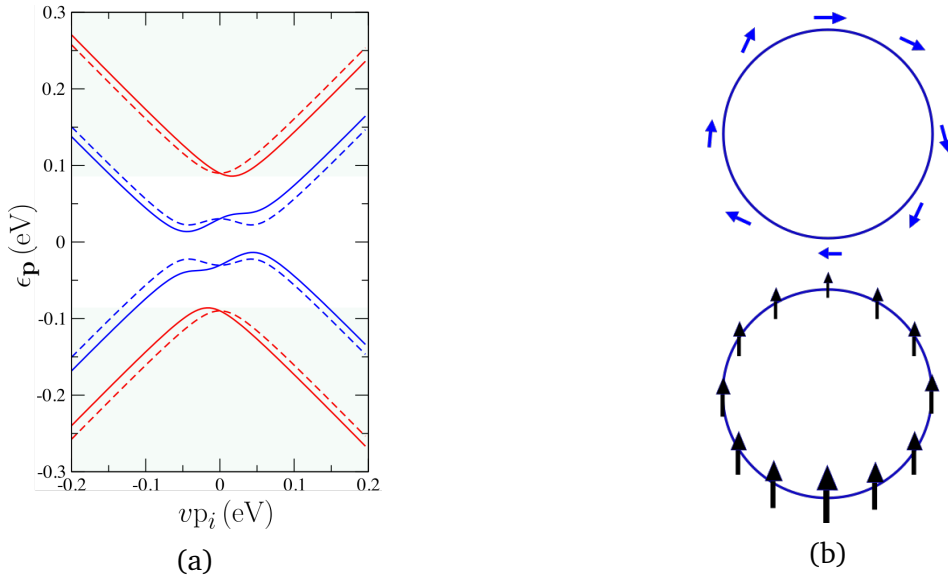
Figure 3.3: (a) The typical magnetised generalised Dirac-Rashba band structure along the anisotropy direction as the full lines ($\hat{y}$ for in-plane magnetisation along $\hat{x}$) and along $\hat{x}$, as dashed lines, showing the distorted mexican hat. The shaded region highlight the spectral region II. This is an example of a TMD|graphene|FM heterostructure with $\alpha = 40$ meV, $\mathfrak{m}_z = 30$ meV and $\mathfrak{m}_x = 20$ meV. (b) The spin texture for the spin majority band. The in-plane spin (top) shows a locking that resembles the one from the Dirac-Rashba model but with a small deviation due to m_x. The presence of m_z and Δ induces an out-of plane spin (black arrows, bottom) that is modulated by the in-plane magnetisation. For visual effect, the impact of m_x is exaggerated.

Regime	$\Delta = 0$	$\Delta \neq 0$
ϵ_{II}	$\sqrt{\tilde{\mathfrak{m}}_z^2 + 4\alpha^2}$	$\tilde{\mathfrak{m}}_z + \Delta$
ϵ_{Ic}	$\tilde{\mathfrak{m}}_z + \frac{\mathfrak{m}_x^2}{2\tilde{\mathfrak{m}}_z}$	$\sqrt{(\Delta - \tilde{\mathfrak{m}}_z)^2 + 4\alpha^2}$
ϵ_{Ib}	$\frac{\tilde{\mathfrak{m}}_z \alpha}{\sqrt{\tilde{\mathfrak{m}}_z^2 + \alpha^2}} + \frac{\alpha \mathfrak{m}_x \tilde{\mathfrak{m}}_z \sqrt{2\alpha^2 + \tilde{\mathfrak{m}}_z^2}}{(\alpha^2 + \tilde{\mathfrak{m}}_z^2)^{3/2}}$	$\frac{\alpha(\Delta + \tilde{\mathfrak{m}}_z)}{\sqrt{\alpha^2 + \tilde{\mathfrak{m}}_z^2}} + \frac{\alpha \mathfrak{m}_x \sqrt{\tilde{\mathfrak{m}}_z(\Delta + \tilde{\mathfrak{m}}_z)(2\alpha^2 + \tilde{\mathfrak{m}}_z^2 - \Delta \tilde{\mathfrak{m}}_z)}}{(\alpha^2 + \tilde{\mathfrak{m}}_z^2)^{3/2}}$
ϵ_{Ia}	$\frac{\tilde{\mathfrak{m}}_z \alpha}{\sqrt{\tilde{\mathfrak{m}}_z^2 + \alpha^2}} - \frac{\alpha \mathfrak{m}_x \tilde{\mathfrak{m}}_z \sqrt{2\alpha^2 + \tilde{\mathfrak{m}}_z^2}}{(\alpha^2 + \tilde{\mathfrak{m}}_z^2)^{3/2}}$	$\frac{\alpha(\Delta + \tilde{\mathfrak{m}}_z)}{\sqrt{\alpha^2 + \mathfrak{m}_z^2}} - \frac{\alpha \mathfrak{m}_x \sqrt{\tilde{\mathfrak{m}}_z(\Delta + \tilde{\mathfrak{m}}_z)(2\alpha^2 + \tilde{\mathfrak{m}}_z^2 - \Delta \tilde{\mathfrak{m}}_z)}}{(\alpha^2 + \tilde{\mathfrak{m}}_z^2)^{3/2}}$

Table 3.2: Spectral regimes of the C_{3v} model. To ease the notation, all couplings are taken to be positive.

- Regime II: High energy regime which for which we present the results in the coming sections. Here we have $\epsilon > \epsilon_{\mathrm{IV}}$ and the Fermi level crosses two Fermi rings with opposite spin textures;

The expressions for the different limits are given in Table 3.2. The high energy regime can be tuned into in gated devices [11, 190].

Spin and Pseudospin Textures

Understanding how the spin polarisation depends on the momentum and how it changes with the Hamiltonian parameters is key to identify what the mechanisms are behind the spin density semi-classical response. For high-electronic densities (regime II), the spin operators have the following equilibrium average values, in the asymptotic limit $\epsilon \gg \mathfrak{m}_z \equiv \tilde{\mathfrak{m}}_z \gg \mathfrak{m}_x$ (with θ the wave-vector angle with respect to the $\hat{x}$ axis):

$$\langle s_x \rangle = \frac{\alpha}{\sqrt{\alpha^2 + \mathfrak{m}_z^2}} \left(1 - \frac{(\Delta \mathfrak{m}_z + \alpha^2)^2}{2\epsilon^2 (\alpha^2 + \mathfrak{m}_z^2)} \right) \sin\theta + \mathfrak{m}_x \frac{\mathfrak{m}_z^2 + \alpha^2 \cos^2\theta}{(\alpha^2 + \mathfrak{m}_z^2)^{3/2}}, \quad (3.27a)$$

$$\langle s_y \rangle = -\frac{\alpha}{\sqrt{\alpha^2 + \mathfrak{m}_z^2}} \left(1 - \frac{(\Delta \mathfrak{m}_z + \alpha^2)^2}{2\epsilon^2 (\alpha^2 + \mathfrak{m}_z^2)} \right) \cos\theta + \frac{\mathfrak{m}_x}{2} \frac{\alpha^2 \sin 2\theta}{(\alpha^2 + \mathfrak{m}_z^2)^{3/2}}, \quad (3.27b)$$

$$\langle s_z \rangle = \frac{\mathfrak{m}_z}{\sqrt{\alpha^2 + \mathfrak{m}_z^2}} \left(1 + \frac{\alpha^2}{2\epsilon^2} \frac{\Delta^2 - \mathfrak{m}_z^2}{\alpha^2 + \mathfrak{m}_z^2} - \frac{\mathfrak{m}_x \alpha}{\alpha^2 + \mathfrak{m}_z^2} \sin\theta \right) + \frac{\alpha^4}{\epsilon^2} \frac{\Delta - \mathfrak{m}_z}{(\alpha^2 + \mathfrak{m}_z^2)^{3/2}}, \quad (3.27c)$$

for the spin majority band, the other band has opposite polarity. In Fig. 3.3b it is shown the spin texture for the spin majority band at a fixed Fermi energy. The pseudospin texture, on the other hand, is:

$$\langle \sigma_x \rangle = \left(1 - \frac{\alpha^2 + \Delta^2}{2\epsilon^2} \right) \cos\theta \pm \frac{\alpha \mathfrak{m}_x}{2\epsilon} \frac{\sin 2\theta}{\sqrt{\alpha^2 + \mathfrak{m}_z^2}}, \quad (3.28a)$$

$$\langle\sigma_y\rangle = \left(1 - \frac{\alpha^2 + \Delta^2}{2\epsilon^2}\right)\sin\theta \mp \frac{\alpha\mathfrak{m}_x}{2\epsilon}\frac{1 + \cos 2\theta}{\sqrt{\alpha^2 + \mathfrak{m}_z^2}}, \tag{3.28b}$$

$$\langle\sigma_z\rangle = \frac{\Delta}{\epsilon} \mp \frac{\mathfrak{m}_z}{\sqrt{\alpha^2 + \mathfrak{m}_z^2}}\frac{\Delta\mathfrak{m}_z + \alpha^2}{\epsilon^2}\left(1 - \frac{\alpha\mathfrak{m}_x}{\alpha^2 + \mathfrak{m}_z^2}\sin\theta\right), \tag{3.28c}$$

where the $\pm$ refers to the spin majority and minority bands, respectively. Figure 3.4 shows the spin and pseudospin profiles along the $\hat{x}$ and $\hat{y}$ directions in momentum space. The orbital mass (Δ) broadens up the $\mathbf{p}$-space spin texture dramatically, which boosts the generation of out-of-plane spin polarisation in applied current. Near $\mathbf{p} = 0$ we see that both the spin and pseudospin textures display non-trivial features such as fast oscillations and change of sign. These can be traced back to the "Mexican hat" shape of the energy bands. Near zero momentum, the velocity changes its sign several times and so does the pseudospin (the velocity operator of the model is the pseudospin). With $\Delta, \lambda_{sv} \neq 0$ the "Mexican hat" is no longer present and the pseudospin texture is smoothed. Due to spin momentum-locking the spin texture follows a similar progression.

Self-Energy

The presence of all the couplings in the Hamiltonian (3.22) generates new matrix structures in the self-energy, even with scalar disorder. The T-Matrix now has the following structure:

$$\begin{aligned}\Sigma^R = &t_{00}\gamma_{00} + t_{01}\gamma_{01} + t_{03}\gamma_{03} + t_{12}\gamma_{12} + t_{20}\gamma_{20} + t_{21}\gamma_{21} + \\ &+ t_{23}\gamma_{23} + t_{30}\gamma_{30} + t_{31}\gamma_{31} + t_{33}\gamma_{33}\end{aligned} \tag{3.29}$$

In the Gaussian approximation it gets significantly simpler:

$$\Sigma^R_G = -i\eta\left(\mathbf{1} + \frac{\Delta}{\epsilon}\tau_z\sigma_z + \frac{\mathfrak{m}_x}{\epsilon}s_x + \frac{\mathfrak{m}_z}{\epsilon}s_z\right), \tag{3.30}$$

where $\eta = nu_0^2\epsilon/(4v^2)$ is the disorder-induced quasiparticle broadening. The magnetised Dirac-Rashba model thus has the extra feature that, already at Gaussian level with scalar impurities, the self-energy is not scalar even in the high energy regime. However, since it does not generate any new matrix structures we can obtain the disorder average GF from the clean GF via the substitution similar to the one from Eq.(3.18) but now for $\mathfrak{m}_z$ and $\mathfrak{m}_x$. The expression for the GF of the clean systems is presented in Appendix A for the case where m_x is small. Due to its complexity the full T-Matrix case will be
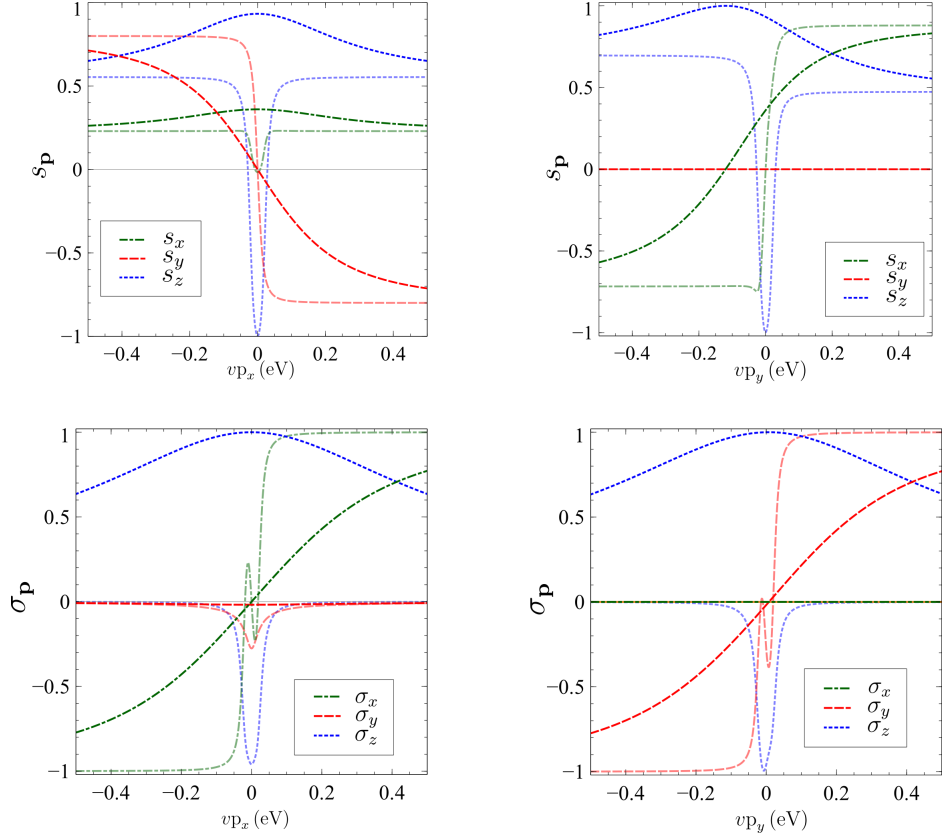
Figure 3.4: Spin (top row) and pseudospin (bottom row) profiles along $\hat{x}$ (left column) and $\hat{y}$ (right column). The semi transparent curves refer to the massless case ($\Delta = 0$). This mass term greatly broadens the profiles, particularly of s_z which is highly peaked near zero energy in the massless case. Parameters used $\alpha = 20$ meV, $\Delta_{xc} = 15$ meV, $\theta_{\mathbf{m}} = \pi/8$, $\Delta = 400$ meV, $\lambda_{sv} = 0$.

treated numerically in Chapter 5.

We end this section highlighting a difference between this generalised model and the Dirac-Rashba introduced in Section 3.2. In the standard Dirac-Rashba model skewness is absent. Scalar impurities yielding the potential from Eq.(3.2) do not distinguish between the left and right scattering directions. This can be explicitly confirmed by computing the transition amplitude[1]:

$$W_{\mathbf{p}\mathbf{p}'} = W(\varphi) = 2\pi n \left| \langle \mathbf{p}' | T^R | \mathbf{p} \rangle \right|^2 \delta \left(\epsilon_{\mathbf{p}} - \epsilon'_{\mathbf{p}} \right), \qquad (3.31)$$

which can be shown to be even in $\varphi = \theta - \theta'$, the difference between the initial and final momentum angles [191]. In the generalised version, however, the presence of m_z is enough to distinguish left and right scattering

---

[1]For simplicity we have presented an expression valid in regime I where the Fermi level crosses only one band. In regime II one would have to include inter-band transitions, however the final conclusion is unchanged.

processes, akin to an external magnetic field. This asymmetry is carried through onto the scattering cross section $W_{\mathbf{pp'}}$ and is the source of skews-cattering upon impurity scattering. This will be key when analysing the SOT response of the system and is one of the reasons why we employ the T-Matrix formalism.

Chapter 4

Weak Localisation Corrections

4.1 Quantum Corrections to the Conductivity in Graphene

In this Chapter we will put into practice the formalism we have presented in previous sections to compute the quantum corrections to conductivity. We will start by applying it to simple systems with the aim of familiarising ourselves with the type of arguments and features that are characteristic of this approach. We start with graphene with simple scalar impurities and then recovering the famous results of Ando and Suzuura for graphene with intervalley scatterers [142]. This will serve as the foundation for our goal of studying the case of strong SOC in the band structure.

4.1.1 Vertex Corrections and Conductivity

For pedagogical reasons we briefly review the semi-classical (dominant) contribution for the longitudinal conductivity in this system. This can be easily computed using Eq.(2.22):

$$\sigma^c = \frac{e^2}{2\pi} \int \frac{d\mathbf{p}}{4\pi^2} \mathrm{Tr} \left\{ v_x \mathcal{G}^R_\mathbf{p} \tilde{v}_x \mathcal{G}^A_\mathbf{p} \right\}, \tag{4.1}$$

where $v_i = \partial_{\mathbf{p}_i} \mathcal{H}_0 = v\sigma_i$ is the (bare) velocity operator and the tilde denotes vertex renormalisation due to disorder. For scalar disorder, these vertex corrections can be computed using:

$$\tilde{v}_i = v_i + nu_0^2 \int \frac{d\mathbf{p}}{4\pi^2} \text{Tr} \left\{ \mathcal{G}_{\mathbf{p}}^R \tilde{v}_i \mathcal{G}_{\mathbf{p}}^A \right\}, \tag{4.2}$$

which is a specific case of Eq.(2.23). In this simple case the structure of the renormalised vertex is the same as the bare one and we get the notorious result for electrons in graphene:

$$\tilde{v}_x = 2\hat{v}_x. \tag{4.3}$$

Inserting this result in Eq.(4.1) yields, to leading order in the impurity concentration:

$$\begin{aligned}
\sigma^c &= \frac{e^2 v^2}{\pi} \left(\frac{|\epsilon|}{2v^2\eta} \right) \\
&= \frac{e^2}{\pi} \epsilon \tau_{tr},
\end{aligned} \tag{4.4}$$

already accounting for spin and valley degeneracy factors. We have defined the *transport time* $\tau_{tr} \equiv 2\tau_\mathrm{p}$, which is the average time between collisions that significantly alter the electrons trajectory so that they are no longer contributing to the longitudinal transport. The fact that, in graphene, this time is twice the average time between any collisions is the manifestation of the *suppression of backscattering* in pristine graphene. This suppression can be traced back to graphene's Berry phase of π [9, 192].

4.1.2   The Cooperon Structure

The Cooperon is a two particle object encoding the series of maximally crossed diagrams that control the weak (anti)localisation effects. This series of diagrams can be fully summed using:

$$\mathcal{C}(\boldsymbol{Q}) = \frac{nu_0^2}{1 - nu_0^2 P(\boldsymbol{Q})}, \tag{4.5}$$

where $P(\boldsymbol{Q})$ is the recursion insertion given by:

$$P(\boldsymbol{Q}) = \sum_{\mathbf{p}''} \mathcal{G}_{\mathbf{p}''}^R \otimes \mathcal{G}_{\boldsymbol{Q}-\mathbf{p}''}^A \approx P^{(0)} + QP^{(1)} + Q^2 P^{(2)}, \tag{4.6}$$

in the small momentum Q limit ($Q \ll \mathrm{p}_F$) as discussed in Section 2.3.4.

It is important to choose a suitable basis to perform the calculations, not only to make them simpler, but to also provide insight into the nature of

the interference corrections. The following transformation T_θ which makes $P(\boldsymbol{Q})$ block diagonal:

$$\begin{pmatrix} |\chi_1\rangle \\ |\chi_2\rangle \\ |\chi_3\rangle \\ |\chi_4\rangle \end{pmatrix} = \frac{1}{\sqrt{2}} \begin{pmatrix} e^{i\theta_Q} & 0 & 0 & -e^{i\theta_Q} \\ 0 & 1 & -1 & 0 \\ 0 & 1 & 1 & 0 \\ e^{i\theta_Q} & 0 & 0 & e^{i\theta_Q} \end{pmatrix} \begin{pmatrix} |\uparrow\uparrow\rangle \\ |\uparrow\downarrow\rangle \\ |\downarrow\uparrow\rangle \\ |\downarrow\downarrow\rangle \end{pmatrix}, \tag{4.7}$$

with θ_Q the Cooperon momentum angle [193]. We shall call this the "block basis" and will denote matrices written in this basis by a tilde. The states $|\chi_1\rangle$, $|\chi_3\rangle$ and $|\chi_4\rangle$ are pseudospin (sublattice degree of freedom) triplets and $|\chi_2\rangle$ is the pseudospin singlet. This block basis is useful to perform the matrix inversion needed to get the Cooperon. This transformation is formed by the eigenvectors of the matrix $\sigma_{\theta_Q} \otimes \sigma_{\theta_Q}$, where $\sigma_{\theta_Q} = -i\left(\sigma_x \cos\theta_Q + \sigma_y \sin\theta_Q\right)$ rotates the momemtum in the Hamiltonian as $\theta \to 2\theta_Q - \theta$. The usual singlet triplet basis can be obtained via the following transformation matrix J_M:

$$\begin{pmatrix} |t_1\rangle \\ |s\rangle \\ |t_2\rangle \\ |t_4\rangle \end{pmatrix} = \begin{pmatrix} 1 & 0 & 0 & 0 \\ 0 & \frac{1}{\sqrt{2}} & -\frac{1}{\sqrt{2}} & 0 \\ 0 & \frac{1}{\sqrt{2}} & \frac{1}{\sqrt{2}} & 0 \\ 0 & 0 & 0 & 1 \end{pmatrix} \begin{pmatrix} |\uparrow\uparrow\rangle \\ |\uparrow\downarrow\rangle \\ |\downarrow\uparrow\rangle \\ |\downarrow\downarrow\rangle \end{pmatrix}. \tag{4.8}$$

In the block basis we get the following result for P, at leading order in η/ϵ (the tilde denotes matrices in the block basis):

$$\tilde{P}^{(0)} = \frac{1}{8v^2} \frac{|\epsilon|}{\eta} \begin{pmatrix} 1 & 0 & 0 & 0 \\ 0 & 2 & 0 & 0 \\ 0 & 0 & 0 & 0 \\ 0 & 0 & 0 & 1 \end{pmatrix}, \tag{4.9a}$$

$$\tilde{P}^{(1)} = i\frac{|\epsilon|}{16v\eta^2} \begin{pmatrix} 0 & 1 & 0 & 0 \\ 1 & 0 & 0 & 0 \\ 0 & 0 & 0 & 0 \\ 0 & 0 & 0 & 0 \end{pmatrix} \tag{4.9b}$$

$$\tilde{P}^{(2)} = -\frac{|\epsilon|}{128\eta^3} \begin{pmatrix} 3 & 0 & 0 & 0 \\ 0 & 4 & 0 & 0 \\ 0 & 0 & 0 & 0 \\ 0 & 0 & 0 & 1 \end{pmatrix} \tag{4.9c}$$

We thus get the following result for $\tilde{P}$:

$$nu_0^2 \tilde{P}(\boldsymbol{Q}) = \begin{pmatrix} \frac{1}{2} - \frac{3\ell^2 Q^2}{8} & i\frac{\ell Q}{2} & 0 & 0 \\ i\frac{\ell Q}{2} & 1 - \frac{\ell^2 Q^2}{2} & 0 & 0 \\ 0 & 0 & 0 & 0 \\ 0 & 0 & 0 & \frac{1}{2} - \frac{\ell^2 Q^2}{8} \end{pmatrix}. \tag{4.10}$$

Here we have introduced the mean free path $\ell = v\tau_{\rm p} = v/2\eta$ and have used Eqs.(3.4) and (3.5) to write $nu_0^2 = 4v^2\eta/\epsilon$. In this block basis none of the terms depend on the angle of the Cooperon momentum θ_Q. Eq.(4.10) already hints about the nature of the quantum corrections to the conductivity. Firstly the triplet $|\chi_3\rangle$ (the one with 0 angular momentum projection) does not contribute as it is a completely flat mode. Furthermore, the singlet and triplet $|\chi_1\rangle$ are coupled to each other linearly in $\boldsymbol{Q}$. This coupling is fundamental to capture the correct transport time of the system, as we shall show shortly.

The Cooperon matrix then takes the following form:

$$\frac{1}{nu_0^2}\tilde{\mathcal{C}}(\boldsymbol{Q}) = \begin{pmatrix} X_{11} & X_{12} & 0 & 0 \\ X_{21} & X_{22} & 0 & 0 \\ 0 & 0 & X_{33} & 0 \\ 0 & 0 & 0 & X_{44} \end{pmatrix}, \tag{4.11}$$

where the X coefficients can be written as:

$$X_{11} = \frac{c_{11}}{\lambda_1^{-2} + Q^2}, \quad X_{22} = \frac{c_{21}}{\lambda_1^{-2} + Q^2} + \frac{c_{22}}{\lambda_2^{-2} + Q^2}, \tag{4.12a}$$

$$X_{33} = 1, \quad X_{44} = \frac{c_{44}}{\lambda_4^{-2} + Q^2}, \tag{4.12b}$$

with $c_{11} = 8\ell^{-2}/3$ and $c_{21} = c_{22} = \ell^{-2}$. The quantities λ_i are relaxation lengths that describe the average length a particle hole pair from each channel can travel while preserving their sublattice coherence. They are given by:

$$\lambda_1 = \sqrt{\frac{3}{8}}\ell, \quad \lambda_2 = \infty, \quad \lambda_4 = \frac{\ell}{2}. \tag{4.13}$$

We emphasise that these relaxation lengths are different from other microscopic relaxation lengths such as the mean free path. These control instead the typical length scale of pseudospin two particle coherence. Let us focus
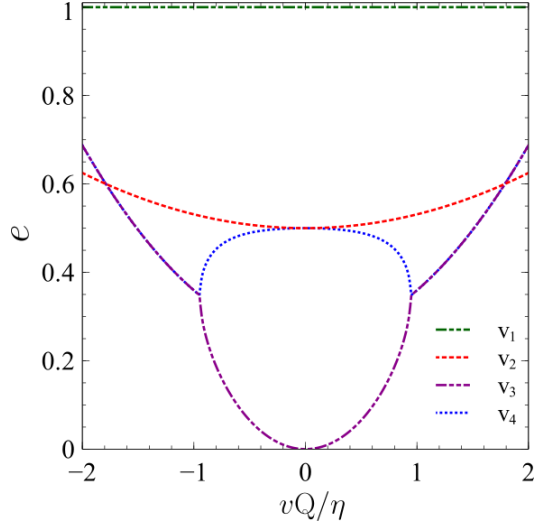
Figure 4.1: The dispersions of the Cooperon modes for graphene with scalar impurites. The only gapless mode is the pseudospin singlet, making it the dominant contribution for large coherence length $L \gg \ell$. The point at which e_3 and e_4 join marks the momentum at which the modes are no longer real.

our attention on the singlet mode. For small momentum we have:

$$X_{22} \sim \frac{1}{D\tau_{\mathrm{p}}Q^2},$$ (4.14)

which has the familiar form of a diffusion pole with a diffusion coefficient given by $D = v^2 \tau_{tr}/2$, where the transport time is twice the momentum relaxation time $\tau_{tr} = 2\tau_{\mathrm{p}}$. So the coupling between the singlet and the triplet, which is the anti-hermitian part of the Cooperon Hamiltonian, encodes information about the suppression of the backscattering in graphene and is fundamental to capture the correct diffusion behaviour. Furthermore, it is also responsible for endowing the dispersion of the modes with a imaginary part [193]. The presence of the diffusion pole links the singlet state with charge conservation. In fact, we will see that this holds true for all our systems.

The relaxation lengths are effectively gaps in the dispersion relations of each mode, with the singlet being the only gapless. The WL corrections are controlled by the low momentum contributions, therefore the modes that contribute the most are the ones with the lowest gaps. An alternative and more straightforward method for obtaining these gaps is by computing the eigenvalues of the Cooperon Hamiltonian $\mathcal{H}_C = 1 - nu_0^2 P$ at $\mathbf{Q} = 0$. The real part of the full dispersions are shown in Fig. 4.1. Again we see the single gapless mode, that should be the one dominating the physics. We can

analyse the eigenstates to identify the different modes. For small η and Q these are:

$$v_1 = \begin{pmatrix} 0 \\ 1 \\ 1 \\ 0 \end{pmatrix}, \qquad v_2 = \begin{pmatrix} e^{-i\theta_Q} \\ 0 \\ 0 \\ e^{i\theta_Q} \end{pmatrix}, \qquad \text{(4.15a)}$$

$$v_3 = \begin{pmatrix} -e^{-i\theta_Q} \\ i\frac{2\eta}{vQ} \\ -i\frac{2\eta}{vQ} \\ e^{i\theta_Q} \end{pmatrix}, \quad v_4 = \begin{pmatrix} -e^{-i\theta_Q} \\ i\frac{vQ}{2\eta} \\ -i\frac{vQ}{2\eta} \\ e^{i\theta_Q} \end{pmatrix}, \qquad \text{(4.15b)}$$

with the respective dispersion relations:

$$e_1 = 1, \qquad e_2 = \frac{1}{2} + \frac{Q^2 v^2}{32\eta^2}, \qquad \text{(4.16a)}$$

$$e_3 = \frac{Q^2 v^2}{4\eta^2}, \quad e_4 = \frac{1}{2} - \frac{Q^2 v^2}{32\eta^2}. \qquad \text{(4.16b)}$$

The first state is precisely the triplet $|t_2\rangle$. We see that both v_3 and v_4 have contributions from the singlet state $(0, 1, -1, 0)^T$. This reflects the fact that triplet 1 and the singlet are coupled in $P(\boldsymbol{Q})$, however, only v_3 is gapless. As $Q \to 0$ this state becomes essentially the singlet. After inverting the Cooperon Hamiltonian and performing the angular integration (recovering translational symmetry) we will see that the singlet is a true mode of the Cooperon and the only one that is gapless.

4.1.3 The Weight Matrix

As defined before, the weight tensor is given by:

$$W_{\nu'\nu}^{\mu'\mu} = \sum_{\mathbf{p}} \left(\mathcal{G}_{\mathbf{p}}^A \tilde{v}_x \mathcal{G}_{\mathbf{p}}^R \right)_{\nu'\mu} \left(\mathcal{G}_{-\mathbf{p}}^R \tilde{v}_x \mathcal{G}_{-\mathbf{p}}^A \right)_{\mu'\nu}, \qquad \text{(4.17)}$$

with $\tilde{v}_x = 2v\sigma_x$ being the renormalised velocity operator. We obtain the following structure, in the tensor product basis:

$$W = \frac{|\epsilon|}{8\eta^3} \begin{pmatrix} -1 & 0 & 0 & \frac{1}{2} \\ 0 & 1 & -1 & 0 \\ 0 & -1 & 1 & 0 \\ \frac{1}{2} & 0 & 0 & -1 \end{pmatrix}. \qquad \text{(4.18)}$$

Looking at its structure we can already guess that W will not be diagonal in the J_M basis since it has terms mixing the states $|\uparrow\uparrow\rangle$ and $|\downarrow\downarrow\rangle$. These states are not mixed in the J_M basis. Indeed the basis that diagonalises W is given by the following transformation, $J_M^\star$:

$$\begin{pmatrix} |t_1^\star\rangle \\ |s^\star\rangle \\ |t_2^\star\rangle \\ |t_4^\star\rangle \end{pmatrix} = \frac{1}{\sqrt{2}} \begin{pmatrix} 1 & 0 & 0 & 1 \\ 0 & 1 & -1 & 0 \\ 0 & 1 & 1 & 0 \\ 1 & 0 & 0 & -1 \end{pmatrix} \begin{pmatrix} |\uparrow\uparrow\rangle \\ |\uparrow\downarrow\rangle \\ |\downarrow\uparrow\rangle \\ |\downarrow\downarrow\rangle \end{pmatrix}, \tag{4.19}$$

such that:

$$W^\star = J_M^\star . W . (J_M^\star)^{-1} = \frac{|\epsilon|}{16\eta^3} \begin{pmatrix} -1 & 0 & 0 & 0 \\ 0 & 4 & 0 & 0 \\ 0 & 0 & 0 & 0 \\ 0 & 0 & 0 & -3 \end{pmatrix} \tag{4.20}$$

where the star denotes matrices written in the $J_M^\star$ basis. In this way we can see that the true modes of the problem are not eigenstates of the z projection of the total pseudospin. Furthermore, it is at this level that we see the singlet contributing with an opposite sign to the other two triplets, already highlighting the importance of the matrix structure of W.

4.1.4 Correction to the Conductivity

The weight matrix can be written as:

$$W = \begin{pmatrix} W_{11} & 0 & 0 & -W_{11}/2 \\ 0 & -W_{11} & W_{11} & 0 \\ 0 & W_{11} & -W_{11} & 0 \\ -W_{11}/2 & 0 & 0 & W_{11} \end{pmatrix}, \tag{4.21}$$

with $W_{11} = -\frac{|\epsilon|}{8\eta^3}$. Since the singlet triplet basis depends on the direction of $\boldsymbol{Q}$ we go back to the tensor product basis and integrate the Cooperon over θ_Q:

$$\int \frac{\mathrm{d}^2 Q}{(2\pi)^2} \mathcal{C}(\boldsymbol{Q}) = \int \frac{\mathrm{d}Q}{2\pi} Q \frac{4v^2\eta}{|\epsilon|} \begin{pmatrix} \frac{X_{11}+X_{44}}{2} & 0 & 0 & 0 \\ 0 & \frac{X_{22}+X_{33}}{2} & \frac{X_{22}-X_{33}}{2} & 0 \\ 0 & \frac{X_{22}-X_{33}}{2} & \frac{X_{22}+X_{33}}{2} & 0 \\ 0 & 0 & 0 & \frac{X_{11}+X_{44}}{2} \end{pmatrix}, \tag{4.22}$$

with X_{ii} given by Eqs.(4.12a) and (4.12b). The correction to the conductivity becomes:

$$
\begin{aligned}
\Delta\sigma &= \frac{e^2}{2\pi} \frac{4v^2\eta}{|\epsilon|} \int \frac{\mathrm{d}Q}{2\pi} Q\, W_{11} \left[X_{11} - 2X_{22} + X_{44} \right] \\
&= \frac{e^2 D\tau}{\pi} \int \frac{\mathrm{d}Q}{2\pi} Q\, \left[2X_{22} - X_{11} - X_{44} \right],
\end{aligned}
\tag{4.23}
$$

with $D = v^2 \tau_{tr}/2$. In this way we can see that triplets 1 and 4 contribute with the same weight to the conductivity while the singlet has the opposite sign and has double their weight. Since $W_{11} < 0$ the singlet contribution is positive, being anti-localising in nature, while the triplets contribute towards weak localisation. Going back to Eq.(4.22) we can see that, after angular integration, the Cooperon has two degenerate eigenvalues corresponding to the states $|\uparrow\uparrow\rangle$ and $|\downarrow\downarrow\rangle$. For this reason, the Cooperon is diagonal in both basis J_M and $J_M^\star$ since $|t_1^\star\rangle$ and $|t_4^\star\rangle$ are linear combinations of degenerate eigenstates. Note that this is only true after the angular integration. In any of these two basis we get:

$$
\int \frac{\mathrm{d}^2Q}{(2\pi)^2} \mathcal{C}^\star\left(\boldsymbol{Q}\right) = \int \frac{\mathrm{d}Q}{2\pi} Q\, \frac{4v^2\eta}{|\epsilon|}
\begin{pmatrix}
\frac{X_{11}+X_{44}}{2} & 0 & 0 & 0 \\
0 & X_{22} & 0 & 0 \\
0 & 0 & X_{33} & 0 \\
0 & 0 & 0 & \frac{X_{11}+X_{44}}{2}
\end{pmatrix}.
\tag{4.24}
$$

This form together with Eq.(4.20) paints a complete picture of the problem. The $W^\star$ matrix tells us which modes are (anti) localising simply by the sign of its diagonal entries.

Finally we get for the correction to the conductivity:

$$
\begin{aligned}
\Delta\sigma &= \frac{e^2 v^2}{4\pi\eta^2} \int_{\frac{1}{L}}^{\frac{1}{\ell}} \frac{\mathrm{d}Q}{2\pi} \left[\frac{2}{\ell^2 Q} - \frac{1}{4} \frac{Q}{1 + \frac{3}{8}\ell^2 Q^2} - 2\frac{Q}{1 + \frac{1}{4}\ell^2 Q^2} \right] \\
&= \frac{e^2}{2\pi^2} \left[2\ln\left(\frac{L}{\ell}\right) - \frac{1}{3}\ln\left(\frac{11}{8 + 3\left(\frac{\ell}{L}\right)^2}\right) - 4\ln\left(\frac{5}{4 + \left(\frac{\ell}{L}\right)^2}\right) \right].
\end{aligned}
\tag{4.25}
$$

It can be seen that this function is always positive for $L > \ell$: it is an anti-localisation correction. For $L \gg \ell$, the dominant term will be the $\ln\left(L/\ell\right)$ coming from the singlet. Accounting for spin and valley degeneracy we obtain:

$$
\Delta\sigma = 4\frac{e^2}{\pi^2} \ln\left(\frac{L}{\ell}\right),
\tag{4.26}
$$

which is the celebrated result obtained by Ando and Suzuura [142]. The weak anti-localisation nature of bare graphene is yet another manifestation of the absence of backscattering in this system due graphene's Berry phase of π [9, 192]. In the next section we will show the case where a more realistic disorder is able to activate backscattering, altering the nature of the quantum coherence effects.

4.2 Bare Graphene with Complex Impurities

So far we have restricted ourselves to the simplest of impurity potentials. Scalar impurities do not connect different valleys and neither do they allow for backscattering as we can see if we take the overlap between two eigenstates of the system in the same band:

$$|\langle \psi_\theta | U | \psi_{\theta'} \rangle|^2 = \frac{1 + \cos(\theta - \theta')}{2} u_0^2, \qquad (4.27)$$

so for backscattering we have $\theta - \theta' = \pi$ and the probability is completely suppressed. In this way, backscattering in simple graphene is forbidden and the conductivity correction can never be negative. In the light of this argument the result previously obtained is not too surprising.

4.2.1 Impurities with σ_z: Single valley calculation

We can open the backscattering channel by considering different types of impurity potentials. A simple mismatch between the local energies in the A and B sublattices is sufficient. This is achieved via:

$$U = u_0 \sigma_0 + u_z \sigma_z. \qquad (4.28)$$

Now we have

$$2 |\langle \psi_\theta | U | \psi_{\theta'} \rangle|^2 = u_0^2 + u_z^2 + \left(u_0^2 - u_z^2 \right) \cos(\theta - \theta') \qquad (4.29)$$

and the backscattering probability is u_z^2. So we expect that, beyond a certain value of u_z the quantum correction will change its sign and weak localisation will be established. We can perform a similar calculation to the one we have done previously with a few tweaks. In the presence of a general impurity potential the Cooperon is given by:

$$C\left(\boldsymbol{Q}\right) = \frac{\xi}{1 - \xi P\left(\boldsymbol{Q}\right)}, \tag{4.30}$$

with $\xi = nU \otimes U$. Again we assume Gaussian impurities and we take different types of disorder to be uncorrelated: $\langle u_i\left(\mathbf{r}\right) u_j\left(\mathbf{r}'\right)\rangle_{dis} = nu_i^2\delta_{ij}\delta\left(\mathbf{r} - \mathbf{r}'\right)$, with $i, j = 0, z$. This leads to $\xi = n\left(u_0^2 + u_z^2\sigma_z \otimes \sigma_z\right)$. With uncorrelated disorder the self energy remains scalar so that $\mathcal{G}_{\mathbf{p}}^{R,A} = \left[\epsilon - \mathcal{H}_{0\mathbf{p}} \pm i\eta\right]^{-1}$ with:

$$\eta = \frac{\epsilon}{4v^2}n\left(u_0^2 + u_z^2\right). \tag{4.31}$$

We can get useful information by looking at the modes of the Cooperon Hamiltonian. Remarkably, for this case, there is no gapless mode. The sublattice disorder gaps the sublattice singlet:

$$e_1 = 1, \qquad e_2 = \frac{1}{2} + \frac{v^2Q^2}{32\eta^2}, \tag{4.32a}$$

$$e_3 = 2\frac{u_z^2}{u_0^2 + u_z^2} + \frac{v^2Q^2}{4\eta^2}\frac{\left(u_0^2 - u_z^2\right)^2}{\left(u_0^2 - 3u_z^2\right)\left(u_0^2 + u_z^2\right)}, \tag{4.32b}$$

$$e_4 = \frac{1}{2} - \frac{v^2Q^2}{32\eta^2}\frac{u_0^2 + 5u_z^2}{u_0^2 - 3u_z^2}. \tag{4.32c}$$

The eigenstates are now:

$$v_1 = \left(0, 1, 1, 0\right), \qquad v_2 = \left(e^{-i\theta_Q}, 0, 0, e^{i\theta_Q}\right), \tag{4.33a}$$

$$v_3 = \left(-\frac{u_0^2 + u_z^2}{u_0^2 - 3u_z^2}e^{-i\theta_Q}, i\frac{2\eta}{vQ}, -i\frac{2\eta}{vQ}, \frac{u_0^2 + u_z^2}{u_0^2 - 3u_z^2}e^{i\theta_Q}\right), \tag{4.33b}$$

$$v_4 = \left(-\frac{u_0^2 - 3u_z^2}{u_0^2 - u_z^2}e^{-i\theta_Q}, i\frac{vQ}{2\eta}, -i\frac{vQ}{2\eta}, \frac{u_0^2 - 3u_z^2}{u_0^2 - u_z^2}e^{i\theta_Q}\right), \tag{4.33c}$$

assuming $u_0^2 > 3u_z^2$. The full dispersions are shown in Fig. 4.2a. The lack of a gapless mode is due to the fact that the disorder we have used actually breaks time-reversal invariance. When looking at the physics of a single valley the time reversal operator is $\sigma_y\mathcal{K}$ which does not commute with σ_z. This breaks the equivalence between the Cooperon and the Diffuson [157], so we lose the gapless state (diffusion pole). As we increase u_z the singlet stops dominating the quantum corrections. Since it is the singlet the only one that entails a positive correction, after that point the correction must become negative. We can see this happening in Fig. 4.2b. Looking at the separate channels, we find that the singlet actually changes the sign of its contribution at $u_0 = u_z$ due to a prefactor $u_0^2 - u_z^2$ in its term. The $t_1^\star$ and $t_2^\star$

channels are relatively unaffected by u_z.
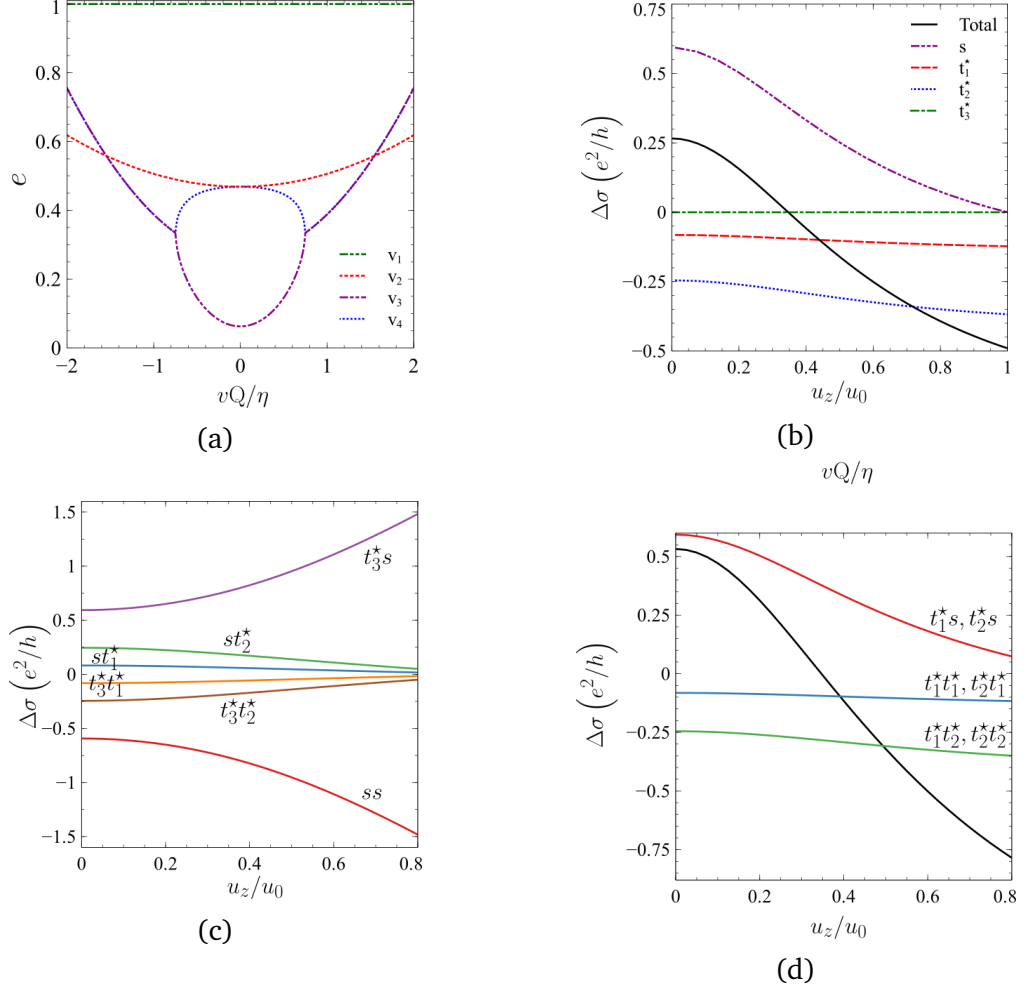
Figure 4.2: (a) The dispersion of the Cooperon modes for graphene with σ_z impurities, in one valley, for $u_0 = 4u_z$. The most striking feature is the absence of a gapless mode, as the presence of u_z gaps the singlet mode. (b) Quantum correction for the conductivity (per valley, per spin) in graphene with sublattice disorder σ_z, for $\epsilon = 0.2$ eV, $\ell = 0.2$ μm, $L = 1$ μm and $n = 10^{14}$ cm^{-2}. The coloured lines show the individual contributions towards $\Delta\sigma$ from each mode channel in the $J_M^\star$ basis. Since the singlet gap increases linearly with u_z, for $u_z \ll u_0$ we have the WAL phase dictated by this channel. As u_z increases, so does the singlet gap and the $t_1^\star$ and $t_2^\star$ channels become more relevant, as they remain largely unaltered, eventually driving the system towards a WL phase, which can be seen in the total correction to the conductivity (black line). Taking into account the two valleys splits the modes into four, two with the wrong symmetries that cancel each other (c) and two others with the right symmetries that yield the degeneracy factor of 2 to $\Delta\sigma$ (d).

4.2.2 Impurities with σ_z: Two valley calculation

To recover time reversal symmetry we need to include the second valley. We perform exactly the same calculation but now including explicitly the isospin (valley degree of freedom), which we act on using the Pauli matrices τ_i, $i = 0, x, y, z$. At this stage there are a few points to note. In the normal $\{A, B, A, B\}$ basis the angular momentum (without the orbital part) is given by $\tau_z \sigma_z$ which makes it difficult to define a basis where valley and sublattice are decoupled. So we use the "magic basis 2" $\{A, B, -B, A\}$, from Table 3.1. In this basis the angular momentum is simply σ_z. Furthermore, the Hamiltonian is separated into two exact copies for each valley. For these reasons, this is the basis that will yield the results that are the most straightforward to analyse. From now on we define triplets and singlets relative to whichever basis we are working on, which means that the singlet is $|\uparrow\downarrow\rangle - |\downarrow\uparrow\rangle$, where the $\uparrow$ state is whatever state is the first in the basis for the SU(2) space we are referring to. Lastly we will use the short-hand notation of ab to denote a product state $|a\rangle \otimes |b\rangle$ and similarly for $abc \equiv |a\rangle \otimes |b\rangle \otimes |c\rangle$

With these preliminaries done we can focus on the quantum corrections. The Hamiltonian in this basis is given by:

$$\mathcal{H}_{0\mathbf{p}} = v\tau_0\boldsymbol{\sigma} \cdot \mathbf{p}, \tag{4.34}$$

and the impurity potential is

$$U = u_0\tau_0\sigma_0 + u_z\tau_z\sigma_z. \tag{4.35}$$

notice the appearance of τ_z. This is simply to ensure the system is invariant under time reversal, which in this basis is given by the operator $\tau_y\sigma_y\mathcal{K}$. [1]

Performing the calculation in the same way as before we first find that the modes of the Cooperon Hamiltonian come in degenerate pairs. This pairing is always between different types of intra and inter-valley states. For example, the two gapless states, the ss state and the t_3s state, are paired, as are t_2t_3 and t_1t_3, and so on. The gaps for the pseudospin singlet states are:

$$\Delta_{ss} = 0 = \Delta_{t_3s}, \qquad \Delta_{t_2s} = \Delta_{t_1s} = 2\frac{u_z^2}{u_0^2 + u_z^2} \tag{4.36}$$

This pairing is also visible when we look at the different channels for the quantum corrections, Figs. 4.2d and 4.2c. The intervalley channels cancel

---

[1] It is in this basis that is most evident that isospin and pseudospin work as effective spins of the theory since, under time reversal, they transform exactly as a normal spin.

each other in pairs while the intravalley modes from one valley contribute exactly as the ones from the other valley yielding a simple factor of two with respect to the calculation done accounting for just one valley. Interestingly, since in this case the two gapless states ss and t_3s cancel each other, the quantum corrections are actually controlled by the higher energy modes t_1s and t_2s.

4.2.3 Intervalley Scattering Impurities

Now we do the same exercise but with impurities that connect the two valleys. Intervalley scattering can be activated via very localised potentials that induce large momentum scatterings, capable of changing the electronic isospin [148]. Connecting the two valleys also allows for backscattering in graphene so we again expect the nature of quantum corrections to change, as with the sublattice imbalance impurities from the previous sections. In the magic basis 2 such an effect is achieved via[2]:

$$U = u_0 \tau_0 \sigma_0 - u_x \tau_x \sigma_z, \tag{4.37}$$

this specific intervalley term can be generated by a hollow adatom [194]. Again, the presence of σ_z ensures the system remains time reversal invariant. Now the pseudospin singlets have the following gaps:

$$\Delta_{ss} = 0 = \Delta_{t_2s}, \qquad \Delta_{t_1s} = \Delta_{t_3s} = 2\frac{u_x^2}{u_0^2 + u_x^2} \tag{4.38}$$

With these impurities again we have a pairing of the eigen-modes of the Cooperon Hamiltonian. However, in this case, the pairing is between states that transform the same way when we exchange valleys. So the degenerate states are ss and t_2s, t_1t_3 and t_3t_3, etc. Looking at the channels for the quantum correction we have that the modes that are odd under $\mathbf{K} \leftrightarrow \mathbf{K}'$ cancel each other in pairs while the even ones contribute equally. This happens because the disorder we are considering does not distinguish between $\mathbf{K}$ and $\mathbf{K}'$, i.e. it commutes with τ_x which generates this transformation.

The appearance of this double degeneracy has to do with the fact that this disorder still preserves C_2 symmetry, a rotation of π around the z-axis. If we include an extra term $\tau_y \sigma_z$ in our disorder:

$$U = u_0 \tau_0 \sigma_0 - u_x \tau_x \sigma_z - u_y \tau_y \sigma_z, \tag{4.39}$$

---

[2]This impurity corresponds to one of the type $\tau_x \sigma_x$ in the normal basis.

the C_2 symmetry is broken. In this case there remains only one gapless mode, the singlet-singlet:

$$\Delta_{ss} = 0, \qquad \Delta_{t_1 s} = 2\frac{u_x^2}{u_0^2 + u_x^2 + u_y^2},$$

$$\Delta_{t_2 s} = 2\frac{u_y^2}{u_0^2 + u_x^2 + u_y^2}, \quad \Delta_{t_3 s} = 2\frac{u_x^2 + u_y^2}{u_0^2 + u_x^2 + u_y^2}. \tag{4.40}$$

In this situation for strong $u_{x,y}$ disorder, the quantum correction will be dominated by the singlet-singlet state only. The singlet will contribute with a positive correction to the conductivity, leading to a WL phase when the intervalley scattering is sufficiently large. Such a phase has already been studied [143] and experimentally observed [144–146, 195] and is indeed the standard phase expected since realistic graphene flakes have atomic defects that activate intervalley scattering.

4.3 Graphene with Rashba SOC

So far we have shown how the innate pseudospin DOF in graphene can activate a WAL phase due to the suppression of backscattering in the presence of scalar impurities. A more "conventional" WL phase settles if the backscattering channel is opened by a more complex impurity landscape for example. The presence of SOC is responsible for a WAL in 2DEG [193] but so far it has remained relatively unexplored in the context of vdW Dirac heterostructures. It is an important topic not only due to the broad appeal that SOC-active 2D materials have for a variety of spintronics applications but also due to the unique way SOC manifests in these, entangling spin and pseudospin. Some works have focused on weak in-band SOC [151, 153] or impurity SOC [152]. Within such approaches the coupling between the spin and pseudospin DOFs is either weak or non-existing. This section is devoted to the impact a strong coupling can have in graphene. For that we shall use the Hamiltonian introduced in Eq.(3.8), that comprises the Rashba SOC, and, using the diagrammatic formalism presented in Chapter 2, go beyond the standard weak SOC limit and explore the case where the spin-splitting is well resolved within the impurity broadening η, i.e. $\alpha > \eta$.

4.3.1 Weak SOC: Cooperon Structure

As previously, we start by computing the disorder corrections to the charge current vertex:

$$\tilde{v}_{x,y} = 2v\left(\sigma_{x,y} + \frac{\alpha}{\epsilon}s_{y,x}\right), \tag{4.41}$$

$$\tilde{v}_{x,y} = 2v\left(1 + \alpha\frac{\epsilon - 2\alpha}{\epsilon^2 + 4\alpha^2}\right)\sigma_{x,y} - \epsilon\frac{\epsilon + 2\alpha}{\epsilon^2 + 4\alpha^2}vs_{y,x}, \tag{4.42}$$

for regimes I and II (see Chapter 3), respectively. The appearance of $s_{x,y}$ in the renormalised vertex structure signals the onset for the Rashba-Edelstein effect by which a charge current is converted into a spin density in the system, introduced in Chapter 1.

The conductivity in regimes I and II is, respectively:

$$\sigma^c = \frac{4v^2}{nu_0^2}\frac{\epsilon\left(\epsilon + 2\alpha\right)}{\epsilon^2 + 4\alpha^2}, \tag{4.43}$$

$$\sigma^c = \frac{4v^2}{nu_0^2}, \tag{4.44}$$

per valley, in units of e^2/h. With both spin and pseudospin as relevant DOFs, the Cooperon is a 16 x 16 matrix making the choice of basis even more important in this case. We can turn the Cooperon matrix block diagonal via the transformation T_θ. This transformation is given by the eigenvectors of the rotation:

$$\Sigma_{\theta_Q} = \begin{pmatrix} 0 & -ie^{-i\theta_Q} \\ -ie^{i\theta_Q} & 0 \end{pmatrix} \otimes \begin{pmatrix} 0 & ie^{-i\theta_Q} \\ -ie^{i\theta_Q} & 0 \end{pmatrix}, \tag{4.45}$$

which rotates the momentum vector $\theta \to 2\theta_Q - \theta$ while leaving the Rashba term invariant. For weak SOC we can expect the sublattice and spin degrees of freedom to be weakly coupled and we can use the *decoupled basis*:

$$\begin{aligned}\{|\sigma s\rangle\} = &\left\{singlet^{A,B} \otimes singlet^{\uparrow,\downarrow}\right\} \oplus \left\{singlet^{A,B} \otimes triplet^{\uparrow,\downarrow}\right\} \oplus \\ &\left\{triplet^{A,B} \otimes singlet^{\uparrow,\downarrow}\right\} \oplus \left\{triplet^{A,B} \otimes triplet^{\uparrow,\downarrow}\right\},\end{aligned} \tag{4.46}$$

where these triplets are the ones given by J_M^* from Eq.(4.19), since we previously saw that these are the ones that diagonalise the W matrix when $\alpha = 0$.

The full expressions for the Cooperon Hamiltonian can be found in Appendix B. Here we will be mainly focused at the structure at $\boldsymbol{Q} = 0$. Building on the previous sections, let us begin by analysing the case of weak SOC $\alpha \ll \eta$. At zero Cooperon momentum, in the absence of SOC the Cooperon

was well described in terms of pseudospin singlet and triplets. As we turn on the SOC, each of these modes will split into four modes which are, up to small corrections in α, spin triplets and singlets. So for small SOC the physics is well described in terms of spin and pseudospin two particle states. For now let us focus on the modes that are borne from the pseudospin singlet, since the others had large gaps without SOC already. In Table 4.1 the states and their respective gaps are shown. Firstly we see that the pseudospin singlet-spin singlet state (henceforth shortened to singlet-singlet) ss state is the only gapless one and the singlet-triplet states acquire masses proportional to the Dyakonov-Perel relaxation rate $\tau_{DP}^{-1} = 4\alpha^2 \tau_{\mathrm{p}}$ [196] and have small mixing with other pseudospin triplet states. These are quite small gaps so all four states are relevant and the quantum correction to the conductivity is only slightly altered relative to its value without SOC.

State	ss	$st_1^\star - 2\alpha\tau_{\mathrm{p}}t_1^\star t_3^\star$	$st_2^\star - 2\alpha\tau_{\mathrm{p}}t_2^\star t_3^\star$	$st_3^\star - 2\alpha\tau_{\mathrm{p}}\left(t_1^\star t_2^\star + t_2^\star t_1^\star\right)$
Gap	0	$\tau_{\mathrm{p}}/2\tau_{DP}$	$\tau_{\mathrm{p}}/2\tau_{DP}$	$\tau_{\mathrm{p}}/\tau_{DP}$

Table 4.1: The low energy Cooperon Hamiltonian eigenstates and their respective gaps, in the limit of small SOC.

Figure 4.3 shows a close up of the 4 low energy states, the pseudospin singlet states.
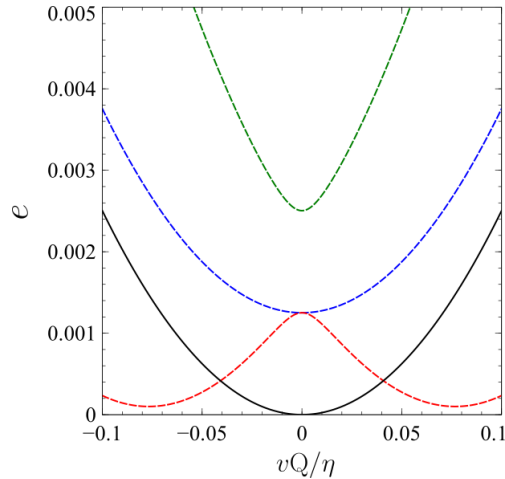
Figure 4.3: The small momentum behaviour of the low energy eigenstates of the Cooperon Hamiltonian for small SOC: $\alpha = 0.1$ meV, $\epsilon = 0.2$ eV. These are the states that split from the pseudospin singlet with the coloured dashed lines corresponding to spin triplets and the solid black line to the singlet. The latter is the only gapless mode but the triplets still compete significantly as long as their gaps remain small.

4.3.2 Weak SOC: The Weight Matrix

For weak SOC we have:

$$W^\star = \begin{pmatrix} W_{11} & 0 & W_{13} & 0 \\ 0 & W_{22} & 0 & 0 \\ -W_{13} & 0 & W_{33} & W_{34} \\ 0 & 0 & -W_{34} & 0 \end{pmatrix} \tag{4.47}$$

in the decoupled basis. The 4 x 4 blocks are given by:

$$W_{11} = \frac{\epsilon}{4\eta^3} \begin{pmatrix} -1 & 0 & 0 & 0 \\ 0 & 1 & 0 & 0 \\ 0 & 0 & 1 & 0 \\ 0 & 0 & 0 & 1 \end{pmatrix}, \tag{4.48}$$

$$W_{13} = i\frac{\alpha}{2\eta^3} \begin{pmatrix} 0 & 1 & 0 & 0 \\ 1 & 0 & 0 & 0 \\ 0 & 0 & 0 & 0 \\ 0 & 0 & 0 & 0 \end{pmatrix}, \quad W_{34} = -i\frac{\alpha}{4\eta^3} \begin{pmatrix} 0 & 0 & 0 & 0 \\ 0 & 0 & 0 & 1 \\ 0 & 0 & 0 & 0 \\ 0 & 1 & 0 & 0 \end{pmatrix}, \tag{4.49}$$

with the relations $W_{22} = -W_{11}/4$ and $W_{33} = -3W_{11}/4$. The weight matrix in this limit is almost diagonal, with off-diagonal terms being $\sim \mathcal{O}\left(\alpha/\epsilon\right)$, and determines the sign of the four low gap states: the singlet-singlet is WL and the singlet-triplets are WAL. As a general rule, the sign of the contribution is determined by the parity of the state under particle exchange, such that an odd state is WAL. This form also justifies ignoring the matrix structure of W and taking simply a weighted trace of the Cooperon to compute the quantum correction to the conductivity, an approximation that is widely used [151, 152, 155].

4.3.3 Cooperon Structure: High SOC Limit

We now turn to the strong SOC case, which, in this instance, means that the Rashba spin gap starts to be well resolved within the disorder broadening: $\alpha \gtrsim \eta$. In the presence of strong spin-orbit interaction the spin and pseudospin degrees of freedom of Dirac fermions become heavily entangled. This has deep consequences for the quantum nature of the charge carriers and can be seen already at the Cooperon level.

Firstly, the Cooperon Hamiltonian modes are no longer simple two parti-

cles product states of spin and pseudospin. What's more, we shall show that the perturbative treatment of the Cooperon momentum no longer accurately captures the physics behind quantum coherence effects. Our discussions so far have relied on the assumption that the biggest contribution for the quantum corrections come from $Q \approx 0$, allowing for a small momentum expansion. This assumption is not valid when α approaches η, as there are some states that, even though they are gapped at $Q = 0$, they have a minimum at finite momentum. In this way, there is a large contribution coming from those states away from the origin, rendering the small momentum expansion inappropriate. Using the Eq.(E.10) derived in section E of the Appendix we computed the Cooperon non-perturbatively in Q. This approach hinges on the assumption $\epsilon \gg \alpha$ but, crucially, it allows us to accurately study the regime where the Cooperon momentum is larger than the disorder broadening, which is fundamental to capture the physics of the low energy Cooperon states at finite momentum, that appear for $\alpha \approx \eta$. In Fig. 4.4 it is clear that the perturbative approach (dashed lines) are not accurate for $vQ \gtrsim \eta$. In the conventional weak SOC limit this is not an issue since the main contribution comes from the gapless mode at small Q and thus differences in the high energy modes for large momenta are typically not significant.

Using Eq.(E.5), we now turn to the case of strong SOC, $\alpha \approx \eta$. The entanglement between the pseudospin and spin has deep consequences for the Cooperon structure. We find the Cooperon Hamiltonian to no longer be well described by product states. As these states evolve they start increasing in energy, leaving the only gapless state, singlet-singlet, dominating the quantum interference correction. This leads to a non-trivial transition, where the SOC drives the system from WAL towards WL due to the high mass that the SU(4) states acquire. The gaps and states at zero momentum can be found in Appendix C.

4.3.4 The Weight Matrix: High SOC Limit

The weight matrix now takes a more complex form, in the decoupled basis it can be written as:

$$W^{\star} = \begin{pmatrix} W_{11} & W_{12} & W_{13} & W_{14} \\ W_{12}^{\dagger} & W_{22} & W_{23} & W_{24} \\ W_{13}^{\dagger} & W_{23} & W_{33} & W_{12}^{\dagger} \\ W_{14} & W_{24}^{\dagger} & W_{12} & W_{44} \end{pmatrix} \tag{4.50}$$
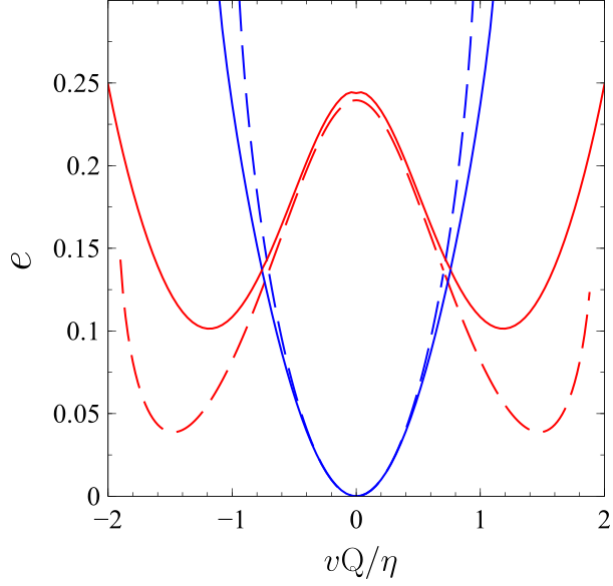
Figure 4.4: Comparison between the Cooperon Hamiltonian modes obtained using a treatment perturbative (dashed lines, Eq.(2.44)) and non-perturbative in Q (solid lines, Eq.(2.45)). The discrepancies are noticeable for $vQ \approx \eta$. For the ss state, in blue, this difference is not important as it happens at higher energies, for the other state (red lines) though this difference is very significant as the perturbative approach will overestimate its contribution for finite momentum due to the much more pronounced minimum in the dispersion. Parameters used: $\epsilon = 0.2$ eV; $\eta = 0.7$ meV and $\alpha = 2\eta/3$.

with the 4x4 blocks:

$$W_{11} = \begin{pmatrix} -\frac{2\alpha^2+\epsilon^2}{4\eta^3\epsilon} & 0 & 0 & 0 \\ 0 & \frac{3\epsilon^3}{16\eta^3(\epsilon^2-\alpha^2)} & 0 & 0 \\ 0 & 0 & \frac{\epsilon^3}{16\eta^3(\epsilon^2-\alpha^2)} & 0 \\ 0 & 0 & 0 & 0 \end{pmatrix}, \tag{4.51}$$

$$W_{22} = \begin{pmatrix} \frac{\epsilon^3}{16\eta^3(\epsilon^2-\alpha^2)} & 0 & 0 & 0 \\ 0 & \frac{8\alpha^4-6\alpha^2\epsilon^2-\epsilon^4}{32\eta^3\epsilon(\epsilon^2-\alpha^2)} & 0 & 0 \\ 0 & 0 & \frac{8\alpha^4-2\alpha^2\epsilon^2-\epsilon^4}{32\eta^3\epsilon(\epsilon^2-\alpha^2)} & 0 \\ 0 & 0 & 0 & 0 \end{pmatrix}, \tag{4.52}$$

$$W_{33} = \begin{pmatrix} \frac{3\epsilon^3}{16\eta^3(\epsilon^2-\alpha^2)} & 0 & 0 & 0 \\ 0 & \frac{8\alpha^4-2\alpha^2\epsilon^2-5\epsilon^4}{32\eta^3\epsilon(\epsilon^2-\alpha^2)} & 0 & 0 \\ 0 & 0 & \frac{8\alpha^4-6\alpha^2\epsilon^2-\epsilon^4}{32\eta^3\epsilon(\epsilon^2-\alpha^2)} & 0 \\ 0 & 0 & 0 & 0 \end{pmatrix}, \tag{4.53}$$

$$W_{44} = \begin{pmatrix} 0 & 0 & 0 & 0 \\ 0 & 0 & 0 & 0 \\ 0 & 0 & 0 & 0 \\ 0 & 0 & 0 & -\frac{\alpha^2\left(\epsilon^2-2\alpha^2\right)}{4\eta^3\epsilon(\epsilon^2-\alpha^2)} \end{pmatrix}, \tag{4.54}$$

$$W_{12} = i\frac{\alpha}{16\eta^3} \begin{pmatrix} 0 & 0 & 0 & 0 \\ 0 & 0 & 0 & 0 \\ \frac{3\epsilon^2-4\alpha^2}{\epsilon^2-\alpha^2} & 0 & 0 & 0 \\ 0 & 0 & 0 & 0 \end{pmatrix}, \quad W_{13} = i\frac{3\alpha}{16\eta^3} \begin{pmatrix} 0 & \frac{8}{3} & 0 & 0 \\ \frac{3\epsilon^2-4\alpha^2}{\epsilon^2-\alpha^2} & 0 & 0 & 0 \\ 0 & 0 & 0 & 0 \\ 0 & 0 & 0 & 0 \end{pmatrix}, \tag{4.55}$$

$$W_{23} = \begin{pmatrix} 0 & 0 & 0 & 0 \\ 0 & 0 & \frac{8\alpha^4-6\alpha^2\epsilon^2-\epsilon^4}{32\eta^3\epsilon(\epsilon^2-\alpha^2)} & 0 \\ 0 & \frac{8\alpha^4-10\alpha^2\epsilon^2+\epsilon^4}{32\eta^3\epsilon(\epsilon^2-\alpha^2)} & 0 & 0 \\ 0 & 0 & 0 & 0 \end{pmatrix}, \tag{4.56}$$

$$W_{24} = i\frac{\alpha}{16\eta^3} \begin{pmatrix} 0 & 0 & 0 & 0 \\ 0 & 0 & 0 & 0 \\ 0 & 0 & 0 & \frac{\epsilon^2-4\alpha^2}{\epsilon^2-\alpha^2} \\ 0 & 0 & 0 & 0 \end{pmatrix}. \tag{4.57}$$

The states st_3, $t_1^\star t_3$ $t_2^\star t_3$, $t_3 s$, $t_3 t_1^\star$ and $t_3 t_2^\star$ do not contribute to the quantum correction. Furthermore, the diagonal entries follow the general trend wherein a state that is odd (even) under particle swap contributes for WAL (WL). However, now we cannot neglect the off-diagonal components that strongly couple different states. In the strong SOC regime, the matrix structure of the weight matrix should be taken into account.

4.3.5 The Quantum Correction to the Conductivity: High SOC

The quantum correction to the conductivity is presented in Fig. 4.5 (black line) as a function of the SOC strength relative to the disorder broadening. We employed the non-perturbative expression for the Cooperon in order to access the large SOC regime of $\alpha \approx \eta$. The figure can be divided in two main regions: one that is WAL, for $\alpha < \eta$ and a WL one for $\alpha > \eta$. The former starts with the absence of SOC, where the gapless pseudospin singlet dominates with a positive contribution to $\Delta\sigma$. Spin orbit interaction then splits this mode into four. Of these, only the singlet-singlet mode (WL in nature) remains gapless, however, the spin triplets contribute with an opposite sign and, for weak SOC they dominate the corrections and thus the

system remains in a WAL phase. Furthermore these triplets acquire minima in their dispersion relations away from $\boldsymbol{Q} = 0$ that become deeper with the increase of α which explains the initial increase of $\Delta\sigma$. The curve then hits a peak as we approach the strong SOC regime. At this point the gaps of these low-lying states start becoming too large and their minima less pronounced so that their contribution becomes less significant. The singlet-singlet state remains unaffected and eventually becomes the dominant mode changing the sign of the quantum corrections[3]. This is a transition from a WAL phase to a WL phase driven by spin orbit interactions that strongly couples the pseudospin and spin degrees of freedom in the Dirac system. This is in stark contrast to what is typically found in conventional metals where SOC drives the towards a WAL phase.

4.4 Rashba SOC and Intervalley Impurities

Finally, in this section we treat the full problem of the Dirac Rashba system with intervalley scattering in the disorder potential. This is fundamental to study the effect of point defects that are ubiquitous in current samples. We start from the Hamiltonian:

$$\mathcal{H}_{b\mathbf{p}} = v\boldsymbol{\sigma} \cdot \mathbf{p} + \alpha\left(\sigma_x s_y - \sigma_y s_x\right), \qquad (4.58)$$

written in the magic basis 2 from Table 3.1 (we omitted the identity matrix acting on the valley space). We choose the disorder potential

$$U = u_0 + u_x \tau_x \sigma_z + u_y \tau_y \sigma_z \qquad (4.59)$$

since it preserves time reversal symmetry but is general enough that it does not lead to duplicated gapless modes in the Cooperon structure, as we saw in Section 4.2.3. We assume Gaussian "white noise" statistics where the different disorder types are uncorrelated, which has the advantage of not generating any additional matrix structures in the self energy. This means that the disorder averaged GF is simply a diagonal matrix in the valley space, with two copies of the GF from Eq.(3.19), one for each valley. Generally there will be correlations between the different disorder terms but cannot open any more gaps in the Cooperon modes and therefore should alter qual-

---

[3]This is because the singlet-singlet state is also part of the total angular momentum basis for the SU(4) algebra.

itatively our results. The self energy (in regime II for example) becomes:

$$\Sigma^R = -in \left(u_0^2 + u_x^2 + u_y^2 \right) \frac{\epsilon}{4v^2}. \tag{4.60}$$

We define the intra and intervalley scattering rates as:

$$\tau_v^{-1} = n u_0^2 \frac{\epsilon}{4v^2}, \tag{4.61a}$$

$$\tau_{iv}^{-1} = n \left(u_x^2 + u_y^2 \right) \frac{\epsilon}{4v^2}. \tag{4.61b}$$

Although tackling this problem is technically very complicated due to the size of the objects involved (the Cooperon is now a 64×64 matrix), conceptually we can easily understand it by simply combining the two pictures that we already have for the SOC case and the intervalley impurity. We expect the modes observed in the Dirac-Rashba model with scalar impurities to split into valley singlets and triplets with the valley singlet remaining the only gapless state. For large enough intervalley scattering rate this gapless state should be the sole dominant contribution and change the sign of the quantum corrections from WAL to WL (weak SOC) or from WL to WAL (strong SOC). There is still the question of how strong must the intervalley scattering rate be. This is important to understand how robust is the new SOC driven WL phase analysed in the previous section. To answer this question we must carry out the calculation. This task is significantly simplified by making use of the properties of tensor products. In essence, the Cooperon is obtained via:

$$\mathcal{H}_C \sim \mathcal{G}^R \otimes \mathcal{G}^A = \left(\mathbf{1}_2 \otimes \mathcal{G}_{1v}^R \right) \otimes \left(\mathbf{1}_2 \otimes \mathcal{G}_{1v}^A \right), \tag{4.62}$$

with $\mathbf{1}_n$ being an $n \times n$ identity matrix and the $1v$ subscript indicates that the GF is for one valley only. We want to make use of the Cooperon for a single valley that we have already computed. For that we start from the object

$$\tilde{\mathcal{H}}_C = \mathbf{1}_4 \otimes \mathcal{H}_{C,1v}, \tag{4.63}$$

which is essentially the true Cooperon Hamiltonian but in a basis that is a reordering of the usual tensor product basis from Eq.(4.62). Hence, we can write

$$\mathcal{H}_C = \mathcal{S}^{-1} \tilde{\mathcal{H}}_C \mathcal{S}, \tag{4.64}$$

and similarly for the weight matrix. The explicit form of the transformation matrices used is given in Appendix D. To get the final result we need to invert and integrate the Cooperon in the momentum, which we do numerically (making use of the T_θ transformation for the inversion). The results for $\Delta\sigma$ are shown in Fig. 4.5 in the coloured lines. The novel SOC driven WL phase seen before is extremely sensitive to intervalley scattering since already for values of $\tau_{iv}^{-1} = \tau_v^{-1}/10$ it is replaced by a more conventional transition from WL to WAL in the presence of strong SOC. This makes experimental detection of this new WL phase difficult as experiments put $\tau_{iv} \sim 1$ps and less than 10 times greater than τ_v [146, 197].
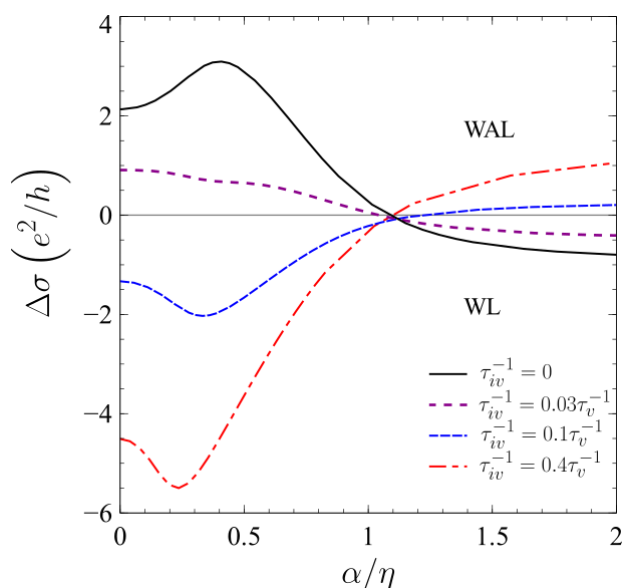
Figure 4.5: The interference correction to the conductivity in graphene with Rashba SOC. The black line depicts the case without intervalley scattering and showcases the unusual SOC driven WL phase that settles in the strong SOC regime ($\alpha > \eta$). The case with intervalley impurities is captured by the coloured lines. The WL at strong SOC still survives for very low intervalley scatering rates (purple curve). However, already for intervalley rates ten times smaller than the intravalley scattering rate the new SOC driven WL phase is destroyed and replaced by the conventional picture of a WL→WAL transition in the presence of SOC. Parameters used: $\epsilon = 0.2$ eV, $L = 1$ μm, $\ell = 0.3$ μm and $n = 10^{14}$ cm^{-2}.

4.5 Conclusions

In this chapter we have studied the quantum interference corrections to the conductivity in graphene with proximity-induced SOC. The inherent pseudospin DOF which couples to the momentum, mimicking SOC and leading

to a WAL phase. If spin and isospin are not irrelevant DOFs (either via impurities or in band effects) we need to take into account the interference between them as well. These interactions split the modes into simple singlet/triplets states (in the case of impurities) or more complicated states (in the case of strong in-band effects). Generally, the quantum corrections are dominated by singlet states as long as time reversal symmetry is preserved. The exceptions are the cases where the disorder potential preserves some rotation symmetries of the system leading to pairwise cancellations between states that change under that transformation.

In the presence of strong Rashba SOC, graphene hosts a WL phase unlike what happens in conventional conductors. To access this new phase it is necessary to perform the calculation non-perturbatively in the Cooperon momentum in order to accurately capture the low energy behaviour of some states at $vQ \approx \eta$. This new phase unveiled in this thesis is highly sensitive to intervalley scattering and it quickly gives way to the conventional picture of WAL with strong SOC. This extreme sensitivity is the underlying reason why no studies so far have managed to capture experimentally the WAL phase that should exist in pristine graphene (i.e. absence of intervalley scattering and meaningful spin orbit interactions), but rather an impurity driven WL [144–146, 195]. Similarly, magnetotransport studies on graphene/TMD heterostructures have reported WAL[141, 148, 149, 198, 199]. The SOC-driven WL phase should be observed in ultraclean samples with minimal point defects.

Chapter 5

Spin-Orbit Torque

5.1 Preliminaries

The physics of spin-orbit torque is deeply intertwined with non-equilibrium spin polarisations that can be generated in materials with broken inversion symmetry via an external electric field. The diagrammatic formalism presented in Chapter 2 allows us to study the extrinsic (i.e. impurity driven) contribution to these non-equilibrium phenomena even in the presence of strong SOC, which is vital for an accurate understanding of the SOT in ferromagnetic vdW heterostructures within the diffusive regime.

Ultimately, the goal is to predict how the magnetisation of our system will change once a current is driven through it or through a material coupled to it. We will restrict ourselves to ferromagnetic materials although the formalism can be extended to anti-ferromagnetic systems. Let the magnetisation of the ferromagnet (FM) be given by $M = M_s\mathbf{m}$, with M_s the saturation magnetisation and $\mathbf{m}$ the unit vector. The dynamics of the magnetisation are controlled by the Landau-Lifshitz-Gilbert (LLG) equation [63, 92]:

$$\frac{\mathrm{d}\mathbf{m}}{\mathrm{d}t} = -\gamma\mathbf{m}\times\mathbf{B_M} + \alpha_{\mathrm{G}}\mathbf{m}\times\frac{\mathrm{d}\mathbf{m}}{\mathrm{d}t} + \frac{\gamma}{M_s}\mathbf{T}, \qquad (5.1)$$

where γ is the gyromagnetic ratio (with units $\mathrm{T}^{-1}\mathrm{s}^{-1}$) and α_{G} the dimensionless Gilbert damping parameter. The first term in the rhs of Eq.(5.1) accounts for the precession of the magnetisation around the effective magnetic field $\mathbf{B_M}$ that is generated by all the magnetic moments of the FM. The second term is the damping that will make the magnetisation relax towards

its equilibrium position. Finally, the third term includes all torques that are exerted by the conduction electrons on the magnetisation and is our main focus. We will derive microscopically the torques that are generated in a 2D interface between the thin FM and a spin-orbit active 2D material that are coupled via a a ferromagnetic interaction with strength Δ_{xc}. In this case the generated torque can be written as [92]:

$$\mathbf{T} = -\frac{\Delta_{xc}}{d}\mathbf{m} \times \mathbf{S}, \tag{5.2}$$

where $\mathbf{S}$ is the current driven spin density. The appearance of the FM film thickness d reflects 2D origin of the torque since, the thicker the FM is, the harder it is to induce magnetisation switching via SOT. This non-equilibrium spin polarisation $\mathbf{S}$ occurs at the level of the 2D layer and is activated a combination of SOC and a magnetic exchange interaction induced by the FM film via proximity effects.

Within linear response theory we write $\mathbf{S} = \hat{K}^J \cdot \mathbf{J}$, where the spin density response to an applied current density $\mathbf{J}$ is controlled by the 3×2 tensor $\hat{K}^J = \hat{K} \cdot \hat{\sigma}^{-1}$ that contains the spin susceptibility response tensor $\hat{K}$ and the conductivity tensor $\hat{\sigma}$. These response functions are given by:

$$K_{\alpha\beta} = 2\pi \sum_{\mathbf{p}} \mathrm{Tr} \left\{ s_\alpha \mathcal{G}_{\mathbf{p}}^R \tilde{v}_\beta \mathcal{G}_{\mathbf{p}}^A \right\}, \tag{5.3}$$

$$\sigma_{\alpha\beta} = \frac{1}{2\pi} \sum_{\mathbf{P}} \mathrm{Tr} \left\{ v_\alpha \mathcal{G}_{\mathbf{p}}^R \tilde{v}_\beta \mathcal{G}_{\mathbf{p}}^A \right\}, \tag{5.4}$$

which are particular cases of Eq.(2.22), and, as we have seen in Chapter 2, can be computed using the Diffuson method. This is a controlled and accurate probe into the extrinsic mechanisms behind SOT which dominate in the diffusive regime due to their semi-classical scaling $\sim 1/n$ [164].

The current induced SOT is conventionally classified into two categories: the field-like torque (T_{odd}) is $\mathbf{m}$-odd and acts like an effective magnetic field and the damping-like torque (T_{even}) which is $\mathbf{m}$-even and renormalises the damping parameter in the LLG equation. Assuming a perturbative expansion of the torque in terms of the magnetisation is possible we can write:

$$\mathbf{T}_{odd} = t_{o1}\, \mathbf{m} \times (\hat{z} \times \mathbf{J}) + t_{o2}\, \mathbf{m} \times (\mathbf{m} \times \hat{z})(\mathbf{m} \cdot \mathbf{J}) + \mathcal{O}\left(\mathbf{m}^5\right), \tag{5.5a}$$

$$\mathbf{T}_{even} = t_{e1}\, \mathbf{m} \times (\mathbf{m} \times (\hat{z} \times \mathbf{J})) + t_{e2}\, \mathbf{m} \times \hat{z}\,(\mathbf{m} \cdot \mathbf{J}) + \mathcal{O}\left(\mathbf{m}^4\right), \tag{5.5b}$$

with the torque parameters $t_{e1,2}$ and $t_{o1,2}$ are to be determined and should not depend on the magnetisation unit vector $\mathbf{m}$. Of particular importance is the damping-like torque since it is responsible for the much sought after magnetic switching in this devices. Rigorously, it does not suffice to look into the parity with respect to $\mathbf{m}$ and one needs to perform a vector spherical harmonics decomposition of each term SOT term to discern its nature, especially in the presence of strong in-plane magnetisation [200]. In that case, both t_{ei} and t_{oi} will yield field and damping-like contributions. The leading contributions are nonetheless as we have denoted them (with the exception of t_{o2} which strongly mixes field-like and damping-like SOT). Keeping this in mind, however, from now on refer to the different torques as is commonly done with t_{oi} being field-like and t_{ei} damping-like.

In the subsequent sections we will show how to use diagrammatic methods to compute the torque parameters in the case of a thin FM coupled to a monolayer transition metal dichalcogenide (TMD), invariant under 3-fold rotations. To that end we will use the Hamiltonian from Equation (3.22), with focus on regime II.

5.2 Symmetry Analysis of the Magnetised C_{3v} Dirac-Rashba Model

We start by performing a symmetry analysis of the problem to find out what kind of terms are possible within our system. To determine the symmetries, it suffices to consider the "empty" bubble (no vertex corrections). Using the commutation relations between the different Pauli matrices together with the Hamiltonian properties under the transformation $\mathbf{m} \to -\mathbf{m}$ (see details on section F of the Appendix) the response function admits the following general structure (sum over repeated indices is implied):

$$\hat{K} = \begin{pmatrix} \mathfrak{m}_z \kappa_{xx} + \mathfrak{m}_a^2 \vec{\alpha}_\xi \cdot \vec{f^a_{xx}} + \vec{\alpha}_\xi \cdot \vec{g} & \kappa_{xy} + \mathfrak{m}_z \vec{\alpha}_\xi \cdot \vec{f_{xy}} + \mathfrak{m}_a^2 h^a_{xy} \\ -\kappa_{xy} - \mathfrak{m}_z \vec{\alpha}_\xi \cdot \vec{f_{xy}} + \mathfrak{m}_a^2 h^a_{yx} & \mathfrak{m}_z \kappa_{yy} + \vec{\alpha}_\xi \cdot \vec{g} + \mathfrak{m}_a^2 \vec{\alpha}_\xi \cdot \vec{f^a_{yy}} \\ \mathfrak{m}_x \kappa_{zx} + \mathfrak{m}_z \mathfrak{m}_x \vec{\alpha}_\xi \cdot \vec{z_{zx}} & \mathfrak{m}_z \mathfrak{m}_x \kappa_{zy} + \mathfrak{m}_x \vec{\alpha}_\xi \cdot \vec{z_{zy}} \end{pmatrix}, \quad (5.6)$$

where $\vec{\alpha}_\xi = \xi(\lambda_{\text{sv}}, \Delta)$. The coefficients $\{\kappa_{ia}, \mathbf{f}^a, \mathbf{g}, h^a, \mathbf{z}\}$ are even functions of $\mathfrak{m}_x$ and $\mathfrak{m}_z$. In the particular case of $\lambda_{\text{sv}} = \Delta = 0$, K_{xx}, K_{yy} and K_{zy} are odd (even) in m_z (m_x), so that any anisotropy effect in the generation of spin density collinear with the applied electric field must be at least $\mathcal{O}(m_x^2)$.

Similarly, $K_{xy} = -K_{yx} + \mathcal{O}\left(m_x^2\right)$, with these terms being instead even in m_z since they encode the REE, which is already present in the non-magnetised system [188]. The only terms odd in m_x are K_{zx} and K_{zy} so the generation of out-of-plane spin polarisation necessitates an anisotropic deformation of the Fermi surface. The inclusion of λ_{sv} and Δ, possible due to the the breaking of sublattice symmetry, activates terms linear in $\vec{\alpha}_\xi$ that vanishing upon the summation over the two valleys.

5.3   An Intuitive Picture: Using Boltzmann

While the powerful diagrammatic formalism allows us to get accurate values for the dominant disorder-induced responses in the diffusive limit, a simpler geometric analysis based on the spin texture at the Fermi surface is capable of not only determining which responses should we expect in the system but also of providing a physical intuition for such phenomena. To simplify our analysis we restrict ourselves to the C_{6v}-invariant model ($\lambda_{sv} = \Delta = 0$) with a proximity induced FM interaction. In the spirit of the Boltzmann formalism introduced in Section 2.3.2 we write the non-equilibrium spin polarisation in terms of the distortion of the Fermi surface due to the applied electric field $\delta f_{\pm,\mathbf{p}}$, such that:

$$\mathbf{S} = \sum_{\mathbf{p}} \langle \mathbf{s} \rangle_{+,\mathbf{p}} \left(\delta f_{+,\mathbf{p}} - \delta f_{-,\mathbf{p}} \right), \tag{5.7}$$

where $\langle \mathbf{s} \rangle_{+,\mathbf{p}}$ is the average value of the spin operator on the state $|k\rangle_+$ whose dependence on the $\mathbf{p}$-direction is shown in Eqs.(3.27a)-(3.27c). We have already taken into account that the two bands ($\uparrow$ / $\downarrow$) have opposite spin polarities. The other piece needed for the response is the deviation of the Fermi surface from its equilibrium value:

$$\delta f_{\mathbf{p}}^\nu \propto \tau_\parallel^\nu \, \hat{\mathbf{p}} \cdot \boldsymbol{\mathcal{E}} + \tau_\perp^\nu \left(\hat{\mathbf{p}} \times \boldsymbol{\mathcal{E}} \right)_z. \tag{5.8}$$

Here we are interested simply in the angular dependencies so that we know which terms survive the integration on Eq.(5.7)[1]. The current-induced deviation of the Fermi surface is written using the parallel transport times $\tau_\parallel^\nu$ that controls the deviation along the direction of the electric field and is therefore connected to forward scattering processes; and the transverse transport

---

[1] Both v_F and p_F carry angular dependences in the presence of m_x. These, however, vanish upon angular integration so we neglect them in the analysis.

times $\tau_\perp^\nu$ that in turn are behind skew scattering generating imbalances in the scattering cross section between angles $\pm\theta$ relative to $\mathcal{E}$. This skewness plays an crucial role in activating damping-like SOT terms which play a major role in magnetisation switching.

Let us start our analysis by taking the electric field to be along the $\hat{x}$-direction so that $\delta f_{\mathbf{k}}^\nu \propto \tau_\parallel^\nu \mathcal{E}_x \cos\theta - \tau_\perp^\nu \mathcal{E}_x \sin\theta$. The longitudinal distortion of the distribution function ($\propto \tau_\parallel$) breaks the equivalence between points in the Fermi surface along this direction, so that a spin imbalance is created leading to the generation of an in-plane spin polarisation along $\hat{y}$. This is the well known REE that is already present in the usual non-magnetic Dirac-Rashba model [54, 188]. Concurrently, the skewness term $\tau_\perp$ is responsible for two extra effects. Firstly, it picks up a contribution from Eq.(3.27a) to S_x. Similarly to the previous effect, this is a current-induced spin polarisation that is generated due to a spin imbalance, but in this case the imbalance occurs perpendicularly to $\mathcal{E}$ due to skewness, so that the spin density generated is along the current direction. Since it does not require m_x, it is already present in isotropic systems. This phenomenon, that we shall call collinear Edelstein effect, can be generated efficiently since it is still a semi-classical effect, scaling with the impurity density as n^{-12}. Lastly, an out-of-plane spin response is generated via a mechanism combining skewness and the anisotropy in the s_z texture due to the in-plane exchange coupling. It is the left-right imbalance together with the angle dependence of the s_z spin texture that activate this response.

We can apply the same reasoning when the electric field is along the $\hat{y}$-direction. Just like previously, the REE and the collinear version are present but now generate a S_x and S_y response, respectively. An additional out-of-plane non-equilibrium spin polarisation is also generated, however, in this case, it is captured by $\tau_\parallel$, not requiring any sort of skewness, since the anisotropy direction of the out-of-plane spin texture coincides with the direction of the applied electric field. All these mechanisms can be visualised using Figure 5.1. The reasoning outlined above provides a general and intuitive tool to predict which SOTs are operative in different systems, by analysing their spin textures.

Both the collinear Edelstein effect and the generation of out-of-plane spin polarisation discussed are new effects which can have important contributions towards SOT as we shall see in the next section. It is important to note

---

[2]Note that the formalisms that we use are meant to study diffusive processes that hinge on the presence of impurities. Therefore, the $n = 0$ is not contemplated in this work.
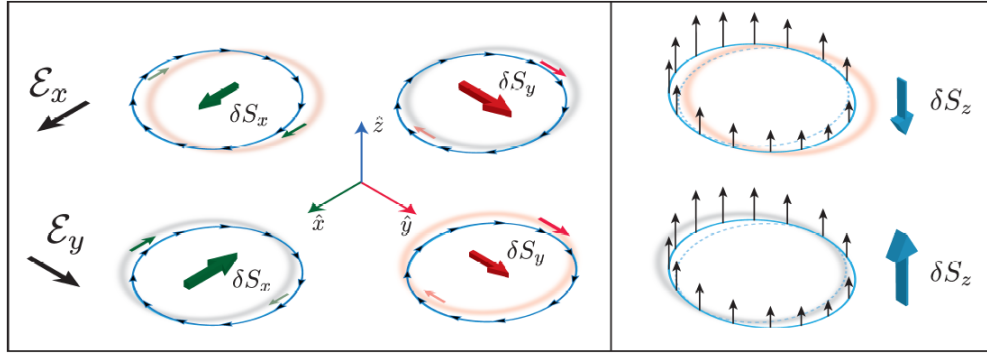
Figure 5.1: Spin responses responsible for the SOT mechanisms in the system can be understood based on the spin texture and the deformation of the Fermi surface due the electric field $\mathcal{E}$. For simplicity, only the spin majority band (blue line) is shown. The image is divided into in-plane response (left block) and out-of-plane (right block). The responses on the top (bottom) row are activated by an electric field along $\hat{x}$ ($\hat{y}$), assuming in-plane magnetisation to be along $\hat{x}$. The shadowed grey (red) circles represent the field-induced distortion parallel (perpendicular) to the applied field, described by $\tau_\parallel$ and $\tau_\perp$ in Eq.(5.8).

that these arguments are applicable to each band separately. Since they have opposite spin polarities it would be possible for the effects to cancel when summing over the two bands. This however is not to be expected since the two bands have different Fermi momenta and a rigorous calculation proves that all the effects listed above are indeed present even when the two opposite spin bands are populated.

We finish this discussion by drawing the comparison between the magnetised Dirac-Rashba model here discussed and the 2DEG Rashba model with induced exchange interaction [90]. The Rashba-Edelstein effect is operative in both systems since they share the winding spin texture around the Fermi rings. However, the different nature of the dispersions is important. In the 2DEG there is a cancellation between the two bands that negates the simple mechanism outlined above for the generation of S_z via $\mathcal{E}_y$. Furthermore, the skew-scattering-activated mechanisms are not as robust in the 2DEG [201].

5.4   Diagrammatics on the SOT

The main goal of this section is to develop an accurate microscopic theory of SOT that incorporates disorder effects self consistently. To that end we employ the diagrammatic formalism outlined in Chapter 2. This technique allows us to treat all the couplings *non-perturbatively* enabling the

study of a variety of rich regimes, including the more experimentally relevant case of proximitised materials with competing energy scales $\alpha \approx \Delta_{xc}$. Furthermore, by summing all single impurity diagrams using T-Matrix insertions in the vertex corrections we capture all processes that contribute at the semi-classical level. Such an approach has proved to be more accurate than the standard ladder diagrams approximation and has the advantage of not only bridging the gap between the weak scattering Gaussian approximation and the unitary limit (the case of vacancies), but also capturing the skew-scattering mechanisms [164]. We can obtain simple analytical expressions in the weak scattering limit by expanding the GF in the anisotropy m_x in Dyson's series [90].

In order to study the charge-spin conversion phenomena in weakly disordered systems we focus on the Fermi surface contributions that are captured using Eq.(5.3). The 3×2 K tensor encodes every charge-to-spin response. From the symmetry analysis done in Section 5.2 we can infer the following form for the charge current-to-spin response tensor:

$$\hat{K}^J = \begin{pmatrix} m_z \kappa_{xx}^{ss} & \kappa_{xy} \\ \kappa_{yx} & m_z \kappa_{yy}^{ss} \\ m_x \kappa_{zx}^{ss} & m_x m_z \kappa_{zy} \end{pmatrix}, \tag{5.9}$$

where the superscript ss marks the responses that are activated by skew scattering. And similarly for the conductivity:

$$\hat{\sigma}^c = \begin{pmatrix} \sigma_{xx} & m_z \sigma_{xy}^{ss} \\ m_z \sigma_{yx}^{ss} & \sigma_{yy} \end{pmatrix}. \tag{5.10}$$

We have made explicit which terms are odd upon inversion of the magnetisation components so that the terms $\kappa_{\alpha\beta}$ and $\sigma_{\alpha\beta}$ are even functions in m_x and m_z.

With the decomposition in Eq.(5.9), the $\hat{K}$ tensor elements and the torque parameters from Eqs.(5.5b) and (5.5a) are related via:

$$t_{o1} = \Delta_{xc} \left(\kappa_{xy} - m_x^2 \kappa_{zy} \right); \quad t_{o2} = \Delta_{xc} \left(\frac{\kappa_{xy} + \kappa_{yx}}{m_x^2} - \kappa_{zy} \right); \tag{5.11a}$$

$$t_{e1} = \Delta_{xc} \kappa_{yy}; \quad t_{e2} = \Delta_{xc} \left(\frac{\kappa_{xx} - \kappa_{yy}}{m_x^2} - \kappa_{zx} - \kappa_{xx} \right). \tag{5.11b}$$

In order to accurately capture the diffusive regime, we perform the calculations using T-Matrix insertions in the Bethe-Salpeter equation for the renor-

malised current vertex. For that we can use Eq.(2.28):

$$K_{\alpha\beta} = \frac{2}{\pi} \left[(\mathcal{D} - 1) \, \Upsilon^{-1} \right]_{\beta\alpha} \qquad (5.12)$$

where now $\alpha = 2\,(s_x)\,, 3\,(s_y)\,, 4\,(s_z)$ runs the indices that cover the spin density operators and $\beta = 5\,(\sigma_x)\,, 9\,(\sigma_y)$ covers the velocity operators.

5.4.1 Results: Graphene/FM heterostructure

To develop a generic SOT theory, not reliant on spinful scattering centers [168, 169, 194, 202] we chose a simple scalar disorder potential:

$$U\,(\boldsymbol{x}) = u_0 \sum_{i=1} \delta\,(\boldsymbol{x} - \mathbf{X}_i)\,. \qquad (5.13)$$

We start with the simpler case of the C_{6v} invariant model in the presence of an FM induced exchange interaction ($\Delta = \lambda_{sv} = 0$). The exchange coupling in these samples can be up to the order of 10s of meV [94]. The results are summarised in Fig. 5.2a where it is shown the Fermi energy dependence of the relevant K^J terms. The familiar Rashba-Edelstein response (κ_{yx}) stands out with a high efficiency (~ 0.4 for $\epsilon_F = 0.4$ meV), comparable to what is found in topological insulators and graphene/TMD bilayers [91, 188]. Additionally, there is a significant generation of out-of-plane spin polarisation (κ_{zy}). Both of these responses are present even in the Gaussian limit making them inherently more robust. These terms make up the field-like SOT and are incapable of inducing magnetic switching by themselves. The T-Matrix approximation captures skewscattering, which is present in systems with $m_z \neq 0$ (see Fig. 5.1). This reveals two more contributions to the SOT. A collinear Edelstein effect (κ_{ii}), which establishes a spin polarisation along the same direction as the applied current, is present already in the isotropic model ($m_x = 0$). This is the main contribution towards the damping-like SOTs: t_{e1} and t_{e2}, which are desirable for magnetic switching based devices. Lastly, the in-plane magnetisation induces a small out-of-plane spin density response. Both these effects are present for moderate impurity potential strength and are finite as soon as skewscattering is activated. Interestingly, these terms are also present in the 2DEG, albeit much weaker, since they appear as higher order terms (in terms of potential strength) in the diagrammatic expansion [201].

Both skewscattering-activated responses (K^J_{xx} and K^J_{zx}) are highly sensi-
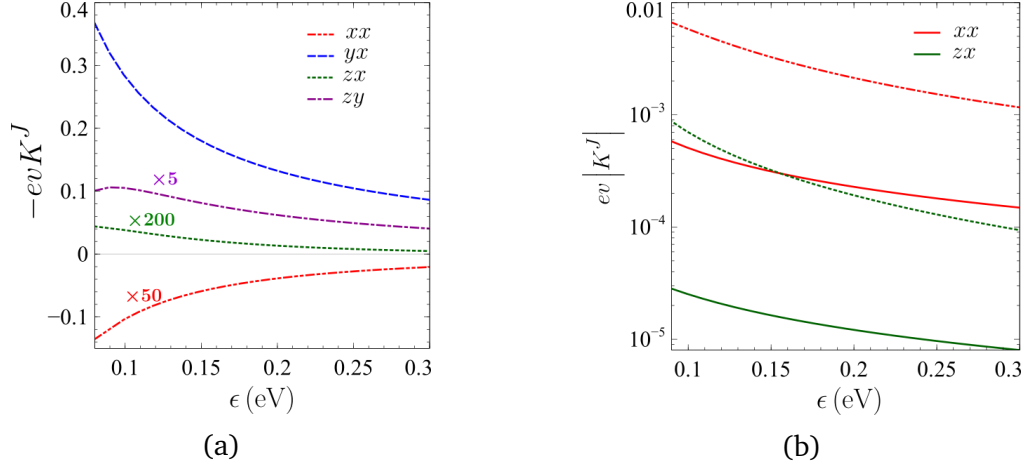
Figure 5.2: The current induced spin response in magnetised graphene, as a function of the Fermi energy, for $\alpha = 20$ meV, $\Delta_{xc} = 15$ meV, $\theta_m = \pi/11$, $n = 10^{11}$ cm^{-2}. (a) For an intermediate disorder potential $u_0 = 1.2$ eVnm^2, using the T-Matrix approximation, all responses are active, however the damping-like terms are very low, with efficiencies below 1%. (b) Comparison between the weak scattering limit, $u_0 = 0.1$ eVnm^2 (full lines) and the unitary limit $u_0 \to \infty$ (dashed lines) showing the increase in the SOT efficiencies $K_x^J x$ and $K_z^J x$ with the impurity potential due to their skewscattering origin.

tive to the scattering potential strength. While the Edelstein efficiency shows slow logarithmic disorder corrections [188], the damping-like efficiencies increase ten-fold when approaching the unitary limit ($u_0 \to \infty$), as shown in Fig. 5.2b. In systems where resonant scatterers (such as vacancies) are predominant the collinear Edelstein effect efficiency can get close to 1%.

It is possible to obtain approximate expressions for the torque coefficients in the weak scattering limit by treating the anisotropy perturbatively. We expand the GF in the anisotropy "parameter" m_x and insert it already at the level of Bethe-Salpeter equation for the vertex renormalisation. In this way the renormalised vertex acquires matrix structures dependent on m_x already containing information about which responses are activated. This is because once we insert the renormalised vertex into the final integral we automatically generate all diagrams to leading order in m_x. In the Gaussian approximation in particular, the matrix components of the renormalised vertex yield (apart from a multiplicative factor) the response. In this case we get a non-trivial structure for the self-energy Σ:

$$i\Sigma^R = \eta\mathbf{1} - \eta_x s_x - \eta_z s_z, \tag{5.14}$$

	$m_x = 0$	$\mathcal{O}\left(m_x\right)$
$\tilde{J}_x$	$\sigma_x s_0,\ \sigma_0 s_y,\ \sigma_x s_z,\ \sigma_z s_y$	$\sigma_x s_x,\ \sigma_y s_y$
$\tilde{J}_y$	$\sigma_y s_0,\ \sigma_0 s_x,\ \sigma_y s_z,\ \sigma_z s_x$	$\sigma_0 s_0,\ \sigma_z s_0,\ \sigma_0 s_z,\ \sigma_x s_y,\ \sigma_y s_x,\ \sigma_z s_z$

Table 5.1: The matrix structures generated upon disorder renormalisation of the charge current vertices, in the Gaussian approximation. Notice the presence of s_y in $\tilde{J}_x$ and of s_x and s_z in $\tilde{J}_y$.

with

$$\eta = nu_0^2 \frac{\epsilon}{4v^2}, \quad \eta_x = nu_0^2 \frac{\mathfrak{m}_x}{4v^2}, \quad \eta_z = nu_0^2 \frac{\mathfrak{m}_z}{4v^2}, \tag{5.15}$$

where we have have again defined $\mathfrak{m} = \Delta_{xc}m$ and neglected the real part of the self energy since it does not contribute to leading order terms. In Table 5.1 we show all the matrix structures of the charge current vertices generated by disorder renormalisation. The presence of s_x and s_y in, respectively, $\tilde{J}_y$ and $\tilde{J}_x$ is a manifestation of the Rashba-Edelstein effect. Additionally, the appearance of s_z in the former encodes the out-of-plane spin polarisation that is generated, at Gaussian level, by an electric field applied normal to the anisotropy direction.

The longitudinal conductivity is given by:

$$\sigma_{xx} = \sigma_{yy} = \sigma_0 \left(1 - \frac{4\alpha^2 \mathfrak{m}_z^2 \left(\epsilon^2 - 2\alpha^2\right)}{\epsilon^4 \left(\alpha^2 + \mathfrak{m}_z^2\right) - \mathfrak{m}_z^4 \left(\epsilon^2 - 3\alpha^2\right)} \right) \tag{5.16}$$

where $\sigma_0 = \epsilon/\eta$ is the conductivity of pure Dirac fermions. The longitudinal conductivity is lower when $\alpha, m_z \neq 0$ since backscattering is no longer completely suppressed. The Rashba-Edelstein response is, in turn:

$$K_{xy} = \frac{\sigma_0}{v} \frac{2\alpha^3 \epsilon \left(\epsilon^2 + \mathfrak{m}_z^2\right)}{\epsilon^4 \left(\alpha^2 + \mathfrak{m}_z^2\right) - \mathfrak{m}_z^4 \left(\epsilon^2 - 3\alpha^2\right)} = -K_{yx}, \tag{5.17}$$

and the out-of-plane spin polarisation response is:

$$K_{zy} = \frac{\sigma_0}{v} \frac{2\mathfrak{m}_x \mathfrak{m}_z \alpha}{\epsilon \left(\alpha^2 + \mathfrak{m}_z^2\right)} + \mathcal{O}\left(\epsilon^{-2}\right), \tag{5.18}$$

in the limit of high Fermi energy. These are the only responses that are captured by the widely used Gaussian approximation. It is necessary to go beyond it and include skewness to activate the remaining terms and, consequently, damping-like torque. In the weak scattering limit we do that by considering the "Y-diagrams" which are the next order diagrams in the impurity potential strength, shown in Fig. 5.3. Including these is also enough to
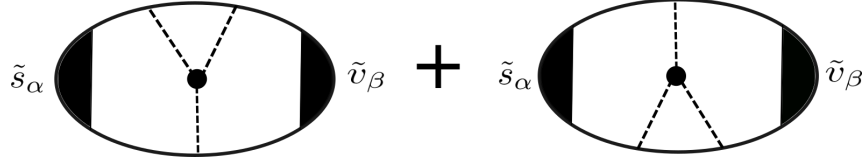
Figure 5.3: The Y diagrams are the the lowest order diagrams that capture skewscattering in the weak scattering limit. For these diagrams we need to renormalise both opeators involved.

capture the extrinsic contribution to the Hall response:

$$\sigma_{xy}^{\mathrm{Y}} = -\frac{2u_0 m_z \alpha^6 \left(\epsilon^2 + m_z^2\right)^3 \sigma_0}{v^2 \left(\epsilon^4 \left(\alpha^2 + m_z^2\right) - m_z^4 \left(\epsilon^2 - 3\alpha^2\right)\right)^2} = -\sigma_{yx}^{\mathrm{Y}}, \qquad (5.19)$$

as well as the newly unveiled collinear Edelstein effect:

$$K_{xx}^{\mathrm{Y}} = K_{yy}^{\mathrm{Y}} = \frac{u_0 \mathfrak{m}_z \alpha^5 \epsilon \left(\epsilon^2 - \mathfrak{m}_z^2\right) \left(\epsilon^2 + \mathfrak{m}_z^2\right)^2 \sigma_0}{v^3 \left[\epsilon^4 \left(\mathfrak{m}_z^2 + \alpha^2\right) - \mathfrak{m}_z^4 \left(\epsilon^2 - 3\alpha^2\right)\right]^2}, \qquad (5.20)$$

and another out-of-plane response

$$K_{zx}^{\mathrm{Y}} = -\sigma_0 \frac{u_0 \mathfrak{m}_x \mathfrak{m}_z^2 \alpha^5}{2v^3 \epsilon \left(\alpha^2 + \mathfrak{m}_z^2\right)^3} + \mathcal{O}\left(\epsilon^{-2}\right). \qquad (5.21)$$

Now every response is present and, more importantly, all of them scale linearly with the conductivity. This is a stark contrast to previous theoretical works where skewness was not taken into account. In such cases the damping-like torques appear as subleading terms (in the case of perturbative diagrammatic calculations [91, 203]) or weakly dependent on the transport time (in the case of first principle calculations [204, 205]). The coefficients of the torque ($t_{\mathrm{e(o)}i} \equiv d^{-1}\Delta_{xc}\tau_{\mathrm{e(o)}i}$) in this limit admit the following expressions:

$$\tau_{\mathrm{o}1} \simeq 2\alpha^3 / f_\epsilon, \qquad \tau_{\mathrm{o}2} \simeq 2\Delta_{xc}^2 \alpha / f_\epsilon, \qquad (5.22a)$$

$$\tau_{\mathrm{e}1} \simeq u_0 \Delta_{xc} \epsilon \, \alpha^5 / (v f_\epsilon^2), \quad \tau_{\mathrm{e}2} \simeq -\tau_{\mathrm{e}1}, \qquad (5.22b)$$

where $f_\epsilon = v\epsilon(\alpha^2 + \mathfrak{m}_z^2)$.

5.4.2 Results: TMDs/FM heterostructures

We now move on to systems with broken sublattice symmetry ($C_{6v} \rightarrow C_{3v}$) which spans a wide range of materials. We will study the case of a semiconductor TMD/FM heterostructure. These materials typically have sizable

orbital gaps $E_g = 2\Delta$ and an extra SOC known as spin-valley coupling λ_{sv}. Since this interaction is diagonal in the valley space we compute the response functions for each separate valley and then add them to get the final result. Furthermore, in these systems, α and Δ_{xc} can be much larger than the values seen in the graphene case [206–209]. In particular we shall explore the case where the exchange coupling is of the order of 100s of meV.

The presence of the additional energy scales make an analytical treatment extremely unpractical. Hence, we compute the Diffuson and Υ matrix numerically and bypass integrating the renormalised vertex via Eq.(2.28). The evolution of the SOTs with the orbital gap is depicted in Fig. 5.4. There are two main features here. First is the strong enhancement of the out-of-plane damping-like SOT efficiency K_{zx}^J relative to what was obtained before, due to a large out-of-plane equilibrium spin polarisation established by the orbital mass. Furthermore the collinear Edelstein effect is now highly anisotropic as $|\tau_{e1}| \neq |\tau_{e2}|$, a difference that increases with the orbital gap. This anisotropy is further illustrated in the inset of Fig. 5.4 which shows that even for a small magnetisation angle of $\pi/10$ there is already a 25% difference between the two. What's more, the fact that the angle dependence is so noticeable for small angles means that a non-perturbative treatment of the problem is necessary and one cannot make the approximation of taking the torquances $t_{e/o,i}$ to be constant in θ_m when solving the LLG equation.

The values obtained for the SOT terms are small (one order of magnitude smaller) when compared to typical experimental values [77–79]. This is a consequence of the fairly simplified model that was used (scalar, uncorrelated disorder) and the fact that we are considering the Rashba Hamiltonian as the only SOC contribution. These results however represent a large improvement over previous theories where damping-like SOT is only captured at next order $\mathcal{O}\left(n^0\right)$ in the impurity density [91], and, therefore, will contribute much less in diffusive samples. Furthermore, this theory is mainly aimed at providing an understanding about the microscopic mechanisms behind the generation of SOT in 2D materials.

5.5   Conclusions

In this chapter we have presented a microscopic theory for purely interfacial SOT, focusing in the Fermi sea response, which is dominant in the diffusive limit of disordered systems. Such a theory was sorely lacking and represents an important step away from the previous idea that, in the mono-
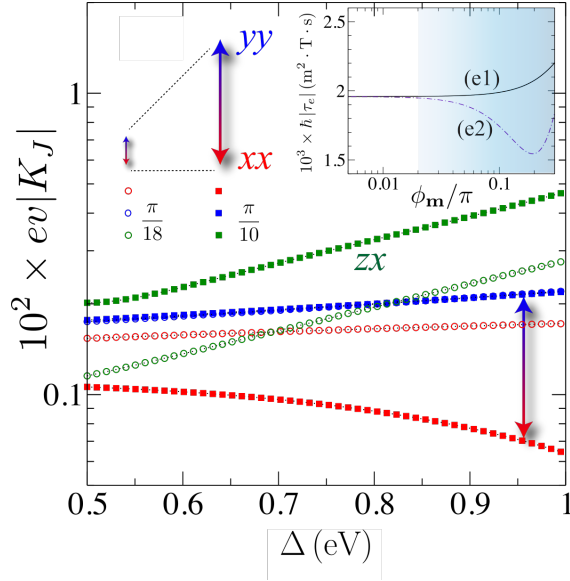
Figure 5.4: Orbital gap dependence of the damping-like SOT efficiencies generated in TMDs in the unitary limit, for a fixed carrier density of $n_e = 4.7 \times 10^{13}$cm^{-2}, $\Delta_{xc} = 0.1$eV, $\alpha = 60$meV, $\lambda_{sv} = 3$meV and impurity density $n = 10 \times 11$ cm^{-2}. The circle points are realizations for $\theta_m = \pi/18$ while the squares are $\theta_m = \pi/10$. There is a high degree of anisotropy between K_{xx}^J and K_{yy}^J that gets amplified for higher Δ. The inset depicts angle dependence of $\tau_{e1(2)}$. The shaded area indicates strong non-perturbative region where high-order harmonics τ_{en} ($n > 2$) become prominent.

layer limit, the Rashba SOC would induce a predominantly field-like response [90, 92, 210]. When skewscattering is taken into account, a robust damping-like response that scales linearly with the conductivity is activated. This enhancement of the damping-like SOT efficiency comes in tandem with two novel charge-to-spin conversion phenomena: the collinear Edelstein effect, wherein a spin polarisation is generated along the direction of the applied current ($S_i = K_{ii}\mathcal{E}_i$), and an out-plane spin polarisation response ($S_z = K_{zx}\mathcal{E}_x$) [211]. These findings dismiss the expectation that anti-damping SOT required the presence of bulk SHE [92] or intrinsic Berry phase-related mechanisms [212–214].

These results relied on a self consistent treatment of disorder that allows for a full resummation of single impurity diagrams (T-Matrix approach). It is the first instance this formalism is used in the context of SOTs. It allows study all impurity potential regimes from the weak (Gaussian) to the resonant (unitary) scattering limits non-perturbatively in all the couplings of the bare Hamiltonian, including randomly oriented magnetisation. This formalism can be easily used for other systems such as topological insulators and lower symmetry TMDs [201].

Chapter 6

Summary and Outlook

In this thesis we have studied 2D honeycomb lattice systems under the effects of strong proximity induced spin-orbit and exchange interactions in the presence different types of disorder potential landscapes. We employed a diagrammatic formalism that allows for a fully quantum and controlled treatment of the problem in the dilute impurity regime, non-perturbatively in the energy scales of the Hamiltonian.

We first analysed C_{6v}-invariant focusing on the quantum interference corrections to the conductivity and how they are affected by strong entanglement between the different DOFs: spin, pseudospin (sublattice) and isospin (valley). The analysis was heavily centered on the Cooperon structure, and understanding which types of states are dominant. By studying them on simple graphene, we found that for certain types of disorder the WL corrections are not dominated by a singlet state as is generally assumed, and is the basis for most of the approximations used ([143, 151–153, 182]). The presence of strong SOC in graphene significantly alters the Cooperon modes, as they are no longer well described by spin-pseudospin product states. Furthermore, the SOC makes the weight matrix non-diagonal leading to the mixing of different Cooperon states. This feature is missed if we take the commonly taken approximation of a diagonal weight matrix. Finally, we found a new weak localisation phase that is driven by the spin-orbit interaction, a contrasting picture to what happens in conventional conductors. This regime required the development of a non-perturbative treatment in the Cooperon momentum to accurately capture the low energy behaviour of the Cooperon states. The observation of this WL phase would require ultra clean samples,

since it is highly sensitive to intervalley scattering, which quickly changes the nature of the quantum interference, giving way to the conventional WAL phase. Moving forward on this topic, it would be interesting to apply this formalism to C_{3v}-invariant materials such as TMDs and analyse the quantum corrections in the different energy regimes and see if this non-perturbative treatment yields again new results compared to previous perturbative studies [152, 153]. Furthermore, while we have assumed throughout this work that the coherence length of electrons is much larger than the mean free path. This might not be true in some samples, in which case other diagrams, besides the maximally crossed become relevant [215]. It would be interesting to understand what role do these diagrams play in this case. And lastly, the inclusion of a magnetic field and the study of the magnetoconductivity would facilitate comparisons with experimental results.

In the second part of this thesis we applied the diagrammatic formalism to develop a general microscopic theory of spin-orbit torques in graphene and TMDs proximity coupled to a ferromagnetic material. This allows us to access a wide range of points of the Hamiltonian parameters phase space: weak and strong SOC, strong exchange, intermediate energy regimes, arbitrary direction of magnetisation and strong impurity potential strength. Furthermore, the T-Matrix formalism employed takes fully into account skewscattering. This proved to be crucial as it activates all possible spin density responses, including new charge-to-spin conversion phenomena, the collinear Edelstein effect and the generation of the out-of-plane spin polarisation, which are responsible for damping-like SOT. This comes to dispel the notion that one needs a complex impurity potential landscape (e.g. magnetic impurities) to get a damping-like SOT response in the 2D limit. The skewscattering nature of these responses makes them very sensitive to disorder potential strength getting greatly enhanced in the unitary limit. In TMDs, where the exchange interaction can be much larger, the in-plane mangetisation can lead to a highly anisotropic collinear Edelstein response as the higher harmonics terms become important. Moving forward we can use this formalism to study the SOT in topological insulators and the intrinsic response of the system.

Appendices

Appendix A

The Green's function in the magnetised Dirac Rashba model

We will compute the GF for the clean magnetised Dirac-Rashba system with an orbital mass term. The Hamiltonian describing this system is:

$$\mathcal{H}_{b,\mathbf{p}} = v\boldsymbol{\sigma} \cdot \mathbf{p} + \alpha \left(\sigma_x s_y - \sigma_y s_x \right) + \Delta \sigma_z + \mathfrak{m}_z s_z + \mathfrak{m}_x s_x, \qquad (A.1)$$

with the Pauli matrices σ_i, s_i, $i = 0, 1, 2, 3$ being the Pauli matrices acting, respectively on the sublattice and spin DOF, α is the Rashba SOC, Δ is the orbital mass term and $\mathfrak{m}_{x,z} = -\Delta_{xc} m_{x,z}$ the induced exchange term that couples the conduction electrons to the magnetisation $\mathbf{m}$ with strength Δ_{xc}. The clean system GF has the following structure:

$$G_{0,\mathbf{p}}^{R/A} = \frac{G_0^{\mathrm{p}} + G_0^{\theta}}{\left(v^2 \mathbf{p}^2 - z_1^2 \right)\left(v^2 \mathbf{p}^2 - z_2^2 \right)} + \mathfrak{m}_x \frac{G_x^{\mathrm{p}} + G_x^{\theta}}{\left(v^2 \mathbf{p}^2 - z_+^2 \right)^2 \left(v^2 \mathbf{p}^2 - z_-^2 \right)^2}, \qquad (A.2)$$

where we have expanded in the in-plane magnetisation and defined the terms:

$$z_\pm^2 = \epsilon^2 - \Delta^2 + \mathfrak{m}_z^2 \pm 2\sqrt{\epsilon^2 \left(\alpha^2 + \mathfrak{m}_z^2 \right) - \alpha^2 \left(\Delta + \mathfrak{m}_z \right)^2}, \qquad (A.3)$$

and the radial and angular parts:

$$G_0^{\mathrm{p}} = g_{00}^{\mathrm{p}} \gamma_{00} + g_{03}^{\mathrm{p}} \gamma_{03} + g_R^{\mathrm{p}} \gamma_R + g_{30}^{\mathrm{p}} \gamma_{30} + g_{33}^{\mathrm{p}} \gamma_{33}, \qquad (A.4)$$

$$\begin{aligned}
G_0^{\theta} =& 2v\mathbf{p}\alpha\epsilon \left(\gamma_{02} \cos\theta - \gamma_{01} \sin\theta \right) + 2v\mathbf{p}\epsilon\mathfrak{m}_z \left(\gamma_{13} \cos\theta + \gamma_{23} \sin\theta \right) + \\
& v\mathbf{p} \left(\epsilon^2 - v^2\mathbf{p}^2 - \Delta^2 + \mathfrak{m}_z^2 \right) \left(\gamma_{10} \cos\theta + \gamma_{20} \sin\theta \right) + \\
& v^2\mathbf{p}^2\alpha \left[\sin\left(2\theta \right) \left(\gamma_{22} - \gamma_{11} \right) + \cos\left(2\theta \right) \left(\gamma_{12} + \gamma_{21} \right) \right] + \\
& 2v\mathbf{p}\alpha \left(\Delta + \mathfrak{m}_z \right) \left(\gamma_{32} \cos\theta - \gamma_{31} \sin\theta \right),
\end{aligned} \qquad (A.5)$$

We have defined:

$$g_{00}^{\mathrm{p}} = \epsilon \left(\epsilon^2 - v^2 \mathrm{p}^2 - 2\alpha^2 - \Delta^2 - \mathfrak{m}_z^2 \right),$$

$$g_{03}^{\mathrm{p}} = \mathfrak{m}_z \left(\epsilon^2 + v^2 \mathrm{p}^2 - 2\alpha^2 + \Delta^2 \right) - \mathfrak{m}_z^3 - 2\alpha^2 \Delta,$$

$$g_R^{\mathrm{p}} = \alpha \left(\epsilon^2 - (\Delta + \mathfrak{m}_z)^2 \right), \tag{A.6}$$

$$g_{30}^{\mathrm{p}} = \Delta \mathfrak{m}_z^2 - 2\alpha^2 \mathfrak{m}_z + \Delta \left(\epsilon^2 - v^2 \mathrm{p}^2 - 2\alpha^2 - \Delta^2 \right),$$

$$g_{33} = -2\epsilon \left(\alpha^2 - \Delta \mathfrak{m}_z \right).$$

Finally the first order terms in m_x cumbersome expressions of the various energy scales. Spin-valley coupling can easily be included with the substitution $\mathfrak{m}_z \to \mathfrak{m}_z + \lambda_{sv}$ in the $\mathbf{K}$ valley and $\mathfrak{m}_z \to \mathfrak{m}_z - \lambda_{sv}$ and $\Delta \to -\Delta$ for the $\mathbf{K}'$ valley.

Appendix B

The Cooperon Hamiltonian

We write the Cooperon Hamiltonian $\mathcal{H}_C = 1 - \xi P$ using two particle pseudo-spin and spin operators: $\boldsymbol{\Sigma} = \left(\boldsymbol{\sigma}^1 + \boldsymbol{\sigma}^2\right)/2$, $\tilde{\boldsymbol{\Sigma}} = \left(\boldsymbol{\sigma}^1 - \boldsymbol{\sigma}^2\right)/2$ and $\boldsymbol{S} = \left(\boldsymbol{s}^1 + \boldsymbol{s}^2\right)/2$. The superscripts refer to the particles sub-spaces such that $\boldsymbol{\sigma}^1 = \left(\boldsymbol{\sigma} \otimes s_0\right) \otimes \mathbf{1}_4$.

In the absence of SOC and with scalar, Gaussian impurities we have:

$$
\begin{aligned}
\mathcal{H}_C^0 &= \frac{q^2}{8} + \frac{i}{4}\boldsymbol{Q} \cdot \tilde{\boldsymbol{\Sigma}} + \frac{i}{16}q_x q_y \Sigma_z + \frac{1}{16}\left(8 - q^2\right)\left(\Sigma_x^2 + \Sigma_y^2\right) + \\
&\quad + \frac{1}{16}\frac{q_x^2 - q_y^2}{2}\left(\Sigma_y^2 - \Sigma_x^2\right) - \frac{1}{8}q_x q_y \Sigma_x \Sigma_y,
\end{aligned}
\tag{B.1}
$$

where we have defined the dimensionless quantity $\boldsymbol{q} = v\mathbf{Q}/\eta$. Including the Rashba SOC rapidly increases the complexity of the problem. For weak SOC we get:

$$
\begin{aligned}
\mathcal{H}_C &= \mathcal{H}_C^0 + i\mathcal{C}_1\left(8 - 3q^2\right)\left(\tilde{\Sigma}_x S_y - \tilde{\Sigma}_y S_x\right) + \mathcal{C}_2\left(8 - q^2\right)\left(\Sigma_x S_y - \Sigma_y S_x\right) + \\
&\quad + 4\mathcal{C}_1\left(q_x S_y - q_y S_x\right) + \mathcal{C}_2\frac{Q_x^2 - q_y^2}{2}\left(\Sigma_x S_y + \Sigma_y S_x\right) \\
&\quad - i3\mathcal{C}_1\frac{q_x^2 - q_y^2}{2}\left(\tilde{\Sigma}_x S_y + \tilde{\Sigma}_y S_x\right) + i3\mathcal{C}_1 q_x q_y\left(\tilde{\Sigma}_x S_x - \tilde{\Sigma}_y S_y\right) \\
&\quad - \mathcal{C}_2 q_x q_y\left(\Sigma_x S_x - \Sigma_y S_y\right) + \\
&\quad + \left\{\mathcal{C}_1 q_x\left[S_x\left(\sigma_x^1\sigma_y^2 + \sigma_y^1\sigma_x^2\right) - S_y\left(\sigma_y^1\sigma_y^2 + 3\sigma_x^1\sigma_x^2\right)\right] - x \leftrightarrow y\right\}
\end{aligned}
\tag{B.2}
$$

The factors are given by $\mathcal{C}_1 = \frac{\alpha}{16\eta}$ and $\mathcal{C}_2 = \frac{\alpha}{16\epsilon}$, so we can neglect $\mathcal{C}_2$ for high Fermi energies.

Appendix C

Cooperon Modes with strong SOC

At zero momentum, the eigenvalues and eigenvectors of of the Cooperon Hamiltonian in the strong SOC case are as follows:

$$e_1 = 0, \qquad e_2 = \frac{\epsilon}{2(\epsilon + \alpha)}, \qquad e_3 = \frac{\epsilon^2 - 4\alpha^2}{2(\epsilon^2 - \alpha^2)},$$

$$e_4 = \frac{\epsilon}{2(\epsilon - \alpha)}, \qquad e_5 = \frac{3\epsilon^2 - 4\alpha^2}{4(\epsilon^2 - \alpha^2)}, \qquad e_6 = 1, \tag{C.1}$$

in ascending order. Their respective eigenstates are:

$$v_1 = ss, \qquad v_{2,a} = \frac{1}{\sqrt{2}}(st_2 + it_2 s), \qquad v_{2,b} = \frac{1}{\sqrt{2}}(st_1 - it_1 s),$$

$$v_3 = \frac{1}{\sqrt{2\left(1 + 4\frac{\alpha^2}{\epsilon^2}\right)}}\left(t_1 t_2 - t_2 t_1 - 2i\frac{\alpha}{\epsilon}t_3 t_3\right),$$

$$v_{4,a} = \frac{1}{\sqrt{2}}(st_2 - it_2 s), \qquad v_{4,b} = \frac{1}{\sqrt{2}}(st_1 + it_1 s),$$

$$v_{5,a} = t_1 t_1, \qquad v_{5_b} = t_2 t_2,$$

$$v_{6,a} = t_2 t_3, \qquad v_{6,b} = t_3 t_2,$$

$$v_{6,c} = \frac{1}{\sqrt{2}}(st_3 + t_3 s), \qquad v_{6_d} = \frac{1}{\sqrt{2}}(t_1 t_2 + t_2 t_1), \tag{C.2}$$

$$v_{6,e} = \frac{1}{\sqrt{2\left(1 + 4\frac{\alpha^2}{\epsilon^2}\right)}}\left(t_3 s + t_3 t_3 - 2i\frac{\alpha}{\epsilon}t_1 t_2\right),$$

$$v_{6,f} = \frac{1}{\sqrt{2\left(1 + 4\frac{\alpha^2}{\epsilon^2}\right)}}\left(st_3 + t_3 t_3 - 2i\frac{\alpha}{\epsilon}t_1 t_2\right),$$

$$v_{6,g} = t_3 t_1, \qquad v_{6,h} = t_1 t_3,$$

$$v_{6,i} = \frac{1}{\sqrt{2\left(1 + 4\frac{\alpha^2}{\epsilon^2}\right)}}\left(t_1 t_2 + t_2 t_1 - 2i\frac{\alpha}{\epsilon}t_3 t_3\right),$$

Appendix D

Transformation Matrices for $\mathcal{H}_C$ and W in the valley space

For conciseness we define the matrices $\Xi_{lmn}^{ijk} \equiv (\tau_i \sigma_j s_k) \otimes (\tau_l \sigma_m s_n)$ with the indices $i, j, k, l, m, n = 0, 1, 2, 3$ and the matrices τ_i σ_i and s_i being the Pauli matrices acting on isospin, pseudospin and spin DOFs. We use the following transformation to obtain the Cooperon Hamiltonian:

$$\mathcal{H}_C = \mathcal{S}^{-1}\tilde{\mathcal{H}}_C \mathcal{S}, \tag{D.1}$$

from a simplified form $\tilde{\mathcal{H}}_C = \mathbf{1}_4 \otimes \mathcal{H}_{C,1v}$ that directly uses the result for one valley only. The transformation matrix in given by:

$$\mathcal{S} = \frac{1}{4} \left(\Xi_{000}^{000} + \Xi_{000}^{011} + \Xi_{000}^{022} + \Xi_{000}^{033} + \Xi_{100}^{001} + \Xi_{200}^{002} + \Xi_{300}^{003} + \Xi_{100}^{010} - i\Xi_{300}^{012} + \right.$$
$$\left. + i\Xi_{200}^{013} + \Xi_{200}^{020} + i\Xi_{300}^{021} - i\Xi_{100}^{023} + \Xi_{300}^{030} - i\Xi_{200}^{031} + i\Xi_{100}^{032} \right). \tag{D.2}$$

Similarly for the weight matrix we have:

$$W = \mathcal{S}_L \left(\mathbf{1}_4 \otimes W_{1,v} \right) \mathcal{S}_R \tag{D.3}$$

with the following transformation matrices:

$$\mathcal{S}_L = \frac{1}{4} \left(\Xi_{000}^{000} + \Xi_{000}^{011} + \Xi_{000}^{022} + \Xi_{000}^{033} + \Xi_{100}^{001} + \Xi_{200}^{002} + \Xi_{300}^{003} + \Xi_{100}^{010} + i\Xi_{300}^{012} - \right.$$
$$\left. - i\Xi_{200}^{013} + \Xi_{200}^{020} - i\Xi_{300}^{021} + i\Xi_{100}^{023} + \Xi_{300}^{030} + i\Xi_{200}^{031} - i\Xi_{100}^{032} \right), \tag{D.4}$$

$$\mathcal{S}_R = \frac{1}{8} \left(\Xi^{011}_{000} + \Xi^{022}_{000} + \Xi^{033}_{000} + \Xi^{101}_{000} + \Xi^{110}_{000} - i\Xi^{123}_{000} + i\Xi^{132}_{000} + \Xi^{202}_{000} + \right.$$

$$+ i\Xi^{213}_{000} + \Xi^{220}_{000} - i\Xi^{231}_{000} + \Xi^{303}_{000} - i\Xi^{312}_{000} + i\Xi^{321}_{000} + \Xi^{330}_{000} + \Xi^{000}_{000} +$$

$$+ \Xi^{001}_{100} + \Xi^{002}_{200} + \Xi^{003}_{300} + \Xi^{010}_{100} - i\Xi^{012}_{300} + i\Xi^{013}_{200} + \Xi^{020}_{200} + i\Xi^{021}_{300} -$$

$$- i\Xi^{023}_{100} + \Xi^{030}_{300} - i\Xi^{031}_{200} + i\Xi^{032}_{100} + \Xi^{111}_{100} + \Xi^{122}_{100} + \Xi^{133}_{100} - i\Xi^{203}_{100} -$$

$$- \Xi^{212}_{100} + \Xi^{221}_{100} - i\Xi^{230}_{100} + i\Xi^{302}_{100} - \Xi^{313}_{100} + i\Xi^{320}_{100} + \Xi^{331}_{100} + \Xi^{100}_{100} -$$

$$- i\Xi^{102}_{300} + i\Xi^{103}_{200} + \Xi^{112}_{200} + \Xi^{113}_{300} - i\Xi^{120}_{300} - \Xi^{121}_{200} + i\Xi^{130}_{200} - \Xi^{131}_{300} +$$

$$+ \Xi^{211}_{200} + \Xi^{222}_{200} + \Xi^{233}_{200} - i\Xi^{301}_{200} - i\Xi^{310}_{200} - \Xi^{323}_{200} + \Xi^{332}_{200} + \Xi^{200}_{200} +$$

$$\left. + i\Xi^{201}_{300} + i\Xi^{210}_{300} + \Xi^{223}_{300} - \Xi^{232}_{300} + \Xi^{311}_{300} + \Xi^{322}_{300} + \Xi^{333}_{300} + \Xi^{300}_{300} \right).$$

Appendix E

Non-perturbative Expression for the Cooperon

In this section we provide a proof for a treatment of the Cooperon Hamiltonian non-perturbative in the momentum. The key quantity is the integral:

$$P\left(\boldsymbol{Q}\right) = \int \frac{\mathrm{d}\mathbf{p}}{\left(2\pi\right)^2}\, \mathcal{G}^R_{\boldsymbol{Q}-\mathbf{p}} \otimes \mathcal{G}^A_{\mathbf{p}}. \tag{E.1}$$

We shall restrict ourselves to the case where the self energy is scalar. If we represent the GF in terms of the projectors $\mathcal{P}^\lambda_s = |\lambda s\rangle \langle \lambda s|$, given in terms of the Hamiltonian eigenstates $|\lambda s\rangle$, (λ and s are band labels) it follows that:

$$P\left(\boldsymbol{Q}\right) = \sum_{ss'\lambda\lambda'} \int \frac{\mathrm{d}\mathbf{p}}{\left(2\pi\right)^2} \frac{\mathcal{P}^{\lambda'}_{s'}\left(\boldsymbol{Q}-\mathbf{p}\right)}{\epsilon - E^{\lambda'}_{s'}\left(\boldsymbol{Q}-\mathbf{p}\right)+i\eta} \otimes \frac{\mathcal{P}^{\lambda}_{s}\left(\mathbf{p}\right)}{\epsilon - E^{\lambda}_{s}\left(\mathbf{p}\right)-i\eta}. \tag{E.2}$$

Performing partial fraction decomposition:

$$P\left(\boldsymbol{Q}\right) = \sum_{ss'\lambda\lambda'} \int \frac{\mathrm{d}\mathbf{p}}{\left(2\pi\right)^2} \mathcal{L}\left(\mathbf{Q},\mathbf{p}\right) \left(\frac{P \otimes P}{\epsilon - E^{\lambda}_{s}\left(\mathbf{p}\right)-i\eta} - \frac{P \otimes P}{\epsilon - E^{\lambda'}_{s'}\left(\boldsymbol{Q}-\mathbf{p}\right)+i\eta} \right). \tag{E.3}$$

We have defined, for convenience $P \otimes P = \mathcal{P}^{\lambda'}_{s'}\left(\boldsymbol{Q}-\mathbf{p}\right) \otimes \mathcal{P}^{\lambda}_{s}\left(\mathbf{p}\right)$ and:

$$\mathcal{L}\left(\mathbf{Q},\mathbf{p}\right) = \frac{1}{E^{\lambda}_{s}\left(\mathbf{p}\right) - E^{\lambda'}_{s'}\left(\boldsymbol{Q}-\mathbf{p}\right)+2i\eta}. \tag{E.4}$$

Using the Sokhotski–Plemelj theorem:

$$P(\boldsymbol{Q}) = \sum_{ss'\lambda\lambda'} \int \frac{\mathrm{d}\mathbf{p}}{4\pi} \left(\frac{i\delta\left(\epsilon - E_s^\lambda(\mathbf{p})\right) P \otimes P}{E_s^\lambda(\mathbf{p}) - E_{s'}^{\lambda'}(\boldsymbol{Q} - \mathbf{p}) + 2i\eta} - \frac{i\delta\left(\epsilon - E_{s'}^{\lambda'}(\boldsymbol{Q} - \mathbf{p})\right) P \otimes P}{E_{s'}^{\lambda'}(\boldsymbol{Q} - \mathbf{p}) - E_s^\lambda(\mathbf{p}) - 2i\eta} \right),$$

(E.5)

where we have neglected the principal part of the integral since it contains higher order terms in the impurity concentration. Now, firstly, in the second term of Eq.(E.5) we make the change of variable $\boldsymbol{Q} - \mathbf{p} \to \mathbf{p}$, then we notice that, depending on the sign of the Fermi energy, either only the positive energy bands or the negative energy bands will contribute to each of the terms. From now on we assume a positive Fermi energy. In this case the sum is dominated by the positive energy bands due to the difference of energies in the denominator:

$$P(\boldsymbol{Q}) \approx \sum_{ss'} \int \frac{\mathrm{d}\theta}{4\pi} i \left[\frac{\rho(\epsilon)\,\mathcal{P}_{s'}^+(\boldsymbol{Q} - \mathbf{p}_F) \otimes \mathcal{P}_s^+(\mathbf{p}_F)}{E_s^+(\mathbf{p}_F) - E_{s'}^+(\boldsymbol{Q} - \mathbf{p}_F) + 2i\eta} - \frac{\rho(\epsilon)\,\mathcal{P}_{s'}^+(\mathbf{p}_F) \otimes \mathcal{P}_s^+(\boldsymbol{Q} - \mathbf{p}_F)}{E_{s'}^+(\mathbf{p}_F) - E_s^+(\boldsymbol{Q} - \mathbf{p}_F) - 2i\eta} \right].$$

(E.6)

We have defined the density of states $\rho(\epsilon) = |\mathrm{p}|\,\mathrm{dp}/\mathrm{d}\epsilon$ and assumed it is the same for all bands, and the same for the Fermi momentum $\mathbf{p}_F$ [1]. If the Fermi energy were negative instead we would have:

$$P(\mathbf{p}) \approx \sum_{ss'} \int \frac{\mathrm{d}\theta}{4\pi} i \left[\frac{\rho(\epsilon)\,\mathcal{P}_{s'}^-(\boldsymbol{Q} - \mathbf{p}_F) \otimes \mathcal{P}_s^-(\mathbf{p}_F)}{E_s^-(\mathbf{p}_F) - E_{s'}^-(\boldsymbol{Q} - \mathbf{p}_F) + 2i\eta} - \frac{\rho(\epsilon)\,\mathcal{P}_{s'}^-(\mathbf{p}_F) \otimes \mathcal{P}_s^-(\boldsymbol{Q} - \mathbf{p}_F)}{E_{s'}^-(\mathbf{p}_F) - E_s^-(\boldsymbol{Q} - \mathbf{p}_F) - 2i\eta} \right].$$

(E.8)

Upon relabeling $s \leftrightarrow s'$, we notice that Eqs.(E.6) and (E.8) are very similar. The difference comes from the angular integration of the projectors and is

---

[1]In the case of graphene with Rashba SOC there are two different density of states, one for each band ρ_+ and ρ_-. So we can define $\rho = (\rho_+ + \rho_-)/2$. The error of this approximation is given by

$$\delta\rho = \frac{\rho_+ - \rho_-}{\rho_+ + \rho_-} = \frac{\sqrt{\epsilon(\epsilon + 2\alpha) + \alpha^2} - \sqrt{\epsilon(\epsilon - 2\alpha) + \alpha^2}}{\sqrt{\epsilon(\epsilon + 2\alpha) + \alpha^2} + \sqrt{\epsilon(\epsilon - 2\alpha) + \alpha^2}} = \frac{\alpha}{\epsilon},$$

(E.7)

for large Fermi energies, for each band.

zero when $\boldsymbol{Q} = 0$:

$$\int d\theta \, \mathcal{P}_s^- \left(-\mathbf{p}_F\right) \otimes \mathcal{P}_{s'}^- \left(\mathbf{p}_F\right) = \int d\theta \, \mathcal{P}_{s'}^+ \left(\mathbf{p}_F\right) \otimes \mathcal{P}_s^+ \left(-\mathbf{p}_F\right) \qquad \text{(E.9)}$$

For finite $\boldsymbol{Q}$ this relation no longer holds and introduces and error $\sim \mathcal{O}\left(Q/\mathrm{p}_F\right)$. We now want to extend the range of integration of energy to the whole space $]-\infty, +\infty[$. For the positive bands this is allowed but the other half will now pick up a finite contribution that was not there before. We acount for this with a factor of $1/2$, which is justified as long as $Q/\mathrm{p}_F \ll 1$. Plus we can also include the interband terms that mix positive and negative energies, also allowed in the limit of large Fermi energy. Plugging the Hamiltonians back yields:

$$P\left(\boldsymbol{Q}\right) \approx \int \frac{d\theta}{8\pi} \left[\frac{i\rho\left(\epsilon\right)}{\mathcal{H}^2\left(\mathbf{p}_F\right) - \mathcal{H}^1\left(\boldsymbol{Q} - \mathbf{p}_F\right) + 2i\eta} - \frac{i\rho\left(\epsilon\right)}{\mathcal{H}^1\left(\mathbf{p}_F\right) - \mathcal{H}^2\left(\boldsymbol{Q} - \mathbf{p}_F\right) - 2i\eta} \right], \qquad \text{(E.10)}$$

where the superscripts refer to which particle subspace the Hamiltonians are acting on. Eq.(E.10) provides an alternative way to compute the Cooperon that is valid even when $v\boldsymbol{Q}$ is is comparable to the disorder broadening $vQ \sim \eta$ as long as the spin splitting of the bands due to SOC is small relative to the Fermi level. It is a more general version of other expressions that are used for the 2DEG [182].

Appendix F

Symmetries of the Magnetised Dirac-Rashba Model

Defining the following transformations:

$$S_1 \equiv \{\mathfrak{m}_z \to -\mathfrak{m}_z, \lambda_{sv} \to -\lambda_{sv}, \Delta \to -\Delta\}, \tag{F.1a}$$

$$S_2 \equiv \{\mathfrak{m} \to -\mathfrak{m}, \lambda_{sv} \to -\lambda_{sv}, \Delta \to -\Delta\}, \tag{F.1b}$$

$$S_3 \equiv \{\mathfrak{m}_x \to -\mathfrak{m}_x\} \tag{F.1c}$$

The disorder-averaged Green's functions for the Hamiltonian (3.22) satisfy the following symmetry relations:

$$s_x \sigma_y \mathcal{G}^a(-p_x, p_y)\sigma_y s_x = \mathcal{G}^a(p_x, p_y)\big|_{S_1}, \tag{F.2a}$$

$$s_y \sigma_x \mathcal{G}^a(p_x, -p_y)s_y\sigma_x = \mathcal{G}^a(p_x, p_y)\big|_{S_2}, \tag{F.2b}$$

$$s_z \sigma_z \mathcal{G}^a(-p_x, -p_y)s_z\sigma_z = \mathcal{G}^a(p_x, p_y)\big|_{S_3}. \tag{F.2c}$$

Using these symmetries in Eq.(5.3), we easily find:

$$K_{xx(yy)} = -\left.K_{xx(yy)}\right|_{S_1}, \;\; K_{xx(yy)} = -\left.K_{xx(yy)}\right|_{S_2}, \;\; K_{xx(yy)} = \left.K_{xx(yy)}\right|_{S_3}, \tag{F.3a}$$

$$K_{xy(yx)} = \left.K_{xy(yx)}\right|_{S_1}, \;\; K_{xy(yx)} = \left.K_{xy(yx)}\right|_{S_2}, \;\; K_{xy(yx)} = \left.K_{xy(yx)}\right|_{S_3}, \tag{F.3b}$$

$$K_{zx} = \left.K_{zx}\right|_{S_1}, \;\; K_{zx} = -\left.K_{zx}\right|_{S_2}, \;\; K_{zx} = -\left.K_{zx}\right|_{S_3}, \tag{F.3c}$$

$$K_{zy} = -\left.K_{zy}\right|_{S_1}, \;\; K_{zy} = \left.K_{zy}\right|_{S_2}, \;\; K_{zy} = -\left.K_{zy}\right|_{S_3}. \tag{F.3d}$$

These relations imply the structure of the response function presented in Eq.(5.6) of the main text.

Glossary

2D Two dimensional.

2DEG Two dimensional electron gas.

DOF Degree of freedom.

FM Ferromagnet.

FMR Ferromagnetic resonance.

GF Green's function.

GMR Giant magnetoresistance.

hBN Hexagonal Boron Nitride.

HM Heavy metal.

ISGE Inverse spin galvanic effect.

ISHE Inverse spin Hall effect.

LLG Landau-Lifshitz-Gilbert.

MRAM Magnetoresistive random access memory.

MTJ Magnetic tunnel junction.

REE Rashba-Edelstein effect.

SGE Spin galvanic effect.

SHE Spin Hall effect.

SLTA Spin lifetime anisotropy.

SOC Spin-orbit coupling.

SOT Spin-orbit torque.

STT Spin transfer torque.

TI Topological insulator.

TMD Transition metal dichalcogenide.

vdW van der Waals.

WAL Weak anti-localisation.

WL Weak localisation.

References

[1]K. S. Novoselov, A. K. Geim, S. V. Morozov, D. Jiang, Y. Zhang, S. V. Dubonos, I. V. Grigorieva, and A. A. Firsov, "Electric field effect in atomically thin carbon films", Science **306**, 666–669 (2004).

[2]M. D. Stoller, S. Park, Y. Zhu, J. An, and R. S. Ruoff, "Graphene-based ultracapacitors", Nano Letters **8**, 3498–3502 (2008).

[3]D. Cohen-Tanugi and J. C. Grossman, "Water desalination across nanoporous graphene", Nano Letters **12**, 3602–3608 (2012).

[4]M. A. Rafiee, J. Rafiee, Z. Wang, H. Song, Z.-Z. Yu, and N. Koratkar, "Enhanced mechanical properties of nanocomposites at low graphene content", ACS Nano **3**, 3884–3890 (2009).

[5]A. H. Castro Neto, F. Guinea, N. M. R. Peres, K. S. Novoselov, and A. K. Geim, "The electronic properties of graphene", Rev. Mod. Phys. **81**, 109–162 (2009).

[6]M. I. Katsnelson, K. S. Novoselov, and A. K. Geim, "Chiral tunnelling and the Klein paradox in graphene", Nature Physics **2**, 620–625 (2006).

[7]P. Young A. F. Kim, "Quantum interference and Klein tunnelling in graphene heterojunctions", Nature Physics **5**, 222–226 (2009).

[8]S. Das Sarma, E. H. Hwang, and W.-K. Tse, "Many-body interaction effects in doped and undoped graphene: fermi liquid versus non-fermi liquid", Phys. Rev. B **75**, 121406 (2007).

[9]Y. Zhang, Y.-W. Tan, H. L. Stormer, and P. Kim, "Experimental observation of the quantum hall effect and Berry's phase in graphene", Nature **438**, 201–204 (2005).

[10]V. P. Gusynin and S. G. Sharapov, "Unconventional integer quantum hall effect in graphene", Phys. Rev. Lett. **95**, 146801 (2005).

[11]K. S. Novoselov, D. Jiang, F. Schedin, T. J. Booth, V. V. Khotkevich, S. V. Morozov, and A. K. Geim, "Two-dimensional atomic crystals", Proceedings of the National Academy of Sciences **102**, 10451–10453 (2005).

[12]K. Zhang, Y. Feng, F. Wang, Z. Yang, and J. Wang, "Two dimensional hexagonal boron nitride (2D-hBn): synthesis, properties and applications", J. Mater. Chem. C **5**, 11992–12022 (2017).

[13]X. Wang, J. Lin, Y. Zhu, C. Luo, K. Suenaga, C. Cai, and L. Xie, "Chemical vapor deposition of trigonal prismatic NbS_2 monolayers and 3R-polytype few-layers", Nanoscale **9**, 16607–16611 (2017).

[14]A. Yan, J. Velasco, S. Kahn, K. Watanabe, T. Taniguchi, F. Wang, M. F. Crommie, and A. Zettl, "Direct growth of single- and few-layer MoS_2 on h-BN with preferred relative rotation angles", Nano Letters **15**, 6324–6331 (2015).

[15]M. Okada, T. Sawazaki, K. Watanabe, T. Taniguch, H. Hibino, H. Shinohara, and R. Kitaura, "Direct chemical vapor deposition growth of WS_2 atomic layers on hexagonal boron nitride", ACS Nano **8**, 8273–8277 (2014).

[16]M. Xu, T. Liang, M. Shi, and H. Chen, "Graphene-like two-dimensional materials", Chemical Reviews **113**, 3766–3798 (2013).

[17]A. Ayari, E. Cobas, O. Ogundadegbe, and M. S. Fuhrer, "Realization and electrical characterization of ultrathin crystals of layered transition-metal dichalcogenides", Journal of Applied Physics **101**, 014507 (2007).

[18]J. N. Coleman, M. Lotya, A. O'Neill, S. D. Bergin, P. J. King, U. Khan, K. Young, A. Gaucher, S. De, R. J. Smith, I. V. Shvets, S. K. Arora, G. Stanton, H.-Y. Kim, K. Lee, G. T. Kim, G. S. Duesberg, T. Hallam, J. J. Boland, J. J. Wang, J. F. Donegan, J. C. Grunlan, G. Moriarty, A. Shmeliov, R. J. Nicholls, J. M. Perkins, E. M. Grieveson, K. Theuwissen, D. W. McComb, P. D. Nellist, and V. Nicolosi, "Two-dimensional nanosheets produced by liquid exfoliation of layered materials", Science **331**, 568–571 (2011).

[19]Y. Shi, H. Li, and L.-J. Li, "Recent advances in controlled synthesis of two-dimensional transition metal dichalcogenides via vapour deposition techniques", Chem. Soc. Rev. **44**, 2744–2756 (2015).

[20]J. Yu, X. Hu, H. Li, X. Zhou, and T. Zhai, "Large-scale synthesis of 2D metal dichalcogenides", J. Mater. Chem. C **6**, 4627–4640 (2018).

[21]S. Bae, H. Kim, Y. Lee, X. Xu, J.-S. Park, Y. Zheng, J. Balakrishnan, T. Lei, H. Ri Kim, Y. I. Song, Y.-J. Kim, K. S. Kim, B. Özyilmaz, J.-H. Ahn, B. H. Hong, and S. Iijima, "Roll-to-roll production of 30-inch graphene films for transparent electrodes", Nature Nanotechnology **5**, 574 –578 (2010).

[22]B. Fu, Y. Ge, W. Su, W. Guo, and C.-C. Liu, "A new kind of 2D topological insulators BiCN with a giant gap and its substrate effects", Scientific Reports **6** (2016).

[23]S. Wu, V. Fatemi, Q. D. Gibson, K. Watanabe, T. Taniguchi, R. J. Cava, and P. Jarillo-Herrero, "Observation of the quantum spin hall effect up to 100 kelvin in a monolayer crystal", Science **359**, 76–79 (2018).

[24]Y. Shi, J. Kahn, B. Niu, Z. Fei, B. Sun, X. Cai, B. A. Francisco, D. Wu, Z.-X. Shen, X. Xu, D. H. Cobden, and Y.-T. Cui, "Imaging quantum spin hall edges in monolayer WTe_2", Science Advances **5** (2019).

[25]C. Gong and et al., "Discovery of intrinsic ferromagnetism in two-dimensional van der waals crystals", Nature **546**, 265 (2017).

[26]B. Huang and et al., "Layer-dependent ferromagnetism in a van der waals crystal down to the monolayer limit", Nature **546**, 270 (2017).

[27]G. Moore, "Cramming more components onto integrated circuits", Electronics **38** (1965).

[28]E. Sperling, "Quantum effects at 7/5nm and beyond", Semiconductor Engineering (2018).

[29]P. M. Tedrow and R. Meservey, "Spin polarization of electrons tunneling from films of Fe, Co, Ni, and Gd", Phys. Rev. B **7**, 318–326 (1973).

[30]M. Johnson and R. H. Silsbee, "Interfacial charge-spin coupling: injection and detection of spin magnetization in metals", Phys. Rev. Lett. **55**, 1790–1793 (1985).

[31]M. N. Baibich, J. M. Broto, A. Fert, F. N. Van Dau, F. Petroff, P. Etienne, G. Creuzet, A. Friederich, and J. Chazelas, "Giant magnetoresistance of (001)Fe/(001)Cr magnetic superlattices", Phys. Rev. Lett. **61**, 2472–2475 (1988).

[32]G. Binasch, P. Grünberg, F. Saurenbach, and W. Zinn, "Enhanced magnetoresistance in layered magnetic structures with antiferromagnetic interlayer exchange", Phys. Rev. B **39**, 4828–4830 (1989).

[33]J. Sinova, S. O. Valenzuela, J. Wunderlich, C. H. Back, and T. Jungwirth, "Spin hall effects", Rev. Mod. Phys. **87**, 1213–1260 (2015).

[34]M. Dyakonov and V. Perel, "Possibility of orientating electrons spins with current", Sov. Phys. JETP Let. **13** (1971).

[35]J. E. Hirsch, "Spin hall effect", Phys. Rev. Lett. **83**, 1834–1837 (1999).

[36]N. Mott, "The scattering of fast electrons by atomic nuclei", Proc. R. Soc. Lond. A **124**, 425–442 (1929).

[37]Y. K. Kato, R. C. Myers, A. C. Gossard, and D. D. Awschalom, "Observation of the spin Hall effect in semiconductors", Science **306**, 1910–1913 (2004).

[38]J. Wunderlich, B. Kaestner, J. Sinova, and T. Jungwirth, "Experimental observation of the spin-Hall effect in a two-dimensional spin-orbit coupled semiconductor system", Phys. Rev. Lett. **94**, 047204 (2005).

[39]E. Saitoh, M. Ueda, H. Miyajima, and G. Tatara, "Conversion of spin current into charge current at room temperature: inverse spin-Hall effect", Applied Physics Letters **88**, 182509 (2006).

[40]S. O. Valenzuela and M. Tinkham, "Direct electronic measurement of the spin Hall effect", Nature **442**, 176–179 (2006).

[41]K. Ando, S. Takahashi, J. Ieda, Y. Kajiwara, H. Nakayama, T. Yoshino, K. Harii, Y. Fujikawa, M. Matsuo, S. Maekawa, and E. Saitoh, "Inverse spin-Hall effect induced by spin pumping in metallic system", Journal of Applied Physics **109**, 103913 (2011).

[42]A. Bychkov and E. I. Rashba, "Properties of a 2D electron gas with lifted spectral degeneracy", JETP Lett. **39** (1984).

[43]E. L. Ivchenko, Y. B. Lyanda-Geller, and G. E. Pikus, "Photocurrent in structures in quantum wells with an optical orientation of free carriers", JETP Lett. **50** (1989).

[44]A. Aronov and Y. B. Lyanda-Geller, "Nuclear electric resonance and orientation of carrier spins by an electric field", JETP Lett. **50** (1989).

[45]V. M. Edelstein, "Spin polarization of conduction electrons induced by electric current in two-dimensional asymmetric electron systems", Solid State Communications **73** (1990).

⁴⁶J.-i. Inoue, G. E. W. Bauer, and L. W. Molenkamp, "Diffuse transport and spin accumulation in a Rashba two-dimensional electron gas", Phys. Rev. B **67**, 033104 (2003).

⁴⁷S. D. Ganichev, E. L. Ivchenko, V. V. Bel'kov, S. A. Tarasenko, M. Sollinger, D. Weiss, W. Wegscheider, and W. Prettl, "Spin-galvanic effect", Nature **417**, 153–156 (2002).

⁴⁸Y. K. Kato, R. C. Myers, A. C. Gossard, and D. D. Awschalom, "Current-induced spin polarization in strained semiconductors", Phys. Rev. Lett. **93**, 176601 (2004).

⁴⁹J. C. R. Sánchez, L. Vila, G. Desfonds, S. Gambarelli, J. P. Attané, J. M. De Teresa, C. Magén, and A. Fert, "Spin-to-charge conversion using Rashba coupling at the interface between non-magnetic materials", Nature Communications **4** (2013).

⁵⁰G. Dresselhaus, "Spin-orbit coupling effects in zinc blende structures", Phys. Rev. **100**, 580–586 (1955).

⁵¹S. Ringer, S. Hartl, M. Rosenauer, T. Völkl, M. Kadur, F. Hopperdietzel, D. Weiss, and J. Eroms, "Measuring anisotropic spin relaxation in graphene", Phys. Rev. B **97**, 205439 (2018).

⁵²T. S. Ghiasi, A. A. Kaverzin, P. J. Blah, and B. J. van Wees, "Charge-to-spin conversion by the Rashba–Edelstein effect in two-dimensional van der Waals heterostructures up to room temperature", Nano Letters **19**, 5959–5966 (2019).

⁵³C. K. Safeer, J. Ingla-Aynés, F. Herling, J. H. Garcia, M. Vila, N. Ontoso, M. R. Calvo, S. Roche, L. E. Hueso, and F. Casanova, "Room-temperature spin hall effect in graphene/MoS$_2$ van der Waals heterostructures", Nano Letters **19**, 1074–1082 (2019).

⁵⁴L. Li, J. Zhang, G. Myeong, W. Shin, H. Lim, B. Kim, S. Kim, T. Jin, S. Cavill, B. S. Kim, C. Kim, J. Lischner, A. Ferreira, and S. Cho, "Gate-tunable reversible rashba–edelstein effect in a few-layer graphene/2H-TaS$_2$ heterostructure at room temperature", ACS Nano **14**, 5251–5259 (2020).

⁵⁵S. A. Cavill, C. Huang, M. Offidani, Y.-H. Lin, M. A. Cazalilla, and A. Ferreira, "Proposal for unambiguous electrical detection of spin-charge conversion in lateral spin valves", Phys. Rev. Lett. **124**, 236803 (2020).

[56] T. S. Ghiasi, J. Ingla-Aynés, A. A. Kaverzin, and B. J. van Wees, "Large proximity-induced spin lifetime anisotropy in transition-metal dichalcogenide/graphene heterostructures", Nano Letters **17**, 7528–7532 (2017).

[57] L. A. Benítez, J. F. Sierra, W. Savero Torres, A. Arrighi, F. Bonell, M. V. Costache, and S. O. Valenzuela, "Strongly anisotropic spin relaxation in graphene–transition metal dichalcogenide heterostructures at room temperature", Nature Physics **14**, 303–308 (2018).

[58] S. Datta and B. Das, "Electronic analog of the electro-optic modulator", Appl. Phys. Lett. **56**, 665–667 (1990).

[59] S. Sugahara and J. Nitta, "Spin-transistor electronics: an overview and outlook", Proceedings of the IEEE **98**, 2124 –2154 (2010).

[60] M. Julliere, "Tunneling between ferromagnetic films", Physics Letters A **54**, 225 –226 (1975).

[61] J. S. Moodera, L. R. Kinder, T. M. Wong, and R. Meservey, "Large magnetoresistance at room temperature in ferromagnetic thin film tunnel junctions", Phys. Rev. Lett. **74**, 3273–3276 (1995).

[62] S. Yuasa, T. Nagahama, A. Fukushima, Y. Suzuki, and K. Ando, "Giant room-temperature magnetoresistance in single-crystal Fe/MgO/Fe magnetic tunnel junctions", Nature Materials **3**, 868 –871 (2004).

[63] J. Slonczewski, "Current-driven excitation of magnetic multilayers", J. Magn. Magn. Mater. **159** (1996).

[64] L. Berger, "Emission of spin waves by a magnetic multilayer traversed by a current", Phys. Rev. B **54**, 9353–9358 (1996).

[65] A. Brataas, A. D. Kent, and H. Ohno, "Current-induced torques in magnetic materials", Nature Materials **11** (2012).

[66] Y. Tserkovnyak and M. Mecklenburg, "Electron transport driven by nonequilibrium magnetic textures", Phys. Rev. B **77**, 134407 (2008).

[67] R. Urban, G. Woltersdorf, and B. Heinrich, "Gilbert damping in single and multilayer ultrathin films: role of interfaces in nonlocal spin dynamics", Phys. Rev. Lett. **87**, 217204 (2001).

[68] B. Heinrich, Y. Tserkovnyak, G. Woltersdorf, A. Brataas, R. Urban, and G. E. W. Bauer, "Dynamic exchange coupling in magnetic bilayers", Phys. Rev. Lett. **90**, 187601 (2003).

[69] L. Liu, C.-F. Pai, Y. Li, H. W. Tseng, D. C. Ralph, and R. A. Buhrman, "Spin-torque switching with the giant spin hall effect of tantalum", Science **336**, 555–558 (2012).

[70] I. Mihai Miron, G. Gaudin, S. Auffret, B. Rodmacq, A. Schuhl, S. Pizzini, J. Vogel, and P. Gambardella, "Current-driven spin torque induced by the Rashba effect in a ferromagnetic metal layer", Nature Materials **9**, 230–234 (2010).

[71] I. M. Miron and et al., "Perpendicular switching of a single ferromagnetic layer induced by in-plane current injection", Nature **476** (2011).

[72] R. Ramaswamy, J. M. Lee, K. Cai, and H. Yang, "Recent advances in spin-orbit torques: Moving towards device applications", Applied Physics Reviews **5**, 031107 (2018).

[73] L. Liu, T. Moriyama, D. C. Ralph, and R. A. Buhrman, "Spin-torque ferromagnetic resonance induced by the spin hall effect", Phys. Rev. Lett. **106**, 036601 (2011).

[74] C.-F. Pai, L. Liu, Y. Li, H. W. Tseng, D. C. Ralph, and R. A. Buhrman, "Spin transfer torque devices utilizing the giant spin hall effect of tungsten", Applied Physics Letters **101**, 122404 (2012).

[75] A. R. Mellnik, J. S. Lee, A. Richardella, J. L. Grab, P. J. Mintun, M. H. Fischer, A. Vaezi, A. Manchon, E.-A. Kim, N. Samarth, and D. C. Ralph, "Spin-transfer torque generated by a topological insulator", Nature **511**, 449–451 (2014).

[76] Y. Fan, P. Upadhyaya, X. Kou, M. Lang, S. Takei, Z. Wang, J. Tang, L. He, L.-T. Chang, M. Montazeri, G. Yu, W. Jiang, T. Nie, R. N. Schwartz, Y. Tserkovnyak, and K. L. Wang, "Magnetization switching through giant spin–orbit torque in a magnetically doped topological insulator heterostructure", Nature Materials **13**, 699–704 (2014).

[77] Q. Shao, G. Yu, Y.-W. Lan, Y. Shi, M.-Y. Li, C. Zheng, X. Zhu, L.-J. Li, P. K. Amiri, and K. L. Wang, "Strong rashba-edelstein effect-induced spin–orbit torques in monolayer transition metal dichalcogenide/ferromagnet bilayers", Nano Letters **16**, 7514–7520 (2016).

[78] M. D. and et al., "Control of spin-orbit torques through crystal symmetry in WTe$_2$ ferromagnet bilayers", Nature Phys. **13**, 300 (2017).

[79] M. H. D. Guimarães, G. M. Stiehl, D. MacNeill, N. D. Reynolds, and D. C. Ralph, "Spin–orbit torques in NbSe2/permalloy bilayers", Nano Letters **18**, 1311–1316 (2018).

[80] S. Shi and et al., "All-electric magnetization switching and Dzyaloshinskii-Moriya interaction in WTe_2-ferromagnet heterostructures", Nat. Nanotech. **14**, 945 (2019).

[81] W. Lv, Z. Jia, B. Wang, Y. Lu, X. Luo, B. Zhang, Z. Zeng, and Z. Liu, "Electric-field control of spin–orbit torques in WS_2/permalloy bilayers", ACS Applied Materials & Interfaces **10**, 2843–2849 (2018).

[82] D. Fang, H. Kurebayashi, J. Wunderlich, K. Výborný, L. P. Zârbo, R. P. Campion, A. Casiraghi, B. L. Gallagher, T. Jungwirth, and A. J. Ferguson, "Spin–orbit-driven ferromagnetic resonance", Nature Nanotechnology **6**, 413–417 (2011).

[83] K. Garello, I. M. Miron, C. O. Avci, F. Freimuth, Y. Mokrousov, S. Blügel, S. Auffret, O. Boulle, G. Gaudin, and P. Gambardella, "Symmetry and magnitude of spin–orbit torques in ferromagnetic heterostructures", Nature Nanotechnology **8**, 587–593 (2013).

[84] M. Hayashi, J. Kim, M. Yamanouchi, and H. Ohno, "Quantitative characterization of the spin-orbit torque using harmonic hall voltage measurements", Phys. Rev. B **89**, 144425 (2014).

[85] U. H. Pi, K. Won Kim, J. Y. Bae, S. C. Lee, Y. J. Cho, K. S. Kim, and S. Seo, "Tilting of the spin orientation induced by Rashba effect in ferromagnetic metal layer", Applied Physics Letters **97**, 162507 (2010).

[86] A. Ghosh, K. Garello, C. O. Avci, M. Gabureac, and P. Gambardella, "Interface-enhanced spin-orbit torques and current-induced magnetization switching of $Pd/Co/Al/O_x$ layers", Phys. Rev. Applied **7**, 014004 (2017).

[87] X. Fan, J. Wu, Y. Chen, M. J. Jerry, H. Zhang, and J. Q. Xiao, "Observation of the nonlocal spin-orbital effective field", Nature Communications **4** (2013).

[88] C. O. Avci, K. Garello, M. Gabureac, A. Ghosh, A. Fuhrer, S. F. Alvarado, and P. Gambardella, "Interplay of spin-orbit torque and thermoelectric effects in ferromagnet/normal-metal bilayers", Phys. Rev. B **90**, 224427 (2014).

[89] A. Manchon and S. Zhang, "Theory of spin torque due to spin-orbit coupling", Phys. Rev. B **79**, 094422 (2009).

[90] I. A. Ado, O. A. Tretiakov, and M. Titov, "Microscopic theory of spin-orbit torques in two dimensions", Phys. Rev. B **95**, 094401 (2017).

[91] P. B. Ndiaye, C. A. Akosa, M. H. Fischer, A. Vaezi, E.-A. Kim, and A. Manchon, "Dirac spin-orbit torques and charge pumping at the surface of topological insulators", Phys. Rev. B **96**, 014408 (2017).

[92] A. Manchon, J. Železný, I. M. Miron, T. Jungwirth, J. Sinova, A. Thiaville, K. Garello, and P. Gambardella, "Current-induced spin-orbit torques in ferromagnetic and antiferromagnetic systems", Rev. Mod. Phys. **91**, 035004 (2019).

[93] K. Dolui, M. D. Petrović, K. Zollner, P. Plecháč, J. Fabian, and B. K. Nikolić, "Proximity spin–orbit torque on a two-dimensional magnet within van der Waals heterostructure: current-driven antiferromagnet-to-ferromagnet reversible nonequilibrium phase transition in bilayer CrI_3", Nano Letters **20**, 2288–2295 (2020).

[94] K. Zollner, M. D. Petrović, K. Dolui, P. Plecháč, B. K. Nikolić, and J. Fabian, "Scattering-induced and highly tunable by gate damping-like spin-orbit torque in graphene doubly proximitized by two-dimensional magnet $Cr_2Ge_2Te_6$ and monolayer WS_2", Phys. Rev. Research **2**, 043057 (2020).

[95] J Sinova and T Jungwirth, "Surprises from the spin Hall effect", Physics Today **70**, 38 (2017).

[96] N. Tombros, C. Jozsa, M. Popinciuc, H. T. Jonkman, and B. J. van Wees, "Electronic spin transport and spin precession in single graphene layers at room temperature", Nature **448**, 571–574 (2007).

[97] M. V. Kamalakar, C. Groenveld, A. Dankert, and S. P. Dash, "Long distance spin communication in chemical vapour deposited graphene", Nature Communications **6**, 6766 (2015).

[98] J. Sichau, M. Prada, T. Anlauf, T. J. Lyon, B. Bosnjak, L. Tiemann, and R. H. Blick, "Resonance microwave measurements of an intrinsic spin-orbit coupling gap in graphene: a possible indication of a topological state", Phys. Rev. Lett. **122**, 046403 (2019).

[99] A. Avsar, H. Ochoa, F. Guinea, B. Özyilmaz, B. J. van Wees, and I. J. Vera-Marun, "Colloquium: spintronics in graphene and other two-dimensional materials", Rev. Mod. Phys. **92**, 021003 (2020).

[100] J. Serrano, M. Cardona, and T. Ruf, "Spin–orbit splitting in diamond: excitons and acceptor related states", Solid State Communications **113**, 411–414 (2000).

[101] A. H. Castro Neto and F. Guinea, "Impurity-induced spin-orbit coupling in graphene", Phys. Rev. Lett. **103**, 026804 (2009).

[102] J. Ding, Z. Qiao, W. Feng, Y. Yao, and Q. Niu, "Engineering quantum anomalous/valley Hall states in graphene via metal-atom adsorption: an ab-initio study", Phys. Rev. B **84**, 195444 (2011).

[103] H. Zhang, C. Lazo, S. Blügel, S. Heinze, and Y. Mokrousov, "Electrically tunable quantum anomalous hall effect in graphene decorated by $5d$ transition-metal adatoms", Phys. Rev. Lett. **108**, 056802 (2012).

[104] U. Chandni, E. A. Henriksen, and J. P. Eisenstein, "Transport in indium-decorated graphene", Phys. Rev. B **91**, 245402 (2015).

[105] Z. Jia, B. Yan, J. Niu, Q. Han, R. Zhu, D. Yu, and X. Wu, "Transport study of graphene adsorbed with indium adatoms", Phys. Rev. B **91**, 085411 (2015).

[106] Y. Wang, S. Xiao, X. Cai, W. Bao, J. Reutt-Robey, and M. S. Fuhrer, "Electronic transport properties of Ir-decorated graphene", Scientific Reports **5** (2015).

[107] K. T. Chan, J. B. Neaton, and M. L. Cohen, "First-principles study of metal adatom adsorption on graphene", Phys. Rev. B **77**, 235430 (2008).

[108] F. J. d. Santos, D. A. Bahamon, R. B. Muniz, K. McKenna, E. V. Castro, J. Lischner, and A. Ferreira, "Impact of complex adatom-induced interactions on quantum spin hall phases", Phys. Rev. B **98**, 081407 (2018).

[109] A. K. Geim and I. V. Grigorieva, "Van der Waals heterostructures", Nature **499** (2013).

[110] S. Z. i. Butler, "Progress, challenges, and opportunities in two-dimensional materials beyond graphene", ACS Nano **7**, 2898–2926 (2013).

[111] L. Britnell, R. V. Gorbachev, R. Jalil, B. D. Belle, F. Schedin, A. Mishchenko, T. Georgiou, M. I. Katsnelson, L. Eaves, S. V. Morozov, N. M. R. Peres, J. Leist, A. K. Geim, K. S. Novoselov, and L. A. Ponomarenko, "Field-effect tunneling transistor based on vertical graphene heterostructures", Science **335**, 947–950 (2012).

[112]T. Georgiou, R. Jalil, B. D. Belle, L. Britnell, R. V. Gorbachev, S. V. Morozov, Y.-J. Kim, A. Gholinia, S. J. Haigh, O. Makarovsky, L. Eaves, L. A. Ponomarenko, A. K. Geim, K. S. Novoselov, and A. Mishchenko, "Vertical field-effect transistor based on graphene–WS_2 heterostructures for flexible and transparent electronics", Nature Nanotechnology **8**, 100–103 (2013).

[113]S. Bertolazzi, D. Krasnozhon, and A. Kis, "Nonvolatile memory cells based on MoS_2/graphene heterostructures", ACS Nano **7**, 3246–3252 (2013).

[114]B. Hunt, J. D. Sanchez-Yamagishi, A. F. Young, M. Yankowitz, B. J. LeRoy, K. Watanabe, T. Taniguchi, P. Moon, M. Koshino, P. Jarillo-Herrero, and R. C. Ashoori, "Massive dirac fermions and hofstadter butterfly in a van der waals heterostructure", Science **340**, 1427–1430 (2013).

[115]K. F. Mak, C. Lee, J. Hone, J. Shan, and T. F. Heinz, "Atomically thin MoS_2: a new direct-gap semiconductor", Phys. Rev. Lett. **105**, 136805 (2010).

[116]Z. Y. Zhu, Y. C. Cheng, and U. Schwingenschlögl, "Giant spin-orbit-induced spin splitting in two-dimensional transition-metal dichalcogenide semiconductors", Phys. Rev. B **84**, 153402 (2011).

[117]D. Xiao, G.-B. Liu, W. Feng, X. Xu, and W. Yao, "Coupled spin and valley physics in monolayers of MoS_2 and other group-VI dichalcogenides", Phys. Rev. Lett. **108**, 196802 (2012).

[118]W. Yao, D. Xiao, and Q. Niu, "Valley-dependent optoelectronics from inversion symmetry breaking", Phys. Rev. B **77**, 235406 (2008).

[119]T. Cao, G. Wang, W. Han, H. Ye, C. Zhu, J. Shi, Q. Niu, P. Tan, E. Wang, B. Liu, and J. Feng, "Valley-selective circular dichroism of monolayer molybdenum disulphide", Nature Communications **3** (2012).

[120]M. Gmitra and J. Fabian, "Graphene on transition-metal dichalcogenides: a platform for proximity spin-orbit physics and optospintronics", Phys. Rev. B **92**, 155403 (2015).

[121]M. Gmitra, D. Kochan, P. Högl, and J. Fabian, "Trivial and inverted Dirac bands and the emergence of quantum spin Hall states in graphene on transition-metal dichalcogenides", Phys. Rev. B **93** (2016).

[122]A. Avsar, J. Y. Tan, T. Taychatanapat, J. Balakrishnan, G. Koon, Y. Yeo, A. Lahiri J.and Carvalho, A. S. Rodin, E. O'Farrell, G. Eda, A. H. Castro Neto, and B. Özyilmaz, "Spin-orbit proximity effect in graphene", Nat. Comm. **5** (2014).

[123]Y. K. Luo, J. Xu, T. Zhu, G. Wu, E. J. McCormick, W. Zhan, M. R. Neupane, and R. K. Kawakami, "Opto-valleytronic spin injection in monolayer MoS_2/few-layer graphene hybrid spin valves", Nano Letters **17**, 3877–3883 (2017).

[124]G. P. Thomson and A. Reid, "Diffraction of cathode rays by a thin film", Nature **119**, 890–890 (1927).

[125]C. Davisson and L. H. Germer, "The scattering of electrons by a single crystal of nickel", Nature **119**, 558–560 (1927).

[126]Y. Kuga and A. Ishimaru, "Retroreflectance from a dense distribution of spherical particles", J. Opt. Soc. Am. A **1**, 831–835 (1984).

[127]M. P. V. Albada and A. Lagendijk, "Observation of weak localization of light in a random medium", Phys. Rev. Lett. **55**, 2692–2695 (1985).

[128]P.-E. Wolf and G. Maret, "Weak localization and coherent backscattering of photons in disordered media", Phys. Rev. Lett. **55**, 2696–2699 (1985).

[129]P. Drude, "Zur elektronentheorie der metalle", Annalen der Physik **306**, 566–613 (1900).

[130]E. Abrahams, P. W. Anderson, D. C. Licciardello, and T. V. Ramakrishnan, "Scaling theory of localization: absence of quantum diffusion in two dimensions", Phys. Rev. Lett. **42**, 673–676 (1979).

[131]J. S. Langer and T. Neal, "Breakdown of the concentration expansion for the impurity resistivity of metals", Phys. Rev. Lett. **16**, 984–986 (1966).

[132]L. P. Gor'kov, A. I. Larkin, and D. E. Khmel'Nitskii, "Particle conductivity in a two-dimensional random potential", JETP Lett. **30**, 228–232 (1979).

[133]B. L. Altshuler, D. Khmel'nitzkii, A. I. Larkin, and P. A. Lee, "Magnetoresistance and Hall effect in a disordered two-dimensional electron gas", Phys. Rev. B **22**, 5142–5153 (1980).

[134]S. Hikami, A. I. Larkin, and Y. Nagaoka, "Spin-orbit interaction and magnetoresistance in the two dimensional random system", Prog. of Theor. Phys. **63**, 707–710 (1980).

[135]G. Bergmann, "Physical interpretation of weak localization: a time-of-flight experiment with conduction electrons", Phys. Rev. B **28**, 2914–2920 (1983).

[136]C. W. J. Beenakker, "Random-matrix theory of quantum transport", Rev. Mod. Phys. **69**, 731–808 (1997).

[137]H. A. Weidenmüller and G. E. Mitchell, "Random matrices and chaos in nuclear physics: nuclear structure", Rev. Mod. Phys. **81**, 539–589 (2009).

[138]G. E. Mitchell, A. Richter, and H. A. Weidenmüller, "Random matrices and chaos in nuclear physics: nuclear reactions", Rev. Mod. Phys. **82**, 2845–2901 (2010).

[139]P. W. Brouwer, J. N. H. J. Cremers, and B. I. Halperin, "Weak localization and conductance fluctuations of a chaotic quantum dot with tunable spin-orbit coupling", Phys. Rev. B **65**, 081302 (2002).

[140]E. McCann, "Staying or going? chirality decides!", Physics 2 **98** (2009).

[141]S. Zihlmann, A. W. Cummings, J. H. Garcia, M. Kedves, K. Watanabe, T. Taniguchi, C. Schönenberger, and P. Makk, "Large spin relaxation anisotropy and valley-Zeeman spin-orbit coupling in WSe_2/graphene/h-BN heterostructures", Phys. Rev. B **97**, 075434 (2018).

[142]H. Suzuura and T. Ando, "Crossover from symplectic to orthogonal class in a two-dimensional honeycomb lattice", Phys. Rev. Lett. **89** (2002).

[143]E. McCann, K. Kechedzhi, V. I. Fal'ko, H. Suzuura, T. Ando, and B. L. Altshuler, "Weak-localization magnetoresistance and valley symmetry in graphene", Phys. Rev. Lett. **97**, 146805 (2006).

[144]S. V. Morozov, K. S. Novoselov, M. I. Katsnelson, F. Schedin, L. A. Ponomarenko, D. Jiang, and A. K. Geim, "Strong suppression of weak localization in graphene", Phys. Rev. Lett. **97**, 016801 (2006).

[145]F. V. Tikhonenko, D. W. Horsell, R. V. Gorbachev, and A. K. Savchenko, "Weak localization in graphene flakes", Phys. Rev. Lett. **100**, 056802 (2008).

[146]S. Pezzini, C. Cobaleda, E. Diez, and V. Bellani, "Quantum interference corrections to magnetoconductivity in graphene", Phys. Rev. B **85**, 165451 (2012).

[147]Z. Wang, D. Ki, H. Chen, H. Berger, A. H. MacDonald, and A. F. Morpurgo, "Strong interface-induced spin–orbit interaction in graphene on WS_2", Nature Communications **6** (2015).

[148]Z. Wang, D.-K. Ki, J. Y. Khoo, D. Mauro, H. Berger, L. S. Levitov, and A. F. Morpurgo, "Origin and magnitude of 'designer' spin-orbit interaction in graphene on semiconducting transition metal dichalcogenides", Phys. Rev. X **6**, 041020 (2016).

[149] T. Völkl, T. Rockinger, M. Drienovsky, K. Watanabe, T. Taniguchi, D. Weiss, and J. Eroms, "Magnetotransport in heterostructures of transition metal dichalcogenides and graphene", Phys. Rev. B **96**, 125405 (2017).

[150] T. Wakamura, F. Reale, P. Palczynski, S. Guéron, C. Mattevi, and H. Bouchiat, "Strong anisotropic spin-orbit interaction induced in graphene by monolayer WS_2", Phys. Rev. Lett. **120**, 106802 (2018).

[151] E. McCann and V. I. Fal'ko, ".$z \to -z$ Symmetry of spin-orbit coupling and weak localization in graphene", Phys. Rev. Lett. **108**, 166606 (2012).

[152] H. Ochoa, F. Finocchiaro, F. Guinea, and V. I. Fal'ko, "Spin-valley relaxation and quantum transport regimes in two-dimensional transition-metal dichalcogenides", Phys. Rev. B **90**, 235429 (2014).

[153] S. Ilić, J. S. Meyer, and M. Houzet, "Weak localization in transition metal dichalcogenide monolayers and their heterostructures with graphene", Phys. Rev. B **99**, 205407 (2019).

[154] K.-I. Imura, Y. Kuramoto, and K. Nomura, "Weak localization properties of the doped Z_2 topological insulator", Phys. Rev. B **80**, 085119 (2009).

[155] H.-Z. Lu, J. Shi, and S.-Q. Shen, "Competition between weak localization and antilocalization in topological surface states", Phys. Rev. Lett. **107**, 076801 (2011).

[156] G. Baym, "Self-consistent approximations in many-body systems", Phys. Rev. **127**, 1391–1401 (1962).

[157] *Quantum transport theory (1st ed.)* (CRC Press, Boca Raton, 2004).

[158] R. Kubo, "A general expression for the conductivity tensor", Canadian Journal of Physics **34**, 1274–1277 (1956).

[159] R. Kubo, "Statistical-mechanical theory of irreversible processes", Journal of the Physical Society of Japan **12**, 570–586 (1957).

[160] G Mahan, *Many particle physics (3rd ed.)* (Springer Science, New York, 2000).

[161] A. Bastin, C. Lewiner, O. Betbeder-Matibet, and P. Nozières", "Quantum oscillations of the hall effect of a fermion gas with random impurity scattering", Journal of Physics and Chemistry of Solids **32**, 1811 –1824 (1971).

[162] P. Středa, "Theory of quantised hall conductivity in two dimensions", Journal of Physics C: Solid State Physics **15**, L717–L721 (1982).

[163] A. Crépieux and P. Bruno, "Theory of the anomalous Hall effect from the Kubo formula and the Dirac equation", Phys. Rev. B **64**, 014416 (2001).

[164]M. Milletarì and A. Ferreira, "Quantum diagrammatic theory of the extrinsic spin hall effect in graphene", Phys. Rev. B **94**, 134202 (2016).

[165]A. A. Burkov, A. S. Núñez, and A. H. MacDonald, "Theory of spin-charge-coupled transport in a two-dimensional electron gas with rashba spin-orbit interactions", Phys. Rev. B **70**, 155308 (2004).

[166]M. Offidani, R. Raimondi, and A. Ferreira, "Microscopic linear response theory of spin relaxation and relativistic transport phenomena in graphene", Condens. Matter **3**, 18 (2018).

[167]A. Ferreira and et al., "Unified description of the dc conductivity of monolayer and bilayer graphene at finite densities based on resonant scatterers", Phys. Rev. B **83**, 165402 (2011).

[168]A. Ferreira, T. G. Rappoport, M. A. Cazalilla, and A. H. C. Castro, "Extrinsic spin hall effect induced by resonant skew scattering in graphene", Phys. Rev. Lett. **112**, 066601 (2014).

[169]C. Huang, Y. D. Chong, and M. A. Cazalilla, "Direct coupling between charge current and spin polarization by extrinsic mechanisms in graphene", Phys. Rev. B **94**, 085414 (2016).

[170]S. S. Kubakaddi, "Interaction of massless dirac electrons with acoustic phonons in graphene at low temperatures", Phys. Rev. B **79**, 075417 (2009).

[171]R. Bistritzer and A. H. MacDonald, "Electronic cooling in graphene", Phys. Rev. Lett. **102**, 206410 (2009).

[172]W.-K. Tse and S. Das Sarma, "Energy relaxation of hot dirac fermions in graphene", Phys. Rev. B **79**, 235406 (2009).

[173]A. Laitinen, M. Oksanen, A. Fay, D. Cox, M. Tomi, P. Virtanen, and P. J. Hakonen, "Electron–phonon coupling in suspended graphene: supercollisions by ripples", Nano Letters **14**, 3009–3013 (2014).

[174]J. Kondo, "Resistance minimum in dilute magnetic alloys", Progress of Theoretical Physics **32**, 37–49 (1964).

[175]A. Qaiumzadeh, N. Arabchi, and R. Asgari, "Quasiparticle properties of graphene in the presence of disorder", Solid State Communications **147**, 172 –177 (2008).

[176]S. Lara-Avila, A. Tzalenchuk, S. Kubatkin, R. Yakimova, T. J. B. M. Janssen, K. Cedergren, T. Bergsten, and V. Fal'ko, "Disordered fermi liquid in epitaxial graphene from quantum transport measurements", Phys. Rev. Lett. **107**, 166602 (2011).

[177] P. W. Anderson, "Absence of diffusion in certain random lattices", Phys. Rev. **109**, 1492–1505 (1958).

[178] P. A. Lee and T. V. Ramakrishnan, "Disordered electronic systems", Rev. Mod. Phys. **57**, 287–337 (1985).

[179] J. Billy, V. Josse, Z. Zuo, A. Bernard, B. Hambrecht, P. Lugan, D. Clément, L. Sanchez-Palencia, P. Bouyer, and A. Aspect, "Direct observation of anderson localization of matter waves in a controlled disorder", Nature **453**, 891–894 (2008).

[180] J. M. Ziman, *Principles of the theory of solids*, 2nd ed. (Cambridge University Press, 1972).

[181] L. E. Ballentine, *Quantum mechanics* (World Scientific, 2014).

[182] P. Wenk and S. Kettemann, "Dimensional dependence of weak localization corrections and spin relaxation in quantum wires with rashba spin-orbit coupling", Phys. Rev. B **81**, 125309 (2010).

[183] M. Kammermeier, P. Wenk, J. Schliemann, S. Heedt, and T. Schäpers, "Weak (anti)localization in tubular semiconductor nanowires with spin-orbit coupling", Phys. Rev. B **93**, 205306 (2016).

[184] P. R. Wallace, "The band theory of graphite", Phys. Rev. **71**, 622–634 (1947).

[185] C. L. Kane and E. J. Mele, "Quantum spin Hall effect in graphene", Phys. Rev. Lett. **95** (2005).

[186] M. Gmitra and J. Fabian, "Graphene on transition-metal dichalcogenides: a platform for proximity spin-orbit physics and optospintronics", Phys. Rev. B **92**, 155403 (2015).

[187] D. Kochan, S. Irmer, and J. Fabian, "Model spin-orbit coupling hamiltonians for graphene systems", Phys. Rev. B **95**, 165415 (2017).

[188] M. Offidani, M. Milletarì, R. Raimondi, and A. Ferreira, "Optimal charge-to-spin conversion in graphene on transition-metal dichalcogenides", Phys. Rev. Lett. **119**, 196801 (2017).

[189] S. Cho, Y.-F. Chen, and M. S. Fuhrer, "Gate-tunable graphene spin valve", Applied Physics Letters **91**, 123105 (2007).

[190] W. Jin, P.-C. Yeh, N. Zaki, D. Zhang, J. T. Sadowski, A. Al-Mahboob, A. M. van der Zande, D. A. Chenet, J. I. Dadap, I. P. Herman, P. Sutter, J. Hone, and R. M. Osgood, "Direct measurement of the thickness-dependent electronic band structure of MoS_2 using angle-resolved photoemission spectroscopy", Phys. Rev. Lett. **111**, 106801 (2013).

[191] M. Milletarì, M. Offidani, A. Ferreira, and R. Raimondi, "Covariant conservation laws and the spin hall effect in dirac-rashba systems", Phys. Rev. Lett. **119**, 246801 (2017).

[192] T. Ando, T. Nakanishi, and R. Saito, "Berry's phase and absence of back scattering in carbon nanotubes", Journal of the Physical Society of Japan **67**, 2857–2862 (1998).

[193] Y. Araki, G. Khalsa, and A. H. MacDonald, "Weak localization, spin relaxation, and spin diffusion: crossover between weak and strong rashba coupling limits", Phys. Rev. B **90** (2014).

[194] A. Pachoud, A. Ferreira, B. Özyilmaz, and A. H. C. Neto, "Scattering theory of spin-orbit active adatoms on graphene", Phys. Rev. B **90**, 035444 (2014).

[195] D.-K. Ki, D. Jeong, J.-H. Choi, H.-J. Lee, and K.-S. Park, "Inelastic scattering in a monolayer graphene sheet: a weak-localization study", Phys. Rev. B **78**, 125409 (2008).

[196] M. Offidani and A. Ferreira, "Microscopic theory of spin relaxation anisotropy in graphene with proximity-induced spin-orbit coupling", Phys. Rev. B **98**, 245408 (2018).

[197] B. Yan, Q. Han, Z. Jia, J. Niu, T. Cai, D. Yu, and X. Wu, "Electrical control of intervalley scattering in graphene via the charge state of defects", Phys. Rev. B **93**, 041407 (2016).

[198] B. Yang, M. Lohmann, D. Barroso, I. Liao, Z. Lin, Y. Liu, L. Bartels, K. Watanabe, T. Taniguchi, and J. Shi, "Strong electron-hole symmetric rashba spin-orbit coupling in graphene/monolayer transition metal dichalcogenide heterostructures", Phys. Rev. B **96**, 041409 (2017).

[199] T. Wakamura, F. Reale, P. Palczynski, S. Guéron, C. Mattevi, and H. Bouchiat, "Strong anisotropic spin-orbit interaction induced in graphene by monolayer WS_2", Phys. Rev. Lett. **120**, 106802 (2018).

[200] K. D. Belashchenko, A. A. Kovalev, and M. van Schilfgaarde, "Interfacial contributions to spin-orbit torque and magnetoresistance in ferromagnet/heavy-metal bilayers", Phys. Rev. B **101**, 020407 (2020).

[201] A. Veneri, F. Sousa, M. Petrović, N. Branislav, and A. Ferreira, in preparation.

[202] D. V. Fedorov, M. Gradhand, S. Ostanin, I. V. Maznichenko, A. Ernst, J. Fabian, and I. Mertig, "Impact of electron-impurity scattering on the spin relaxation time in graphene: a first-principles study", Phys. Rev. Lett. **110**, 156602 (2013).

[203] A. Dyrdał and J. Barnaś, "Current-induced spin polarization and spin-orbit torque in graphene", Phys. Rev. B **92**, 165404 (2015).

[204] G. Géranton, F. Freimuth, S. Blügel, and Y. Mokrousov, "Spin-orbit torques in $L1_0$-FePt/Pt thin films driven by electrical and thermal currents", Phys. Rev. B **91**, 014417 (2015).

[205] S. Wimmer, K. Chadova, M. Seemann, D. Ködderitzsch, and H. Ebert, "Fully relativistic description of spin-orbit torques by means of linear response theory", Phys. Rev. B **94**, 054415 (2016).

[206] J. Qi, X. Li, Q. Niu, and J. Feng, "Giant and tunable valley degeneracy splitting in $MoTe_2$", Phys. Rev. B **92**, 121403 (2015).

[207] Q.-F. Yao and et al, "Manipulation of the large Rashba spin splitting in polar two-dimensional transition-metal dichalcogenides", Phys. Rev. B **95**, 165401 (2017).

[208] C. Zhao and et al, "Enhanced valley splitting in monolayer WSe_2 due to magnetic exchange field", Nature Nanotechnology **12**, 757 (2017).

[209] T. Norden and et al., "Giant valley splitting in monolayer ws_2 by magnetic proximity effect", Nat.Commun. **10**, 4163 (2019).

[210] V. P. Amin and M. D. Stiles, "Spin transport at interfaces with spin-orbit coupling: phenomenology", Phys. Rev. B **94**, 104420 (2016).

[211] F. Sousa, G. Tatara, and A. Ferreira, "Skew-scattering-induced giant anti-damping spin-orbit torques: collinear and out-of-plane edelstein effects at two-dimensional material/ferromagnet interfaces", Phys. Rev. Research **2**, 043401 (2020).

[212]H. Kurebayashi, J. Sinova, D. Fang, A. C. Irvine, T. D. Skinner, J. Wunderlich, V. Novák, R. P. Campion, B. L. Gallagher, E. K. Vehstedt, L. P. Zârbo, K. Výborný, A. J. Ferguson, and T. Jungwirth, "An antidamping spin–orbit torque originating from the Berry curvature", Nature Nanotechnology 9, 211–217 (2014).

[213]F. Freimuth, S. Blügel, and Y. Mokrousov, "Spin-orbit torques in Co/Pt(111) and Mn/W(001) magnetic bilayers from first principles", Phys. Rev. B 90, 174423 (2014).

[214]T. Gao, A. Qaiumzadeh, H. An, A. Musha, Y. Kageyama, J. Shi, and K. Ando, "Intrinsic spin-orbit torque arising from the Berry curvature in a metallic-magnet/cu-oxide interface", Phys. Rev. Lett. 121, 017202 (2018).

[215]A. Cassam-Chenai and B. Shapiro, "Two dimensional weak localization beyond the diffusion approximation", Journal de Physique I 4 (1994).